

## ABSTRACT

Title of Document: STRESS RESPONSE OF TALL AND HEAVY  
ELECTRONIC COMPONENTS SUBJECTED  
TO MULTI-AXIAL VIBRATION

Raman Sridharan, Master of Science, 2017

Directed By: Dr Abhijit Dasgupta,  
Department of Mechanical Engineering

Electronic assemblies often experience multiaxial vibration environments in use and tall, heavy components are more vulnerable when exposed to multiaxial vibration than are shorter, lighter assemblies. The added vulnerability comes from higher stresses that are a result of nonlinear dynamic amplification which large components are susceptible to under simultaneous multiaxial excitation, termed multi degree of freedom (MDoF) excitation. However, it is still common practice to conduct vibration durability testing on electronic assemblies one axis at a time – in what is termed sequential single degree of freedom (SSDoF) testing. SSDoF testing has been shown to produce lower fatigue damage accumulation rates than simultaneous MDoF testing, in the leads of tall and heavy electronic components. This leads to overestimating the expected lifespan of the assembly.

This paper investigates the geometric nonlinearities and the resulting cross-axis interactions that tall and heavy electronic components experience when subjected to vibration excitation along two orthogonal axes – one direction is in the plane of the PWB and the other is along the normal to the PWB. The direction normal to the PWB aligns with the axial direction of the leads, while the in-plane direction aligns with the primary bending direction of the leads. Harmonic excitation was simultaneously applied to both axes to study the vibration response as a

function of frequency ratio and phase “difference” along the two axes. The experimental observations were verified with a nonlinear dynamic Finite Element study. The effect of geometric nonlinearity on cyclic stresses seen in the vibrating component are analyzed.

Stress Response of Tall and Heavy Electronic Components  
Subjected to Multi-axial Vibration

Raman Sridharan

Thesis submitted to the Faculty of the Graduate School of the  
University of Maryland, College Park in partial fulfillment  
of the requirements for the degree of  
Masters of Science  
2017

Advisory Committee:

Professor Abhijit Dasgupta, Chair

Professor Amr Baz

Professor Miao Yu

## **Acknowledgements**

This paper would not have come to be without the help of many individuals.

My advisor, Professor Abhijit Dasgupta, is responsible for maintaining the continuing body of work that this thesis is a part of. He has handled this project through three previous graduate students, and has set the direction and scope of the work I completed as a part of this paper. His long and late hours spent editing and critiquing papers, results, and presentations provided the foundation of all the work presented in this thesis.

This thesis is a part of a continuing research project, at the CALCE lab, and all the work in this paper is based on the work of students before me. Dr. Ed Habtour and Matthew Ernst laid the groundwork for everything I have presented in this thesis. Furthermore, Dr. Habtour has presented experimental results similar to those presented in this thesis, and he assisted in understanding the analytical side of the subject area.

The entire A-Team (Dr. Dasgupta's lab group) helped me get through the long nights in the lab, and provided many laughs along the way.

Tom Reilly of Data Physics Corporation was instrumental in steering me towards Maryland, and along with Weijie Zhao taught me all I know about the multi-shaker control system SignalStar Matrix. Without their training over the years, the experimental section of this thesis would not have been possible. Joel Hoksbergen of Team Corporation was also instrumental in assisting with the Team Tensor shaker table; and his service visits to the lab are much appreciated.

## Contents

ACKNOWLEDGEMENTS .....	II
LIST OF FIGURES .....	V
LIST OF TABLES .....	VII
LIST OF EQUATIONS .....	VII
1 INTRODUCTION .....	1
1.1 Background and Literature Review.....	1
1.2 Purpose.....	7
2 EXPERIMENTAL STUDY .....	8
2.1 Introduction .....	8
2.2 Test Setup Description .....	10
2.2.1 Test Equipment Limitations.....	11
2.2.2 Data Processing Methodologies.....	18
2.2.3 Test Specimen Selection .....	19
2.2.4 Test Specimen Calibration.....	21
2.3 Test Procedures and Data Acquisition Setup.....	22
2.4 Test matrix.....	25
2.4.1 Test Results.....	25
2.4.2 Data.....	25
3 FINITE ELEMENT STUDY ON EFFECT OF PHASE AND FREQUENCY RATIO.....	32
3.1 Introduction .....	32
3.2 Finite element model description .....	32
3.3 Simulation software.....	37
3.4 Simulation test matrix .....	37
3.5 Finite element study results.....	42
3.5.1 Simulation Results .....	42
3.5.2 Interpretation of Simulation Results .....	46
3.6 Comparison of finite element results with experimental results .....	55
3.6.1 Experimental validation with finite element.....	56
4 SUMMARY, CONCLUSIONS, AND FUTURE WORK .....	63
4.1 Summary and conclusions.....	63

4.2	Limitations and future work.....	63
4.2.1	Experimental limitations.....	63
4.2.2	Finite Element Limitations .....	65
4.2.3	Future Work .....	65
5	APPENDIX .....	76
5.1	Aluminum 6061-T6 Properties.....	76
5.2	Rayleigh Damping Relationship .....	76
5.3	Complete Simulation Matrix for Finite Element Study .....	76
5.4	Results for each Phase Sweep (Frequency Ratio Constant) in Finite Element Study....	79
5.5	Phase Extraction from Time Data (MATLAB Code) .....	83
5.6	Highpass Filter applied to data before integration .....	85
5.7	Periodicity of two sine waves at different frequencies, and how phase relationship between two waves can be described as a single phase angle .....	86
5.8	PWB Properties .....	92
5.9	Beam With Tip Mass Natural Frequency Derivation.....	93
6	REFERENCES .....	99

## List of Figures

Figure 1: Finite element model of beam with tip mass.....	8
Figure 2: Simulation results presented by Ernst, exciting a component sinusoidally in two axes; changing the ratios of frequencies being excited.....	9
Figure 3: Simulation results presented by Ernst, frequency ratio held at 2 while changing phase between excitaiton signals .....	9
Figure 4: Exploded view of TEAM Tensor shaker arrangement.....	11
Figure 5: TEAM Tensor.....	11
Figure 6: Top down view of shaker table and test specimen/fisxure, with four DYTRAN control accelerometers outlined .....	13
Figure 7: Test Specimen mounted in fixture. The top image is unlabeled, while the bottom image is labeled for clarity.....	16
Figure 8: In the foreground, the test specimen with two accelerometers mounted on it (only one was used to measure). On the shaker table, a third measurement accelerometer (labeled in Red) was used to identify the phase offset between the axes' excitations. ....	18
Figure 9: Test specimen set up on TEAM Tensor .....	21
Figure 10: Time history of the $\hat{x}$ and $\hat{y}$ accelerations from the accelerometer at the center of the shaker table .....	26
Figure 11: Zero phase segment of Y acceleration, and its frequency components.....	27
Figure 12: 2048-sample of measured X axis excitation, corresponding to the Y axis excitation in Figure 11 .....	28
Figure 13: X Response of beam during Test 1. $T < 30$ represents the beam's tip response under single axis excitation, and $t > 45$ represents the response due to combine multi-axis excitation. The X axis excitation was held constant once started at $t = 5$ , the Y axis excitaiton was added after $t = 30$ , after the X-axis-only response had reached steady state .....	30
Figure 14: Experimental results, processed, Peak steady state stress vs. excitation phase at frequency ratio 2 .....	31
Figure 15: FEM Model of beam with tip mass .....	33
Figure 16: FEM model of large electronic component (left, A) and simplified component model (right, B).....	34
Figure 17: First bending mode of component model.....	34
Figure 18: First bending mode of electronic components excited while mounted on a circuit card .....	35
Figure 19: First bending mode of circuit card with large electronic components mounted on it	35
Figure 20: Large electronic component model undergoing bi-axial excitation, with nonlinear moment drawn .....	36
Figure 21: Excitation signals used for test 7 (Frequency ratio 1, phase 180) and 53 (frequency ratio 2, phase 0).....	41
Figure 22: Stress response at base of component model for simulation condition 1.....	42
Figure 23: Excitation and response of component for simulation test 1.....	42

Figure 24: Peak steady state stress response observed in component base, for phase 0-360° and frequency ratio 1. Plot Y axis range set to match other result plots, for comparison purposes...	43
Figure 25: Steady state stress amplification (MDoF/SDoF) observed in all simulations (frequency ratios 1-3, excitation phases 0-360).....	45
Figure 26: One cycle of component model's first bending mode (excited by x excitation) with nonlinear moment shown.....	46
Figure 27: Component model with nonlinear moment shown.....	48
Figure 28: Steady State Tip Response (x) for simulation 31, frequency ratio 1.25, phase 0° .....	51
Figure 29: Steady State Tip Response (x) for simulation 98, frequency ratio 2.75, phase 90° ....	52
Figure 30: Steady State Tip Response (x) for simulation 53, frequency ratio 2, phase 0° .....	52
Figure 31: FEA simulation results (left) and experimental results (right).....	55
Figure 32: Finite Element model, a beam with a tip mass. Excitations applied at base of beam.	56
Figure 33: FEM Verification amplification factors vs. Experimental Amplification Factors.....	61
Figure 34: The PWB model, the green PWB board with two large electronic components mounted on it. ....	67
Figure 35: Excitation signals for Simulation 1 .....	69
Figure 36: Excitation Boundary Condition for Simulation 7, 90deg phase.....	70
Figure 37: Stress Response of left component, Simulation 1 .....	71
Figure 38: Peak Stress in single component and PWA Simulations .....	72
Figure 39: Peak Stress in single component and PWA Simulations .....	73
Figure 40: Single Component and Component on PWB .....	74
Figure 41: Sine waves with a frequency ratio of 2 (f1=1,f2=2) .....	87
Figure 42: Frequency Ratio 1.25, f1=1, f2=1.25 .....	88
Figure 43: Frequency Ratio 2.75, f1=1, f2=2.75 .....	89
Figure 44:Frequency Ratio e, f1=1, f2 = <b>e</b> $\cong$ <b>2.71</b> .....	90



## List of Tables

Table 1: Selected test specimen properties .....	20
Table 2: Experimental test matrix.....	25
Table 3: Phase angles measured from test data .....	29
Table 5: Excitation frequencies used in simulation .....	39
Table 6: Excitation phases simulated for each frequency ratio .....	41
Table 4: Test Matrix for FEM verification .....	60

## List of Equations

Equation 1: Nonlinear bending moment.....	48
Equation 2: X_base.....	48
Equation 3: X_tip_linear.....	48
Equation 4: Y_dd_base.....	49
Equation 5:Y_dd_tip estimate.....	49
Equation 6: Nonlinear moment estimate.....	49
Equation 7: Nonlinear moment estimate expanded .....	49
Equation 8: Period of two sine waves at frequency f1 and f2 .....	86
Equation 9: Period of sine waves shown in Figure 37.....	87
Equation 10: Period of sine waves shown in Figure 38.....	88
Equation 11: Period of sine waves shown in Figure 39.....	89
Equation 12: LCM equation for periodicity of signals shown in Figure 40 .....	90
Equation 13: Elastic Potential Energy .....	93
Equation 3: Kinetic Energy.....	93
Equation 4: Lagrange.....	93
Equation 5:Variation.....	93
Equation 6:Euler Lagrange Principal.....	94
Equation 7:First term of Equation 5.....	94
Equation 8: Simplified First term of Equation 5.....	94
Equation 9: Second term of Equation 5 .....	94
Equation 10: Simplified Second term of Equation 5 .....	95
Equation 11: Partly Simplified Third Term of Equation 5 .....	95
Equation 12: Simplified Part 3 of Equation 5.....	96
Equation 13: Hamiltons variation Principal simplified .....	96
Equation 14: Equation of motion.....	96
Equation 15: Boundary Condition 1 .....	96
Equation 16: Boundary Condition 2 .....	96
Equation 17: Boundary Condition 3 .....	96
Equation 18: Boundary Condition 4 .....	96
Equation 19: Separated Equation of motion .....	97

Equation 20: Separated Equation of motion .....	97
Equation 21: Poles of spatial equation.....	97
Equation 22: Beta.....	97
Equation 23: Form of solution of spatial component.....	97
Equation 24: Boundary Condition result .....	97
Equation 25: Boundary Condition result .....	97
Equation 26: Boundary onditions plugged into solution .....	98
Equation 27: Final boundary condition plugged in.....	98
Equation 28: Matrix form of constants .....	98
Equation 29: Natural frequency function.....	98

# 1 Introduction

## 1.1 Background and Literature Review

The US Military has been a leader in environmental stress testing research and in developing relevant testing standards. MIL-STD-810G<sup>1</sup> is the current revision of the standard, and outlines environmental test specifications to simulate real world environments. Method 514.6 of MIL-STD-810G is intended to be used to develop products and materials that can withstand the multiaxial vibrations expected during the lifespan of that product/material. This method outlines test procedures and profiles for common classes of military vehicles, as well as procedures to combine vibration tests with other environmental effects such as temperature or humidity. Method 514.6, however, is explicitly limited to sequential uniaxial vibration excitation, *i.e.* a single degree of freedom (SDoF) at a time. It is common for three SDof tests – one in each orthogonal axis – to be sequentially performed in what is termed the sequential single degree of freedom (SSDoF) test methodology. This ensures the device under test experiences translational excitation along three principal directions, but not simultaneously. They also fail to test the response to rotational excitations.

Mil-STD-810G Method 527 addresses multiple-exciter and multiple-DoF testing (MDoF), however it is explicitly described as an initial version of a Multi-Exciter Testing (MET) standard. While Method 514.6 provides specific SDof testing profiles for various habitats, Method 527 advises the tester to measure the MDoF vibrations the product is expected to see during the life-cycle. These profiles are then to be replicated in a lab, either in the time or frequency domain. In general, generating running MDoF profiles is stated to require more research and development before methods are standardized. Method 527 also acknowledges that cost and availability of MDoF test equipment are a major limiting factor for a tester to run MDoF tests.

In the public domain, the only test procedure which explicitly outlines MDoF testing procedures is IEEE 344<sup>ii</sup>. This standard outlines MDoF testing standards for nuclear power equipment to withstand earthquakes.

The Society for Automotive Engineers produce the Handbook for Robustness Validation of Automotive Electrical/Electronic Modules. This handbook defines methods for producing reliable automotive electronics. Early revisions of this handbook outlined laboratory test conditions which replicated worst case life conditions. As automotive reliability improved, SAE has moved from a test-for-reliability ideology to a design-for-reliability ideology in its 2012 revision. As such, SAE is not pursuing MDoF vibration testing for electronic systems.

MIL-STD-810 asserts that there is an insufficient knowledgebase at the present time to create effective standards for MDoF vibration testing, however there have been many recent research publications which have begun to address the problem. In his paper, Habtour et al<sup>iii</sup> outlined the testing methodologies currently available for performing full 6-DoF vibration tests (3 translational and 3 rotational DoFs). There are two test setups which are commonly used to perform these type of tests: electrodynamic/hydraulic shaker tables with bearing systems that allow fully controllable 6-DoF motion, or repetitive shock shakers that allow only partial control over the excitation profiles.

Choi et al<sup>iv</sup> outlined the differences between electrodynamic/hydraulic test setups and Repetitive Shock setups. In the more expensive electrodynamic/hydraulic test setups, at least six shaker combinations are connected to the shaker table through a bearing system which allows each of the six degrees of freedom to be controlled fully and simultaneously. This allows the shaker system to replicate any type of vibration in its entirety, as long as the vibrations are within the physical limits of the shaker and controller. Repetitive Shock (RS) shakers, on the other

hand, generate quasi-random multiaxial vibration where the RMS acceleration level along the direction orthogonal to the shaker table can be controlled through a master gain knob, however each of the six degrees of freedom cannot be independently controlled. The dynamics of the shaker table, fixture, and device under test (DUT) determine the spectral content seen in each of the six degrees of freedom. An RS shaker uses pneumatic impactors as its vibration source. As a result, RS shakers produce vibration with a large crest factor, and much of the vibration energy exists at high frequencies.

The shaker system used in this study has been described by Smallwood and Gregory<sup>v</sup>. The TEAM TE6-900 is a small table that uses 12 electrodynamic shakers to produce fully controllable 6-DoF vibration. Smallwood and Gregory describe the system to be useful in multiaxial dynamic testing of small test articles. Their assessment along with experimental results presented by Habtour<sup>vi</sup> and Ernst<sup>vii</sup> provide confidence in the test system used in this study.

Papers have been published which pertain to the differences in fatigue life of materials in SDoF vs. MDoF excitation conditions. Whiteman and Burman<sup>viii</sup>, French et al<sup>ix</sup>, Gregory et al<sup>x</sup>, Habtour et al<sup>xi</sup>, and Ernst et al<sup>vii</sup> have all contributed to this field of research.

In their paper<sup>viii</sup>, Whiteman and Burman conducted experiments comparing fatigue life of a notched cantilever excited in SSDoF with that of the same notched cantilever beam excited in simultaneous 3-DoF. They controlled their broadband random profile such that each of the SSDoF tests were excited with the same amount of power as the 3-DoF condition. The SSDoF and 3-DoF tests also had the same frequency range. Whiteman and Burman demonstrated that the SSDoF excitation case resulted in much longer times to failure than did the 3-DoF excitation case. Additionally, they concluded the sequence of excitation in the SSDoF test affected the

time to failure. This is another problem encountered when SSDoF testing is used to replicate real world failures.

French et al<sup>ix</sup> also conducted experiments on a doubly-notched cantilever beam. In their experiment, sweeping sinusoidal excitation was applied to the beam simultaneously in 2-DoFs and times to failure were measured. The average of these times to failure was used as a baseline. Beam samples were then subjected to the same sinusoidal excitations sequentially, for a duration of the previously measured baseline time to failure in each axis. In their SSDoF experiments, every specimen survived the initial SDoF test, and most did not survive the second SDoF test. Ernst<sup>vii</sup> interpreted this as SSDoF being more damaging, as the time to failure per excitation DoF was smaller for the SSDoF case. However French<sup>ix</sup> notes that there is no physics based reasoning to measure time to failure normalized by number of excitation axes. French only concludes that MDoF excitation produces different durability results than SSDoF excitation.

In the study, French et al<sup>ix</sup> excited the doubly notched beam in the beam's two transverse directions. This is different than the analysis and results presented in this paper, and results cannot be directly compared.

Gregory et al<sup>x</sup> conducted experiments and finite element analysis (FEA) of a mass loaded cantilever beam. Gregory et al showed that the resulting strains, stresses, and tip accelerations are different in MDoF excitation than they are in SDoF excitation. His experiments were run on a 6-DoF shaker table similar to that used in this paper, and his test structure is modally similar to the structure tested in this paper. However for simplicity this paper only considers one mode of vibration, whereas Gregory et al considered multiple.

Ayen and Çelik<sup>xii</sup> conducted FEA studies comparing the stresses seen in a helicopter component. SDoF and MDoF random excitation conditions were considered, and analysis was

conducted in frequency domain. Stresses were computed by evaluating FEA matrices numerically. From this, damage accumulation rates were calculated using the computed stresses in conjunction with material fatigue models. Ayen and Çelik concluded that damage accumulation was underestimated by 30-70% when using the SDoF excitation condition. The analysis accentuates the importance of MDoF testing by estimating stresses caused by all degrees of freedom simultaneously. However it does not consider the effect of geometric nonlinearities. The analysis presented in the present study focuses on stress amplification caused by geometric nonlinearities.

Vijay Kumar et. al<sup>xiii</sup> derived analytical equations of motion for a cantilever beam excited with simultaneous axial and transverse excitations. Kumar also experimentally validated the derived equations of motion using a single axis shaker, with the beam (test specimen) mounted at an angle. Kumar noted considerable nonlinear interactions when the excitations applied consisted two sinusoids applied at the beam's resonant frequency and twice the beam's resonant frequency. Kumar noted both cases of increased beam deflection as well as decreased beam deflection; with the deflection varying based on the phase angle between the two excitation sinusoids. Kumar's work corresponds with his other papers written in conjunction with Rhoades et. al<sup>xiv</sup>, in which they initially validated the testing methodology ultimately used by Kumar.

Ernst<sup>vii</sup> presents results which also compare the efficacy of SSDoF testing versus MDoF testing. In Ernst's paper, a circuit card with large electronic components was provided translational broad band (random) SSDOF excitation in 2 orthogonal directions: in the plane of the circuit card and orthogonal to the plane of the circuit card. Samples were then excited simultaneously in both axes. The failure mode investigated was fatigue failure in the lead of the electronic components. This failure was primarily caused by stresses imparted by the

component's first bending mode being excited. Ernst noted the times to failure of the electronic components on the circuit card in (1) SSDoF random excitation, (2) coherent MDoF random excitation, and (3) incoherent MDoF random excitation. Coherence is described as the phase correlation between the two axes of excitation. The average time to failure was measured in each case. Ernst showed that the time to failure of the SSDoF case was far greater than either the coherent or incoherent MDoF excitation case.

Ernst noted<sup>vii</sup> that the test specimen used had a characteristic which perhaps exacerbated the damage accumulation rates in the MDoF case. The first bending mode of the circuit card was at twice the frequency of the first bending mode of the components. The frequency range of the random excitation was selected to include both response modes. Ernst demonstrated through FEA that this frequency ratio of two caused kinematically nonlinear interactions between the two orthogonal response modes, resulting in amplification of the stresses in the components' leads at certain phase relationships, under simultaneous biaxial excitation. These results agree with those presented by Rhodes and Kumar, in their experiments conducted by harmonically exciting a beam at two frequencies in two axes<sup>xiv</sup>. The critical excitation frequency ratio of two is also discussed in the literature by Nayfeh<sup>xv</sup>.

A study which focused on the MDoF induced geometric nonlinearities in electronic components was presented by Sridharan et al<sup>xvi</sup>. In this study, a simplified large electronic component was modeled in finite element as a cantilever beam with a mass at the tip. It was sinusoidally excited in two axes - axially and transversely – at the base of the beam. Sridharan et al quantified the extent to which a larger tip mass or a longer beam resulted in more geometric nonlinearities and a greater stress amplification in the beam.



## 1.2 Purpose

The FEA and experimental work in this present study build on the aforementioned work, particularly that of Ernst<sup>viii</sup>, by investigating the effect of an electronic component's natural frequency and its circuit card's natural frequency on the stresses seen in the component's lead. This thesis uses sinusoidal excitations for simplicity, and later focuses on the component/circuit card natural frequency ratio of two identified by Kumar, Rhoads, and further validated by Ernst. This study also investigates the effect of changing the phase relationship between the excitation sinusoids - particularly when the frequency ratio of two - and validates FEA simulations with experimental results. This study uses a simplified model of an electronic component, a beam with a tip mass, which is modally similar to a large electronic component.

Finite element analysis in this study is conducted in the time domain to account for geometric nonlinearities. Experimental validation is conducted on a 6-DoF electrodynamic shaker system. The results presented are useful in identifying structures and excitation conditions which will have significant cross-axis synergy. This information is ultimately useful to determine (1) whether a structure will require MDoF testing or if SDoF vibration will be sufficient to assess its durability for multiaxial field conditions and (2) the MDoF vibration profile which will be appropriate for accelerated life testing.

## 2 Experimental Study

### 2.1 Introduction

Finite element results were presented by Ernst<sup>vii</sup> demonstrating the effects of MDoF excitation of a large electronic component in comparison to SDoF excitation. In these finite element simulations, a component model (a cantilever beam with a tip mass) was excited with sinusoidal translational excitation at its base in two orthogonal directions: parallel and perpendicular to the beam's axis. A component

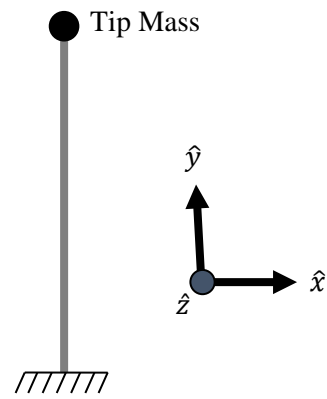


Figure 1: Finite element model of beam with tip mass

model, similar to the one simulated by Ernst, is shown in Figure 1. The coordinate system  $(\hat{x}, \hat{y}, \hat{z})$  and model orientation shown in Figure 1 will be consistent throughout this study unless otherwise specified.

Figure 2 illustrates one set of results presented by Ernst<sup>vii</sup>. The Finite Element model in Figure 1 was used to generate these results. Sinusoidal translational excitation was applied along the  $\hat{x}$  and  $\hat{y}$  axes at the base of the component. The frequency of the excitation in  $\hat{x}$  direction was close to the frequency of the first bending mode (to stimulate worst case resonant motion), while the frequency of excitation in  $\hat{y}$  direction was some multiple (termed the Frequency Ratio) of the frequency in  $\hat{x}$  direction. The frequency of excitation in  $\hat{y}$  was the parameter varied by Ernst in his simulations.

Multiple nonlinear time domain simulations were run at different frequency ratios represented in Figure 2, and different phase differences (from  $0^\circ$  to  $360^\circ$ ) between the  $x$  and  $y$  excitations. Each simulation was allowed to reach steady state. For each frequency ratio, it was observed that the tip displacement and bending stress in the beam's base reached a maximum at some critical phase angle.

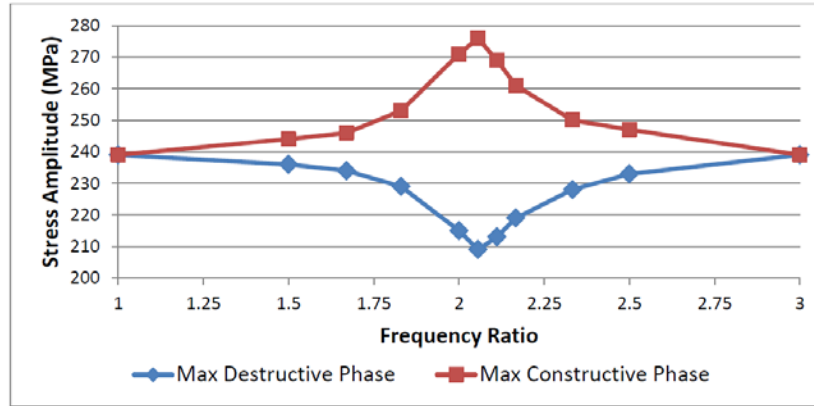


Figure 2: Simulation results presented by Ernst, exciting a component sinusoidally in two axes; changing the ratios of frequencies being excited

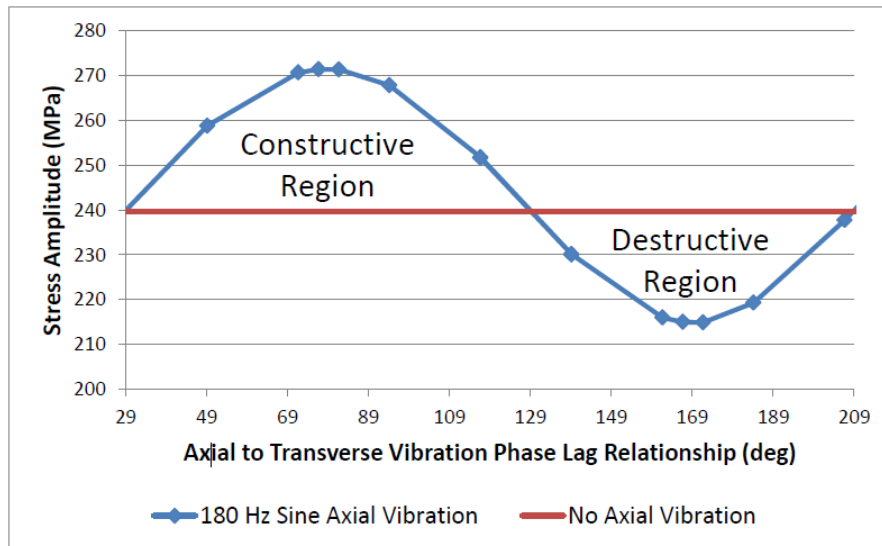


Figure 3: Simulation results presented by Ernst, frequency ratio held at 2 while changing phase between excitaiton signals

The results of these simulations were presented by Ernst<sup>vii</sup>, and are summarized in Figure 2 and Figure 3. Figure 2 shows the peak stresses observed in each set of simulations versus frequency ratio (each frequency ratio was simulated at multiple phases to identify the peak constructive and destructive phase). The stress amplitudes observed vs. phase (at frequency ratio 2) are shown in Figure 3. Ernst concluded that there were significant cross axis interactions when the ratio of excitation frequencies between the  $\hat{x}$  and  $\hat{y}$  axes was 2. This interaction could

either cause stress amplification or stress reduction in the beam, depending on the phase between the excitation sinusoids used in the simulation.

The purpose of this experiment is to validate Ernst's findings (at frequency ratio of 2) . A cantilever beam with a tip mass will be used as a test specimen, similar to the model shown in Figure 1. The beam will be excited near its resonant frequency in  $\hat{x}$ , while simultaneously exciting the beam at twice its resonant frequency in  $\hat{y}$ . Multiple such dynamic experiments will be run, each with a different phase difference between  $\hat{x}$  and  $\hat{y}$  excitation signals. The ultimate goal is to experimentally characterize the effect of excitation phase on the test specimen (at  $\hat{x}$  to  $\hat{y}$  frequency ratio 2). The results will then be validated using geometrically nonlinear finite element simulations, modeling the exact test conditions including the excitation phase.

## **2.2 Test Setup Description**

This section will describe the limitations and reasoning for the selection of the test specimen. Many of the decisions made were made because of limitations in testing equipment.

### 2.2.1 Test Equipment Limitations

Because of the cost of multi-DoF test equipment, equipment selection was limited.

Model selection was greatly dependent on available equipment.



Figure 5: TEAM Tensor

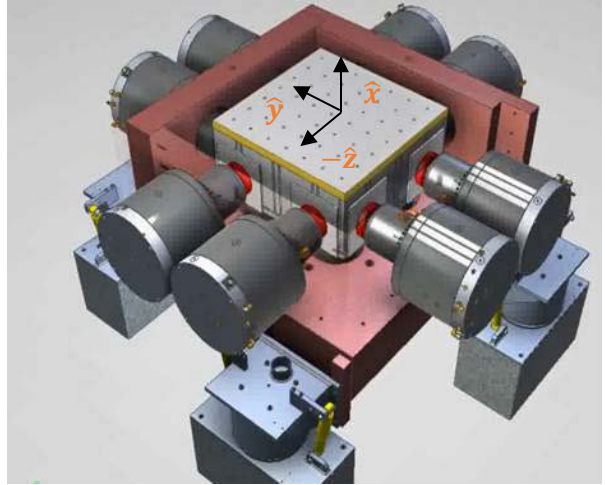


Figure 4: Exploded view of TEAM Tensor shaker arrangement

Experiments were run on a TEAM Corporation TENSOR TE6-900 six DoF shaker table. This shaker table consists of 12 actuators, four oriented in each orthogonal direction. The twelve actuators are connected to an 8x8 inch table, with bearing that permit each shaker to force the table in its axis. In this experiment, only 2 translational DoF were used ( $\hat{x}$  and  $\hat{y}$ ). The shaker is shown in Figure 5 (the moving table is on the top surface of the Tensor), and an exploded view of the shaker table is shown in Figure 4. The black amplifiers on the right side of the Tensor in Figure 5 are not shown in Figure 4.

The  $\hat{x}$  and  $\hat{z}$  (in plane of the table) translations are driven by four shakers in each axis, arranged in two opposed sets of two shakers in each set. In the out-of-plane  $\hat{z}$  direction, all four shakers are mounted underneath the table. Physically this gives control of rotations about  $\hat{z}$  to both the  $\hat{x}$  and  $\hat{y}$  actuators, while rotations about  $\hat{x}$  and  $\hat{y}$  are controlled by the  $\hat{z}$  actuators. This

physical constraint is important to determine the orientation of the test specimen, described later in this section.

The data acquisition equipment and controller used in this experiment for data acquisition and analysis and control was the Data Physics Abacus. The Abacus provides the time synchronized high speed acquisition necessary for both the acquisition and control required in this experiment. The Abacus can be used as a multi-actuator vibration controller or as a data acquisition device.

Multiple Abacus chassis were used in this experiment. Two of the Abacus chassis were used as vibration controllers to control the table. These two Abacus chassis were running Data Physics' SignalStar Matrix controller software. A third Abacus chassis was used for data acquisition. This chassis was running Data Physics' SignalCalc 730 Dynamic Signal Analyzer software. The complete setup is described later in this section.

Four tri-axial accelerometers, DYTRAN 3273A2T, were used for table control. Each of the control accelerometers was located at the corner of a table. An image of this setup is shown in Figure 6. This setup of control accelerometers allows for averaged measurement of all degrees of freedom. In particular, the four  $\hat{x}$  and four  $\hat{y}$  accelerometers were used to measure and control the accelerations in  $\hat{x}$  and  $\hat{y}$ , as well as to null rotations.

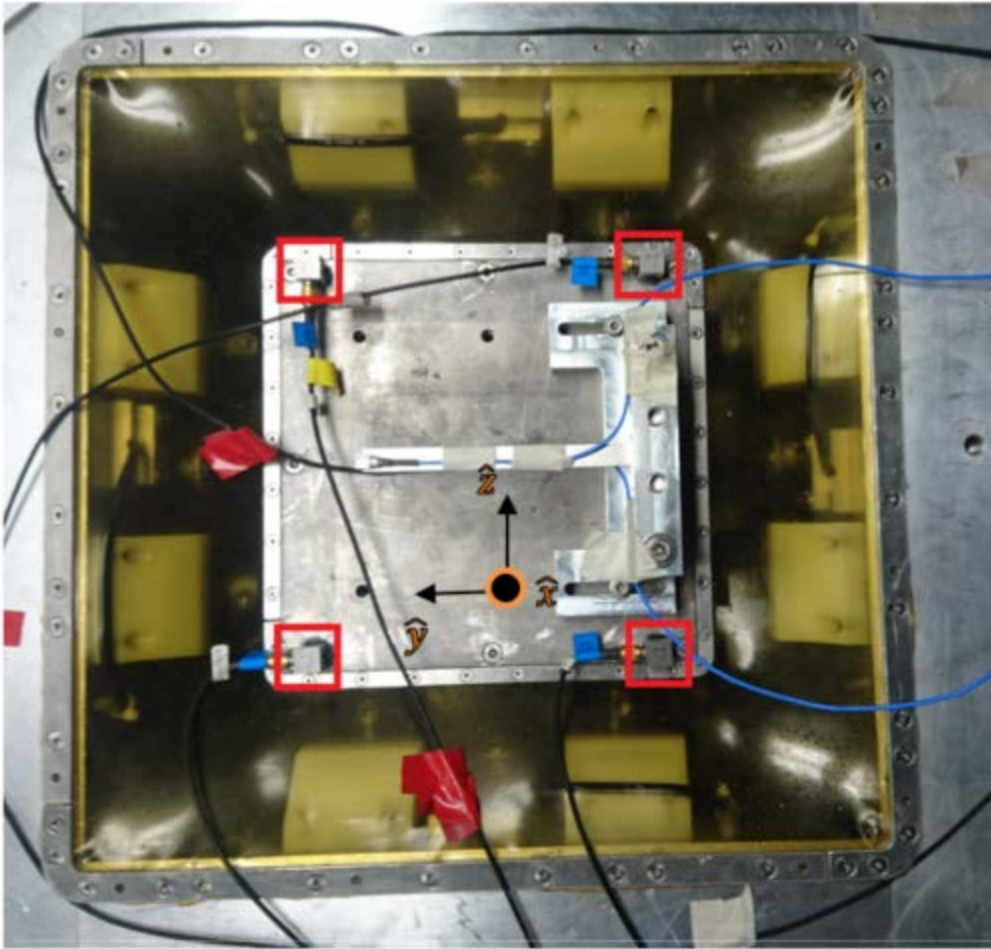


Figure 6: Top down view of shaker table and test specimen/fixsure, with four DYTRAN control accelerometers outlined

The software used to control the shaker system in this experiment is Data Physics SignalStar Matrix. The Multi-shaker Sine control module was used in this experiment. The Multi-shaker sine module is designed to drive multiple actuators in order to achieve multiple degree of freedom control, where a degree of freedom is defined as the motion of an accelerometer (or combination of accelerometers). By using accelerometers in  $\hat{x}$  and  $\hat{y}$  at four different locations – one at each corner of the table (Figure 6) – translations can be separated from rotations, and the controller can generate pure translation with no rotation. This is done by controlling both amplitude and phase at each corner of the table, in the  $\hat{x}$  and  $\hat{y}$  axes.

While SignalStar Matrix's Sine controller can control multiple coupled actuators simultaneously, the software is limited to controlling a single frequency at a time on all the actuators (for sinusoidal excitation). This experiment is intended to test the specimen under harmonic simultaneous biaxial translational excitation, but at a different frequency in each axis. Therefore, a custom test SignalStar Matrix setup was created to allow different frequencies to be run on each orthogonal ( $\hat{x}$  and  $\hat{y}$ ) axis.

Two SignalStar Matrix setups were used – one controlling the  $\hat{x}$  actuators and the other controlling the  $\hat{y}$  actuators. One Abacus chassis was connected to the four  $\hat{x}$  actuators and the four  $\hat{x}$  accelerometers, and another Abacus chassis was connected to the four  $\hat{y}$  actuators and the four  $\hat{y}$  accelerometers. Each Abacus chassis was controlled by a separate instance of SignalStar Matrix controller, running on separate computers. This decoupled setup allowed different frequencies of excitation to be applied in each axis. This setup introduced two uncertainties in the experiment: an uncorrectable overturning moment in  $\hat{z}$  as well as time/phase desynchronization between the two excited axes.

The decision was made to excite the sample's first resonance with the Tensor's  $\hat{z}$  actuators. This implied aligning the beam so that its axis was aligned with the Tensor's  $\hat{x}$  actuators, and its thickness direction was aligned with  $\hat{x}$ . This decision was made to minimize the uncontrollable overturning moment in the experiment, as discussed in the following paragraph. Images of this setup are shown in Figure 6 and in Figure 7.

With the selected beam orientation, beam tip motion during excitation would primarily be in the  $\hat{x}$ . This orientation was selected because the Tensor's  $\hat{x}$  and  $\hat{y}$  controllers can only correct overturning moments their corresponding actuators are physically capable of correcting (described earlier in this section), and also can only correct overturning moments at the



frequency at which their corresponding controller is operating at. The largest overturning moment expected in this experiment is caused by the mass loaded tip motion of the beam (the tip is massive, and sees the greatest accelerations when the beam is excited). Because of the shaker orientation in the Tensor (Figure 4), the Tensor's  $\hat{x}$  actuators correct overturning moments in both the  $\hat{z}$  and the  $\hat{y}$ . Conversely, the Tensor's  $\hat{z}$  and  $\hat{y}$  actuators work together to correct rotations in the  $\hat{x}$ .

Because the Tensor's  $\hat{z}$  actuators correct overturning moments in the other two orthogonal axes, and because the largest overturning moment created (with the chosen beam orientation) is at the  $\hat{x}$  excitation frequency, exciting the beam's first mode with the Tensor's  $\hat{x}$  actuators allows the controller to correct the large overturning moment generated by the beam tip mass vibrating. This is the reason for selecting the described beam orientation: the controller can correct the largest expected overturning moment when set up using this orientation.

Fixturing was selected to orient the specimen (cantilever beam) as described in this section. The fixturing was required to be 'stiff' at twice the resonant frequency of the specimen, the maximum excitation frequency to be tested. In other words, the resonant frequencies of the fixture needed to be significantly higher than twice the resonant frequency of the test specimen. Although the largest overturning moment is corrected by the controller, there is a second smaller overturning moment in the experiment generated by the offset of the fixture and beam being excited by the Tensor's  $\hat{y}$  actuators. This moment was unavoidable and had to be accepted as a part of the experimental errors.

The second error introduced by separating the controllers is the loss of time synchronization. This experiment tests the effect of relative phase between two excitation

signals. Operating the two controllers independently makes it impossible to accurately synchronize their time histories. As a result, the relative phase between global  $\hat{x}$  and  $\hat{y}$  excitations is an uncontrollable variable.

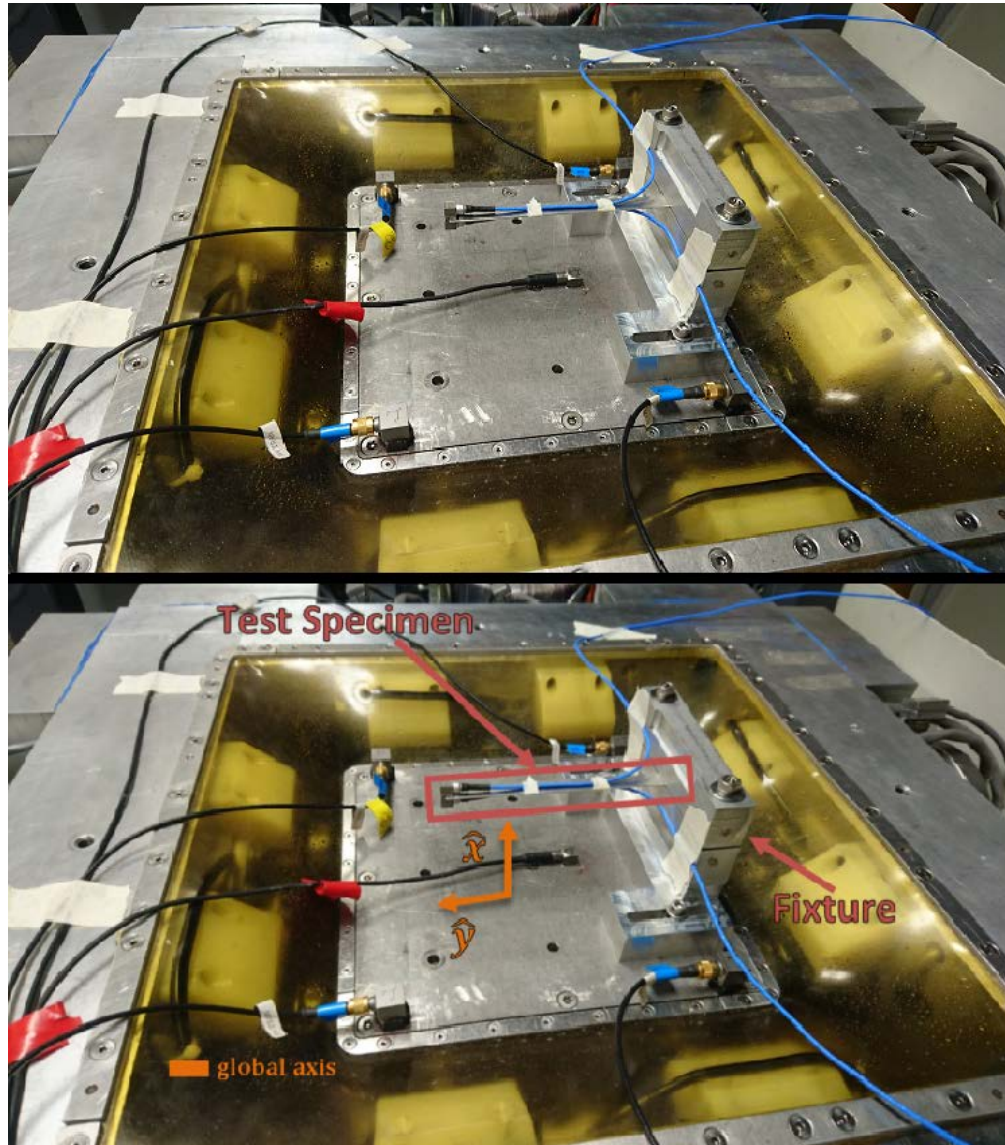


Figure 7: Test Specimen mounted in fixture. The top image is unlabeled, while the bottom image is labeled for clarity

Two instances of SignalStar Matrix were started simultaneously by issuing start commands to SignalStar on time-synchronized computers. After experimenting with the setup, it was realized that the relative phase between excitations was random when the two controllers

were started simultaneously. As such, it was decided to run the same experiment many times – each with a random phase – and compute the phase for each experiment during post processing. The random nature of the initial phase resulted in producing tests with many phase differences, thus covering the complete test domain when a sufficient number of tests had been run. The test matrix is described in Section 2.4

Data Acquisition was conducted using Data Physics SignalCalc 730 software running on a third Data Physics Abacus. Two tri-axial accelerometers were used for data collection. The first accelerometer, a PCB 356A03 was mounted on the tip of the sample to collect tip motion data. A second accelerometer was mounted on the other side of the test specimen to maintain symmetry of the tip mass about the neutral axis; however this accelerometer was not monitored during the experiment. The tip accelerometers can be seen in the foreground of Figure 8.

A third tri-axial measurement accelerometer was mounted at the center of the shaker table. This accelerometer was used to compute the phase angle between the two orthogonal axes for each test. This accelerometer can be seen outlined in red in Figure 8.

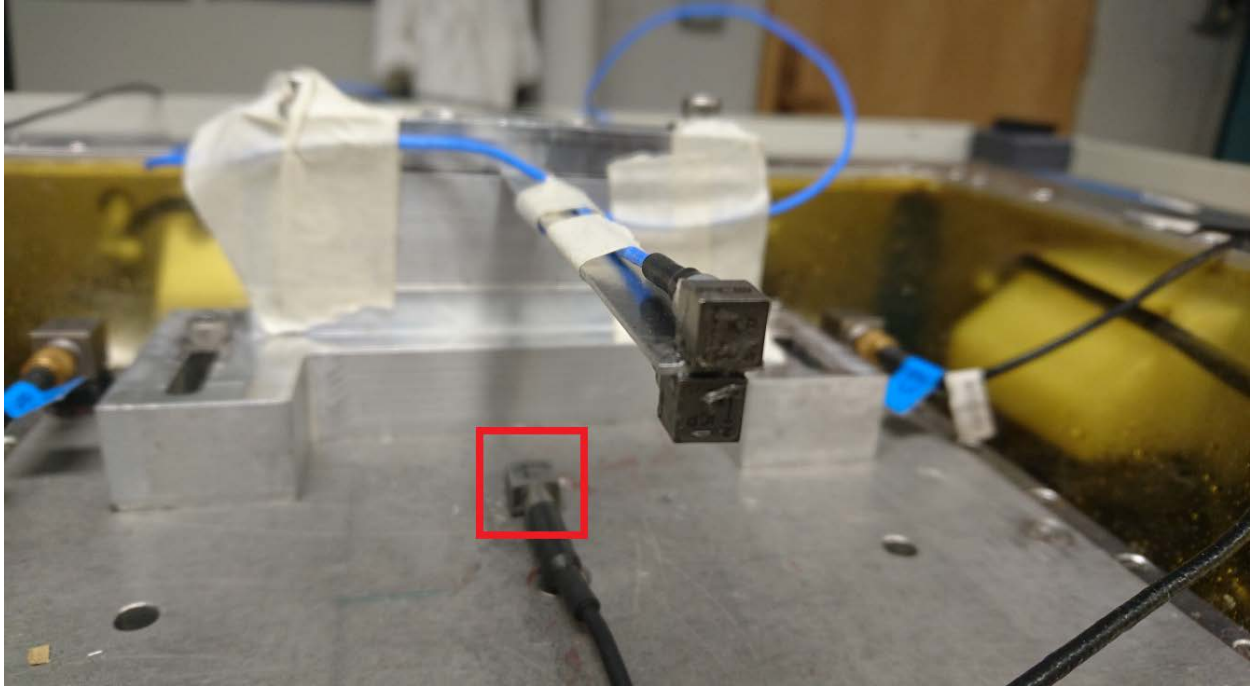


Figure 8: In the foreground, the test specimen with two accelerometers mounted on it (only one was used to measure). On the shaker table, a third measurement accelerometer (labeled in Red) was used to identify the phase offset between the axes' excitations.

### 2.2.2 Data Processing Methodologies

The two tri-axial measurement accelerometers were recorded using the third Abacus chassis and Data Physics' SignalCalc 730 software. The acceleration time signals in  $\hat{x}$  and  $\hat{y}$  from both of the active measurement accelerometers were used to extract data from each run.

This acceleration data from the tip of the specimen was integrated in time to yield tip displacement data. Integration is performed using the trapezoidal rule on high-pass filtered acceleration data. The properties of the filter used is described in Appendix 5.6. Although the filter applies a phase shift to the data, the same shift in time is applied at both 25 and 50Hz. Because steady state measurements are being investigated, this phase shift has no effect on resulting conclusions. Displacement was the output variable of interest, as a beam primarily undergoing unimodal first bending mode deformation observes stresses proportional to tip displacement. Thus, normalized tip displacements are used as a surrogate for stress

amplification, by comparing tip displacements measured during MDoF ( $\hat{x}$  and  $\hat{y}$ ) excitation to those during SDoF ( $\hat{x}$  only) excitation.

The  $\hat{x}$  and  $\hat{y}$  accelerations from the second measurement accelerometer mounted on the shaker table (marked in red in Figure 8) were used to calculate the phase angle between the excitation signals for each test. Computing the phase angle between the  $\hat{x}$  and  $\hat{y}$  axes was done in the FFT domain. For each experiment, the time history of the  $\hat{y}$  accelerations was scanned (incrementing one sample at a time) in 2048-sample blocks until a block in which the  $\hat{y}$  acceleration had zero phase was identified. The phase of the  $\hat{x}$  acceleration was evaluated during that identified 2048-sample block to deduce the relative phase between the excitation signals. Phase of a signal was calculated by evaluating the angle of the FFT of the 2048-sample block at the desired frequency. MATLAB code used to do this is provided in Appendix 5.5.

Data acquisition was done at 2048Hz, which allows for accurate leakage-free FFT measurements at integer frequencies up to 1024Hz (all FFTs were taken using 2048 time samples, or 1sec of data). This set the precedent for deciding model resonant frequency, as described below in Section 2.2.3. With these settings, spectral leakage is not a factor as long as integer excitation frequencies are used.

### **2.2.3 Test Specimen Selection**

In the results presented by Ernst<sup>vii</sup>, the dominant source of nonlinearity is due to geometric effects arising from the large displacement of the tip mass in the cantilever beam model. To maintain modal similarity to the test specimen used in Ernst's study, the test specimen for this experiment was also selected to be a cantilever beam. To maintain simplicity of the model, beams were chosen which could be cut from stock sheet metals. Aluminum 6061-T6 sheet of thickness of 1.016mm (.04 inch) was chosen due to its wide availability. The thin

grade was also useful in keeping the first natural frequency low, which decreases the demand on high speed data acquisition and processing. The properties of the selected material are shown in Table 1.

Density (measured)	$3.9e - 09 \frac{\text{tonne}}{\text{mm}^3}$
Elasticity (measured)	45200MPa
Dimensions	120x10.2x1.1mm

Table 1: Selected test specimen properties

Rather than mounting extra masses on the tip of the beam, it was decided that the accelerometers mounted at the tip of the specimen would serve as the tip mass. The two PCB 356A03 accelerometers used were described in the previous section (one used for data acquisition, the other to maintain symmetry). These can be seen in the image of the test setup shown in Figure 8. The accelerometers were glued onto the tip of the beam, and the cables were allowed to run along the beam's axis.

The width and approximate height of the samples was selected as 10 and 150 mm, respectively, to ensure a large tip displacement when undergoing a low level sinusoidal excitation of .3g applied at the base of the beam model, and to ensure the first bending mode would be near 25Hz. The natural frequencies of the beam equation (with a tip mass) are derived in Appendix 5.7. This derivation was used to select the width and height of the samples. Extra height was added to allow the beam to be clamped into the fixture. Each test specimen length was tuned (by sliding more or less of the sample into the clamping fixture) prior to experimenting, to ensure the first resonance lies exactly at 25Hz. This process is outlined in Section 2.2.4.

25Hz was chosen as the first bending mode frequency primarily for data acquisition and processing reasons. 2048 samples of 2048 Hz-sampled time signals would be used for FFT computation in post processing. This combination requires an integer frequency of motion to prevent spectral leakage and avoid the need for a window function. Furthermore a sampling frequency of 2048Hz provides a phase accuracy of  $4.5deg$  at 25Hz, which is sufficient for this experiment.

A complete test specimen mounted in its fixture is shown in Figure 9.

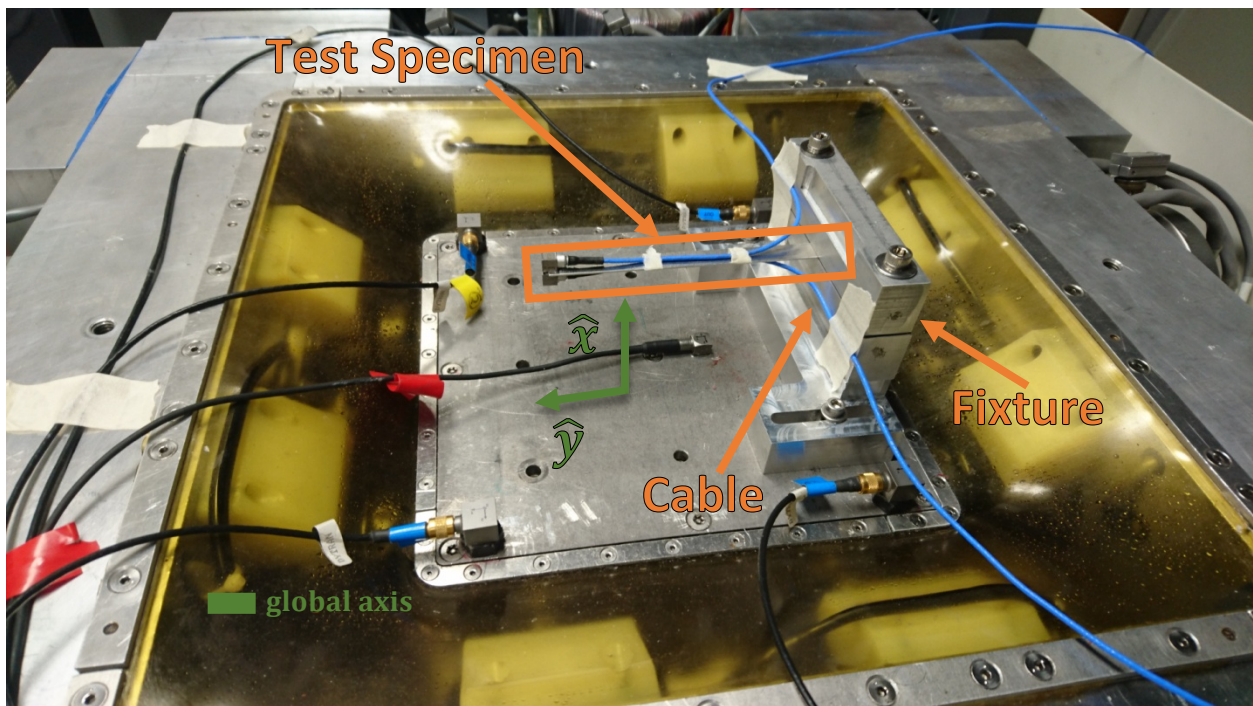


Figure 9: Test specimen set up on TEAM Tensor

#### 2.2.4 Test Specimen Calibration

As described earlier in this section, each model was required to be tuned such that its resonance was exactly 25Hz. This was accomplished by changing the length of the beam which was clamped by the fixture. Resonant frequency was measured by deflecting the tip of the beam and measuring the free response. The length of the beam was modified until the damped

resonant peak was measured to be 25Hz. Due to the low damping ratio in the test specimen, undamped and damped natural frequencies were off by less than 1%. Damped natural frequencies were measured by perturbing the specimen and analyzing the free response, while natural frequencies were predicted by the analytical solution of the beam equation (with a tip mass) presented in Appendix 5.7.

### **2.3 Test Procedures and Data Acquisition Setup**

After a specimen is mounted and calibrated, it can be used for many experimental runs.

Each run consists of two steps:

1. SDoF excitation
2. MDoF excitation.

To begin Step 1, excitation was applied in the  $\hat{x}$  direction until steady state was reached. After steady state was observed, Step 2 was started by adding  $\hat{y}$  excitation without stopping the  $\hat{x}$  excitation. Once steady state motion was observed for the MDoF case, the excitation was terminated and the run was over. Steady state was defined as less than 0.1g variation of the peak acceleration measured at the tip of the beam over two seconds ( $50 \hat{x}$  cycles).

It is important to note that each run consisted of a SDoF and a MDoF test. Although the same SDoF response is expected for every run, material fatigue plays a role over time. Running SDoF excitation before each MDoF test minimized the effect of material fatigue. However, this was not sufficient to completely eliminate the effect of material fatigue. It was decided to discard a specimen if during its  $\hat{x}$  only excitation, the peak tip acceleration was off by over 5g compared to tip response when the sample was new. SignalCalc Dynamic Signal Analyzer software allows for real-time viewing of live data, so the decision on whether to discard a sample was made during the test run (post processing was not required for this decision).



Time history measurements from the measurement accelerometers described in Section 2.2.2 were measured by SignalCalc 730 during both the SDoF and MDoF excitation conditions. The resulting acceleration time histories represent the motion at the tip of the beam and the motion at the center of the shaker plate. The  $\hat{x}$  time history measured during SDoF excitation condition was integrated twice to yield displacement during SDoF excitation. The  $\hat{x}$  time history measured during MDoF excitation condition was integrated twice to yield displacement during MDoF excitation. The peak displacement calculated from the MDoF excitation was normalized by the peak displacement calculated from the SDoF excitation to measure amplification for that run. Because of the unimodal nature of the beam displacement, the tip displacement amplification is considered to be an adequate surrogate of the stress amplification expected at the base of the cantilever beam. All measurements were done after the beam had reached steady state.

The  $\hat{x}$  and  $\hat{y}$  acceleration time histories measured during the MDoF excitation from the accelerometer at the center of the plate were processed using the methodology described in Section 2.2.2 to determine the phase of that test.

The tests were controlled using two SignalStar Matrix controllers running on Data Physics Abacus hardware. The Matrix's multi-shaker sine controller software is not intended to operate at multiple frequencies at a time, so one controller was connected to the four  $\hat{x}$  accelerometers and was used to control the  $\hat{x}$  excitation. The other was connected to the four  $\hat{y}$  accelerometers and was used to control the  $\hat{y}$  excitation.

In SignalStar Matrix, a sine function of desired amplitude and frequency can be defined at each control accelerometer location. In addition, a desired relative phase between each control accelerometers can be defined. This is not the relative phase between axes (which is

uncontrollable), but rather the relative phase between the four  $\hat{x}$  accelerometers (or the relative phase between the four  $\hat{y}$  accelerometers) These relative phases were defined as 0 for all cases, as nonzero phase between any of the accelerometers aligned in the same axis would imply a rigid body rotation.

SignalStar Matrix requires specifying the number of linearly independent degrees of freedom to prevent over-actuation in systems (such as the Tensor) that have more shakers than free degrees of freedom. Because of the Tensor's shaker arrangement (Section 2.2.1), the rank (number of linearly independent degrees of freedom) of the  $\hat{x}$  excitation in the Matrix software (actuated by the TEAM Tensor's  $\hat{x}$  actuators) was 3, since the Tensor's  $\hat{x}$  actuators control translation in the  $\hat{x}$ , as well as rotation in  $\hat{y}$  and  $\hat{z}$ . The rank of the  $\hat{y}$  excitation matrix was set to 2 in SignalStar Matrix, as the Tensor's  $\hat{y}$  axis affects translation in  $\hat{y}$  as well as rotation about the  $\hat{x}$ .

It should be noted that there were many challenges in running this experiment, and care had to be taken to ensure consistent results. The test methods were iteratively improved, each time identifying new disturbances that affected measurements. Only the final results are presented in this paper. One of the sources of errors was the distributed mass of the accelerometer cables. The cables were secured with masking tape to the length of the beam, and bent sideways at the beam's base, to avoid the cable being compressed and stretched in its axis. The cable also could not be left loose, as it could generate inertial forces and result in sporadic motion of the cable. Bending the cable sideways at the beam's base (labeled as "cable" in Figure 9 allowed for shear deformation of the cables as the beam oscillated, which minimized the resistance force.

## 2.4 Test matrix

The goal of these experiments is to investigate the effect of excitation phase on beam tip displacement, at the frequency ratio of two. Because Ernst's FEA simulation results yielded low amplification at other frequency ratios (and because of the complexity of the experimental setup), only the frequency ratio of two was chosen for the experimental part of this investigation.

Sufficient experiments were needed to cover the entire phase domain 0-180° (at frequency ratio 2, 180-360° are mathematically identical to 0-180). Five test points are sufficient to cover the phase domain (average spacing of 36°). However because the actual phases tested were random, a repeat factor of 4 was used. Twenty test points were run to ensure repeatability of the experiment. The test matrix is shown in Table 2.

X excitation Frequency (Natural frequency of specimen)	X excitation level	Y excitation Frequency (Natural frequency of specimen)	Y excitation level	Phase	Repeats
25	.3g	50Hz	2g	TBD	20

Table 2: Experimental test matrix

### 2.4.1 Test Results

Experimental test results are represented in this section. These results are also validated in Section 3.6.1 using finite element models and simulation.

### 2.4.2 Data

The first step after completing the 20 sets of tests was to compute the phase angles in each of these tests, using the method described in Section 2.2.2. A section of the time history of the  $\hat{x}$  and  $\hat{y}$  accelerations from the accelerometer at the center of the shaker table are shown in Figure 10. These were the measurements made in test number 1.

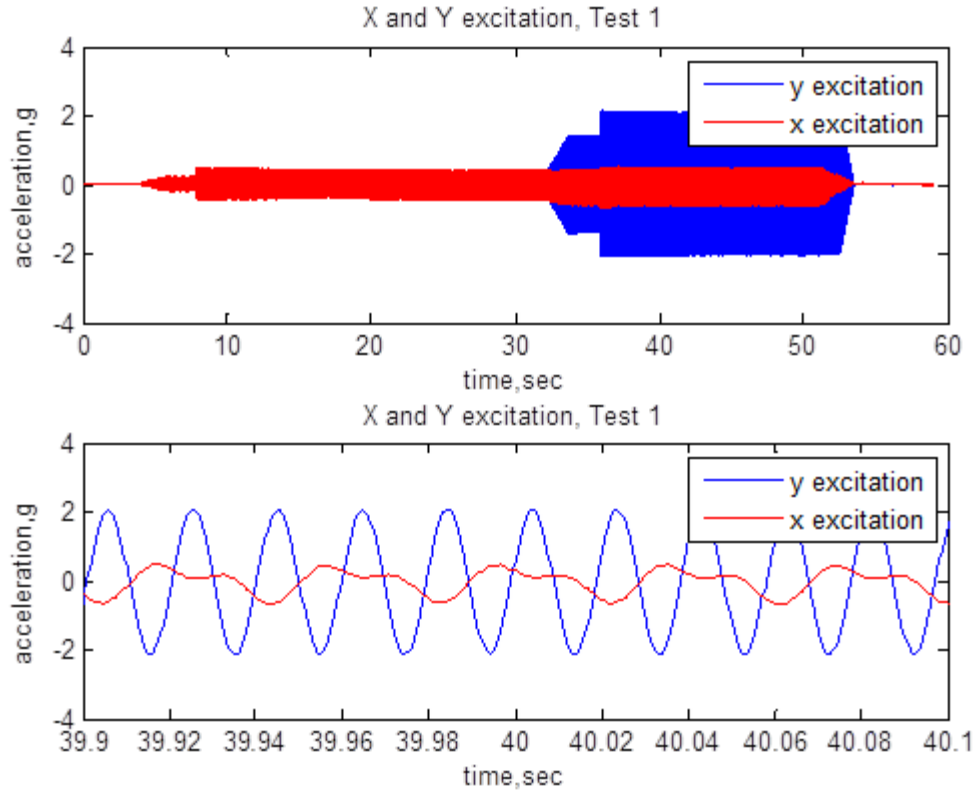


Figure 10: Time history of the  $\hat{x}$  and  $\hat{y}$  accelerations from the accelerometer at the center of the shaker table

In the top plot of Figure 10, the excitations applied during the entire run can be seen: The initial SDoF  $\hat{x}$  excitation before 30sec, and both the  $\hat{x}$  and  $\hat{y}$  MDoF excitation case from 30-50sec. The effect of the uncontrollable overturning moment is apparent as distortion in the red signal of the bottom plot of Figure 10. As stated earlier, this is one of the sources of experimental noise that has been considered to be unavoidable in this study. It appears that the relative phase between the red  $\hat{x}$  signal and the blue  $\hat{y}$  is difficult to extract based on the plot, however the frequency domain method described in Section 2.2.2 is not affected by the overturning moment.

The following is an example illustrating how phase relationships were extracted from the  $\hat{x}$  and  $\hat{y}$  excitations signals shown in Figure 10. The  $\hat{x}$  and  $\hat{y}$  excitations during the multi-axis excitation portion of each test case (Figure 10,  $t > 40$ ) were searched through until a 2048-sample segment was found in which the  $\hat{y}$  excitation was found to have 0 phase. The  $\hat{y}$  acceleration

from Figure 10 (test case 1) starting at a point of 0 phase, along with its FFT are shown in Figure 11. Note the phase of the 50Hz bin is approximately  $0^\circ$  ( $1.9^\circ$ ).

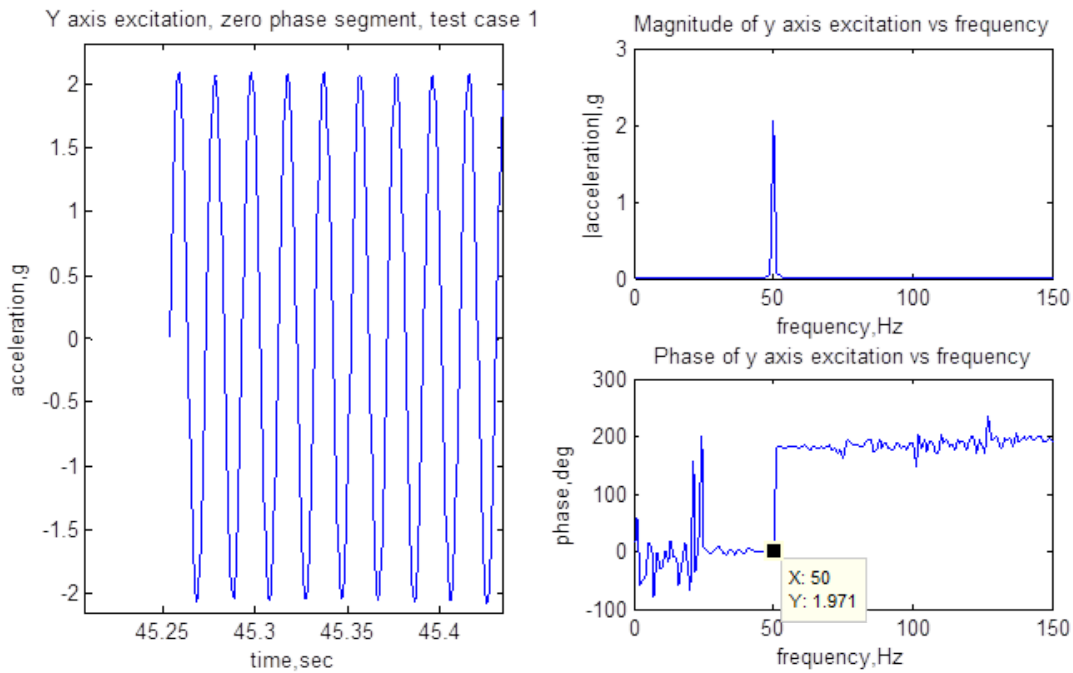


Figure 11: Zero phase segment of Y acceleration, and its frequency components

The  $\hat{x}$  excitation for the same test case 1 during the same 2048-sample span was then converted to the frequency domain using the FFT. A plot for the 2048 sample of  $\hat{x}$  excitation along with its frequency components (magnitude and phase) are shown in Figure 11. The phase of the 25Hz bin ( $15.7^\circ$ ) was noted as the excitation phase of this test case 1.

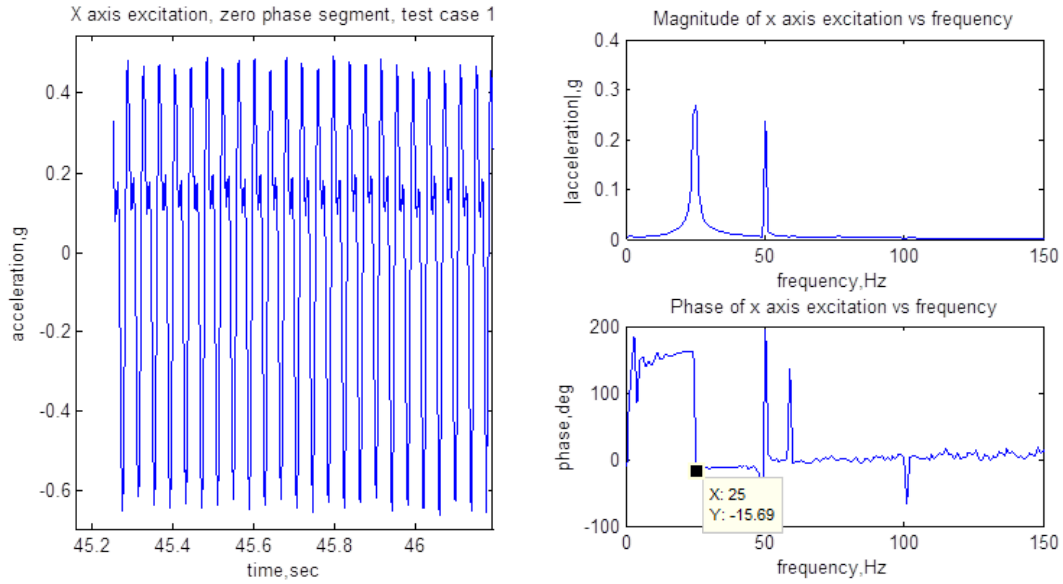


Figure 12: 2048-sample of measured X axis excitation, corresponding to the Y axis excitation in Figure 11

The data shown in Figure 10, Figure 11, and Figure 12 corresponds to an initial phase of  $15.7^\circ$ . Similarly, the resulting phase angles tested in Tests 1-20 are given in Table 3, as demonstrated by the above example and as completely described in Section 2.2.2.

Test Number	Phase (°)
1	15.7
2	51.5
3	76.2
4	71.7
5	0
6	111.3
7	115.8
8	174.8
9	165.8
10	116.5
11	140.4
12	17.9
13	40.3
14	44.1
15	159.1
16	71.0
17	129.9
18	0
19	14.9
20	17.2

Table 3: Phase angles measured from test data

Next, the amplification for each run was computed from test data. A sample of the tip acceleration data (corresponding to Test 1) is shown in Figure 13. In this plot, the SDoF and MDoF responses can be clearly seen, the SDoF response before 30sec and the MDoF response from 30-50sec. This time history was filtered and integrated twice, as described in Section 2.2.2. The peak displacement value from the steady-state SDoF portion of the signal (around 30sec) and the peak displacement from the settled MDoF portion of the test are evaluated. Amplification for a run is defined as the ratio of the peak values of the stable MDoF tip displacement and the SDoF tip displacement observed in that run. The amplification measured from Figure 13 (Test case 1) was measured to be 1.36: The peak displacement observed in the steady state response to the uni-axial excitation ( $20 < t < 30$  in Figure Figure 13) normalized by the

steady state response to the multi-axial excitation ( $45 < t < 50$  in Figure Figure 13). Note the acceleration data shown was filtered and integrated in time to compute displacement values.

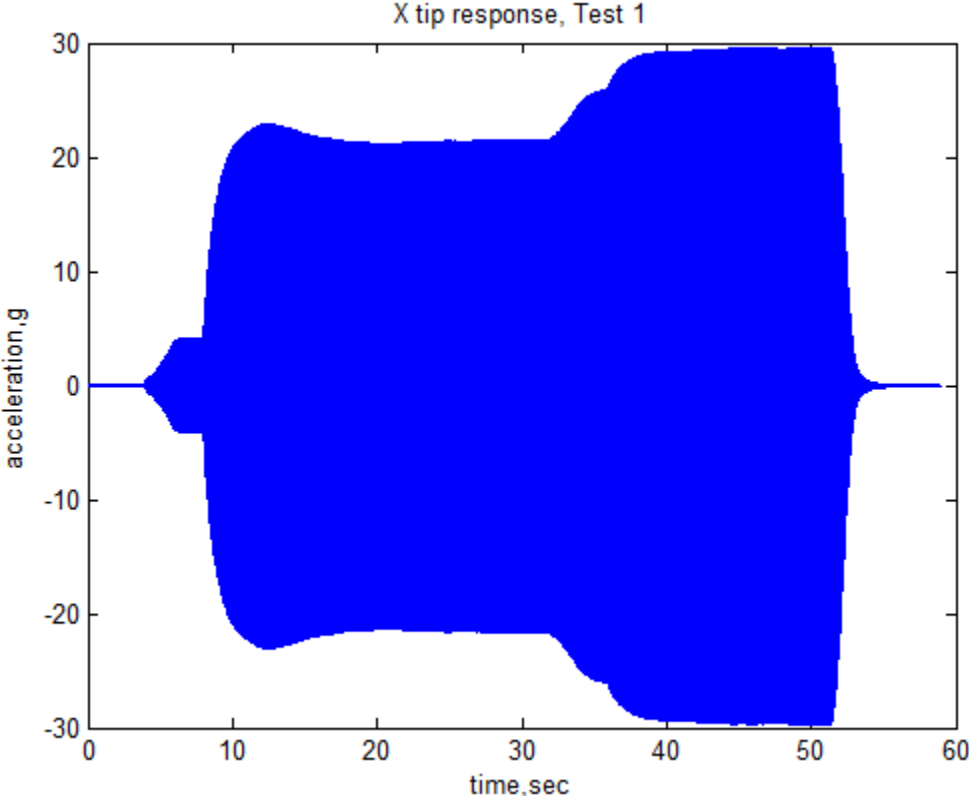


Figure 13: X Response of beam during Test 1.  $t < 30$  represents the beam's tip response under single axis excitation, and  $t > 45$  represents the response due to combine multi-axis excitation. The X axis excitation was held constant once started at  $t=5$ , the Y axis excitation was added after  $t=30$ , after the X-axis-only response had reached steady state

The resulting amplification factors for all tests 1-20 are plotted versus phase in Figure 14.



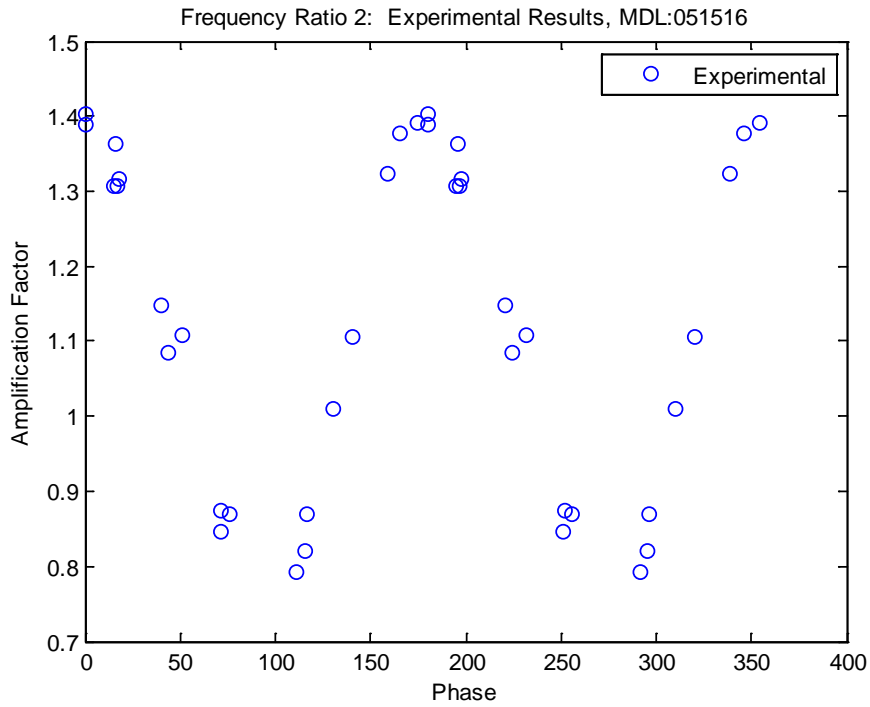


Figure 14: Experimental results, processed, Peak steady state stress vs. excitation phase at frequency ratio 2

Patterns similar to those seen in Ernst's finite element experiments<sup>vii</sup> conducted at frequency ratio two are observed. Most notably, it is observed that there are some phase angles which amplify stress, and other phase angles which reduce stress. To further validate the experimental results, finite element simulations mimicking the test specimen and excitation conditions were run. This process and the resulting amplification factors are presented in Section 3.6.1.

### **3 Finite Element study on effect of phase and frequency ratio**

This section describes the finite element study conducted. In this section, a nonlinear beam model is simulated with harmonic bi-axial excitation, and the stress response observed at the beam's base are analyzed. Excitation frequency ratio and relative excitation phase are analyzed.

#### **3.1 Introduction**

In his paper, Ernst ran finite element simulations for sinusoidal excitation of a cantilever beam along two orthogonal axes: one along the beam's longitudinal axis and the other along an orthogonal transverse direction <sup>vii</sup>. He found a nonlinear coupling when the excitation frequency ratio was 2; that is the beam was excited at a frequency  $F$  in an off axis direction, and at frequency  $2F$  along the beam's axis. In his experiments, the frequency  $F$  was near the frequency of the beam's first bending mode. Ernst also found a relationship between the phase offset between the two sinusoidal excitations and the nonlinear coupling.

Ernst's finite element study was correlated with experimental results, presented in Section 2.4.1. However, a more complete understanding of the effect of phase and frequency ratio is desired. This finite element study will use a model similar to Ernst's model, representing a large electronic component, and will further parametrically investigate the effects of sinusoidal excitation frequency ratio and phase. Following this, a finite element model exactly mimicking the experimental test specimen used in Section 2.2 will be simulated in order to further validate experimental results of Section 2

#### **3.2 Finite element model description**

This section will describe the finite element model used in this section.

The finite element model used in this section is pictured in Figure 15. All references to dimensions will be in mm, mass in metric tonnes, material stiffness moduli in MPa and time in seconds. Responses are therefore in mm and resulting stresses are in MPa.

The model is selected to be simple, yet capable of capturing some of the key dynamics of a large electronic component's first bending mode. For this reason, a beam (representing the component lead) with a tip mass (representing the mass of the component) was selected, as shown in Figure 15.

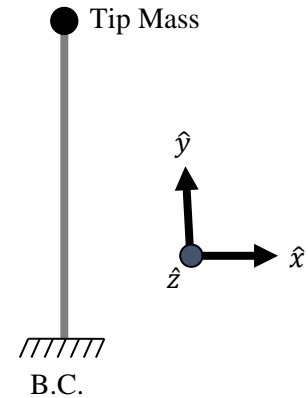


Figure 15: FEM Model of beam with tip mass

This model consists of a beam oriented such that its axis aligns with  $\hat{y}$ . The “base” of the beam is at the origin and the beam has a point mass at its free end. The length of the beam is 15mm, and the mass 1.5E-5 tonne. The beam consists of 10 shear deformable beam elements. The beam's material is Aluminum 6061-T6, and material properties can be found in Appendix 5.1. The beam had a circular cross section with radius .5334mm

Rayleigh damping was applied ( $\alpha = 100$ ) to ensure that the simulations settled in an appropriate simulation time. The Rayleigh modal damping formulations used by the finite element solver are shown in Appendix 5.2. In this section's simulations, results are compared across simulations, and not to physical test specimens. Thus, the damping values selected are acceptable as long as sufficient energy remains in the system (post settling) to measure results. This is because Rayleigh Damping computes a modal damping ratio for each mode from  $\alpha$  and  $\beta$  (equation in Appendix 5.2). This allows a different damping ratio to be applied to each mode. This section's simulations only focus on a single mode of vibration, and thus the ratio of  $\alpha/\beta$  in the Rayleigh damping formulation is irrelevant. Thus, for simplicity,  $\beta$  was set to zero.

In this section, excitation was applied to the model at the base of the beam (Figure 15)Figure 15, also labeled as the B.C. Boundary conditions were applied as prescribed displacements at the base of the beam. For simplicity, the beam was provided translational

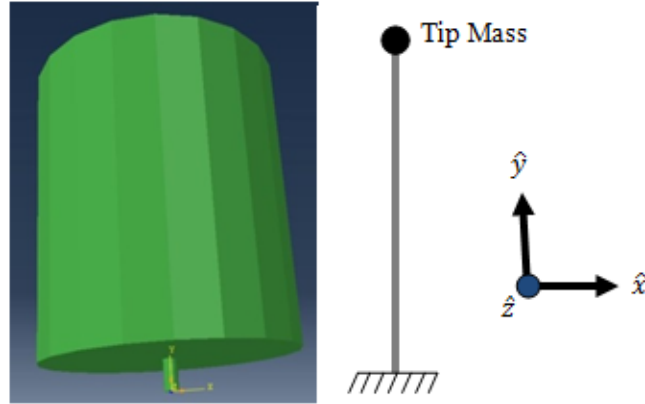


Figure 16: FEM model of large electronic component (left, A) and simplified component model (right, B)

sinusoidal excitation only along  $\hat{x}$  and/or  $\hat{y}$  axes. Because of symmetry, this eliminates any translations in  $\hat{z}$  direction and any rotations about  $\hat{x}$  or  $\hat{y}$  for the entire model. All simulations were run in the time domain to account for geometric nonlinearities. During the simulations, time histories of several selected variables were saved at several selected locations. These included displacements at the tip of the beam as well as stresses at the base of the beam. Both of these values are saved at locations where they are the greatest in magnitude for the first mode of vibration.

This particular model was chosen to represent the dynamics of the first mode of vibration of a large electronic component. A picture of a large electronic component (an insertion mount inductor) and of the equivalent beam model are shown in Figure 16 for comparison. The large



Figure 17: First bending mode of component model

inductor model shown in Figure 16 is not a part of this study. A beam (length and tip mass of  $15mm$  and  $1.5E - 5tonne$ , respectively) was chosen in this study as an equivalent model to mimic the dynamics of such inductors. A linear modal analysis of the model used in this simulation is shown in Figure 17 . This shows that the first bending mode of our model occurs at a

frequency of 80Hz. This corroborates with an analytical solution of natural frequency, derived in Appendix 5.7, of a beam with a tip mass.

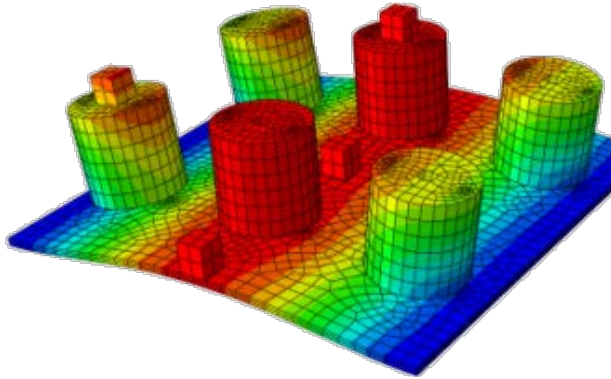


Figure 19: First bending mode of circuit card with large electronic components mounted on it

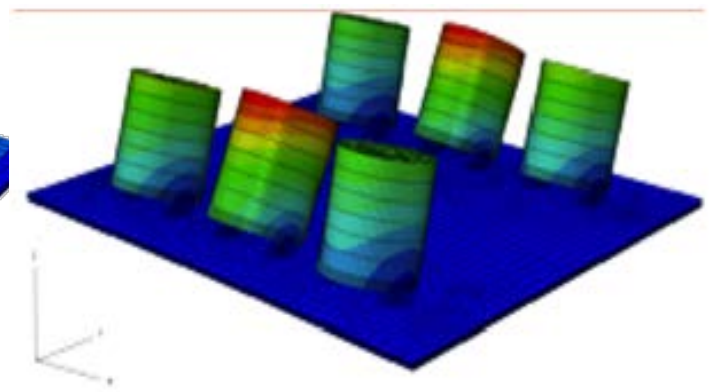


Figure 18: First bending mode of electronic components excited while mounted on a circuit card

A component mounted on a circuit

card experiences accelerations which excite the component's first bending mode. This happens when the circuit card is excited in its plane, or when out-of-plane response of the circuit card rotate the base of the components mounted on it. A circuit card being excited in its plane is illustrated in Figure 18. The bending mode illustrated will be excited as long as the circuit card's in-plane motion (and/or base rotation due to out-of-plane motion) has significant energy at or around the frequency of the component's first bending mode. In order to simplify test conditions, the circuit card dynamics were ignored and translational excitation was applied directly to the base of the component model in the transverse direction (Rotational excitation is not used in the present study because the components shown in Figure 18 and 18 had very high flexural stiffness in the direction of the principal rotation). In order to generate a worst-case test condition, the component model was always excited slightly off the natural frequency (at 95% of its natural frequency ,76.9Hz in  $\hat{x}$ ), in order to avoid the excessively large gain at the resonant frequency.

The components shown in Figure 18 also experience acceleration in their axial direction due to the circuit card vibrating out of plane. As an example, the first bending mode of the circuit card is illustrated in Figure 19. As measured at the component's base, this motion's dominant frequencies will be those of the circuit card's bending modes. To simplify test conditions,  $\hat{y}$  excitation was applied directly to the component's base, and the component model is excited at a single frequency in  $\hat{y}$ , representing the circuit card's first bending mode frequency.

The simplifications to excitation outlined in the previous two paragraphs allow investigation of the effects of circuit card architecture and bending mode by modifying the  $\hat{y}$  excitation frequency applied to the component model. Because the  $\hat{x}$  and  $\hat{y}$  excitations are applied independently, the effects of changing the initial phase of each excitation signal can also be investigated. This is of interest as in the real world, the phase between the transverse and axial accelerations seen at the base of a circuit card will generally be unrelated.

The underlying forces which give rise to the nonlinearity being investigated are visualized in Figure 20. This figure shows the electronic component model being excited in the manner described in this section. The x-excitation of the base causes a bending moment due to the mass M, causing vibration in the x direction. As the tip displaces in  $\hat{x}$  direction from the center line, simultaneous y-excitation of the base causes  $\hat{y}$

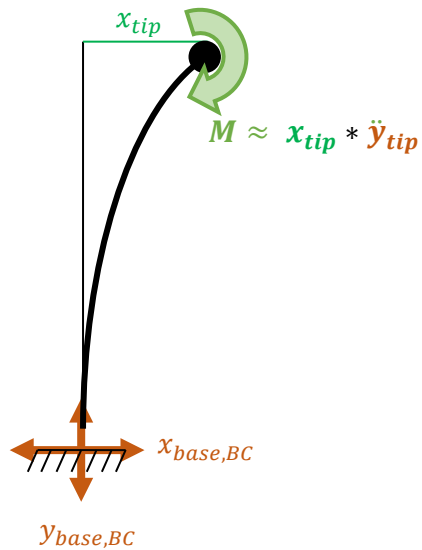


Figure 20: Large electronic component model undergoing bi-axial excitation, with nonlinear moment drawn

acceleration of the mass  $M$ , thus inducing an additional a moment at the base of the beam. This additional bending moment can only be captured by nonlinear finite element analysis (FEA), as its magnitude depends on the current displacement of the beam and mass. In contrast, linearized FEA is based on the initial geometry, and hence cannot capture this additional bending moment.

### **3.3 Simulation software**

Abaqus finite element solver was used to model and run the simulations. All beam elements were shear deformable Timoshenko beam elements (B23 elements in Abaqus). Nonlinear computations due to kinematic nonlinearities were enabled in Abaqus since the phenomenon being investigated is caused by large displacement. All simulations were run in the time domain. This greatly increased the time required for simulations, however frequency domain simulations would have failed to capture these nonlinear effects.

### **3.4 Simulation test matrix**

The purpose of this simulation is to investigate the effect of circuit card architecture and excitation conditions on stresses seen in the lead of an electronic component which resides on the circuit card. As seen in Figure 18, a component on a circuit card has its first mode excited by excitation in the plane of the circuit card. If a real world broadband random excitation were applied in the plane of the circuit card, the component would vibrate primarily at its resonant modes. The frequency range of realistic broadband excitation (caused by vehicles, etc) typically contains energy at low frequencies, around 0-500Hz. As such the first bending mode of the component is most likely to be excited, as it is the mode of vibration with the lowest frequency. To simplify the test procedure and to produce repeatable steady state results, sinusoidal

excitation was applied to the base of the component in the  $\hat{x}$  direction (at 95% of the natural frequency of the component, as discussed earlier).

A circuit card as shown in Figure 18 is relatively rigid in its plane at low frequencies. As such, the in plane excitation seen at the base of any component on the circuit card will be similar to the in plane excitations applied to the boundary conditions of the circuit card, as a first-order approximation. An acceleration of 5.0g was used in the transverse direction. This acceleration level was chosen because it is an acceleration value that could reasonably be experienced by electronic cards. The level of 5g is within the peak value of the electronics screening profile recommended in the U.S. Navy's manufacturing screening program, NAVMAT P9492. The excitation applied in this set of finite element simulations, however, is a single frequency and will generate a state not expected by NAVMAT P9492. This was intentional and intended to create a worst case scenario.

Broadband excitation applied to a circuit card in its out of plane direction causes the circuit card to vibrate primarily at its resonant bending modes. This vibration causes an axial excitation and a rotational excitation at the base of the components residing on the circuit card. As discussed earlier, the flexural stiffness of the components shown in Figure 18 is quite high in the direction of the principal rotation, hence only the axial excitation was considered in the following simulation (and in the experiments of Sec 5). Just as with the component, the first bending mode of the circuit card is most likely to be the dominant mode of vibration under typical realistic use conditions. The frequency of the first mode of vibration depends on the size, material properties, boundary conditions, and mass distribution on the circuit card. In general, the first bending mode frequency will vary greatly from one circuit card to the next. To examine the effect of bending mode frequency on the stresses seen in the component, the frequency for



the axial excitation of the component will be parametrically varied to simulate the effects of different circuit cards. These frequencies are normalized by the component's first bending mode frequency, as shown in Table 4.

<b>Transverse excitation frequency</b>	<b>Axial excitation frequency ratio (frequency)</b>
76.9Hz	1 (76.9Hz)
76.9Hz	1.25 (96.125)
76.9Hz	1.5 (115.35Hz)
76.9Hz	1.75 (135.58Hz)
76.9Hz	2 (153.8Hz)
76.9Hz	2.25 (173.0Hz)
76.9Hz	2.5 (192.25Hz)
76.9Hz	2.75 (211.47Hz)
76.9Hz	3 (230.7Hz)

Table 4: Excitation frequencies used in simulation

Circuit cards are not rigid in their out of plane direction. When a circuit card is excited at its first bending mode frequency, a component on the circuit card will see amplified accelerations. The level of amplification a component sees will depend on the circuit card's bending mode shape, as well as the component's location on the circuit card. Based on the acceleration level of 5g chosen in  $\hat{x}$  direction, an amplification of 2 was selected for the peak  $\hat{y}$  acceleration applied to the component.

While dominant frequencies and amplitudes of motion are determined from mode shapes and typical acceleration levels, the phase relationship between the excitations along the two axes is generally not highly correlated. For certain sinusoidal base excitations with specific frequency ratios, this relationship between the two excitation sinusoids can be generalized by a single phase angle. In order for this generalization to work, the frequencies of excitation must have a LCM; that is they must both be periodic over a given period P. See Appendix 5.7 for a detailed description of sine wave periodicity and characterizing their relationship as a single phase angle.

In this paper, the phase relationship between the  $\hat{x}$  and  $\hat{y}$  excitation signals is always defined as the phase of the  $\hat{x}$  excitation displacement (boundary condition) when the  $\hat{y}$  excitation displacement (boundary condition) has zero phase. This definition was chosen as the  $\hat{x}$  excitation frequency remains the same for every test condition in the test matrix. Because the  $\hat{y}$  excitation frequency is the same or greater than the  $\hat{x}$  excitation frequency, there will be one or more  $\hat{x}$  phases corresponding to zero  $\hat{y}$  phase (see Appendix 5.7 for more details). In the cases of more than one corresponding phase, the extras are mathematically identical to the first. However repeat excitation conditions are still simulated in this experiment, as a phase range of 0-360 degrees was used for each frequency ratio.

A list of  $\hat{y}$  excitation phases simulated in this finite element study (for each frequency ratio listed in Table 4) is given in Table 5.

Transverse excitation phase @ 76.9Hz	Axial excitation phase @ $\hat{y}$ excitaiton frequency
0°	0°
30°	0°
60°	0°
90°	0°
120°	0°
150°	0°
180°	0°
210°	0°
240°	0°
270°	0°
300°	0°
330°	0°
360°	0°

Table 5: Excitation phases simulated for each frequency ratio

The complete matrix for this simulation is given in Appendix 5.3.

In order to illustrate the excitation signals used in this finite element study, two samples of applied excitations are shown in Figure 21. These excitation signals (applied as displacement boundary conditions at the base of the beam) correspond to simulation numbers 7 and 53. These two simulations consisted of

frequency ratios of 1 and 2 with phase relationships of 180° and 0° respectively. The excitation signals for other simulations are similar, with the  $\hat{y}$  excitation signal at the  $\hat{y}$  test frequency and the phase of the  $\hat{x}$  signal set to the phase of the  $\hat{x}$  excitation phase for that test.

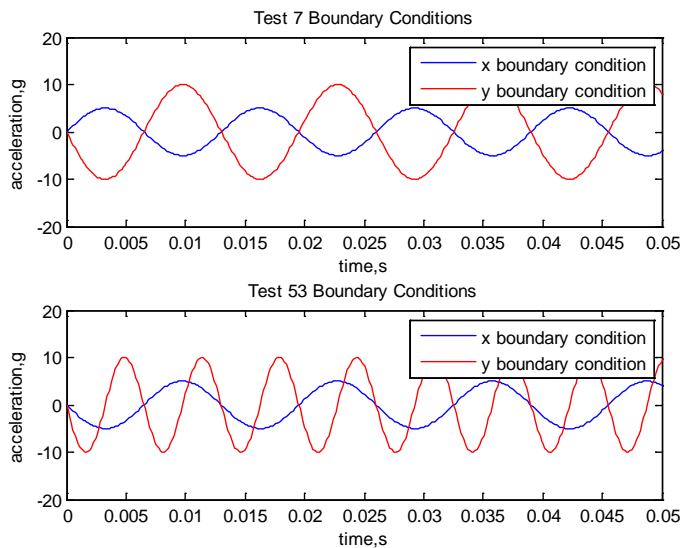


Figure 21: Excitation signals used for test 7 (Frequency ratio 1, phase 180) and 53 (frequency ratio 2, phase 0)

### 3.5 Finite element study results

Ernst<sup>vii</sup>, in his durability tests of tall and heavy electronic components on a circuit card, observed that all components failed at the base of their lead. This conclusion is consistent with the simulation conditions set forth in Section 3.4 in which the primary mode of vibration of the component model is the first bending mode, which induces the highest stresses at the base of the beam. The stresses seen at the base of a beam vibrating at its first bending mode frequency are dependent on the displacement of the tip of the beam. Stresses are the output value of interest as SN curves provide material level relationships between stress cycles and life. For the reasons outlined in this paragraph, either stresses or

displacements can be considered as the output variable of interest.

#### 3.5.1 Simulation Results

Each simulation in the test matrix was a time domain simulation. Because each simulation was started from rest, a transient response was present during the early stages of each

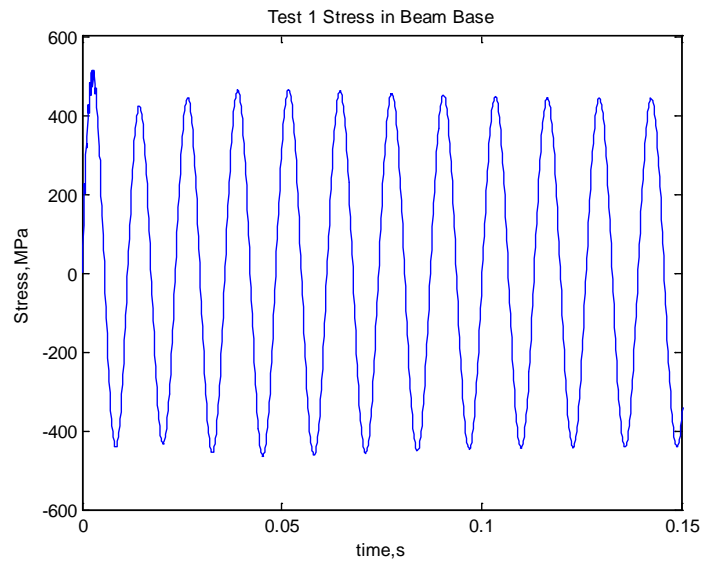


Figure 22: Stress response at base of component model for simulation condition 1

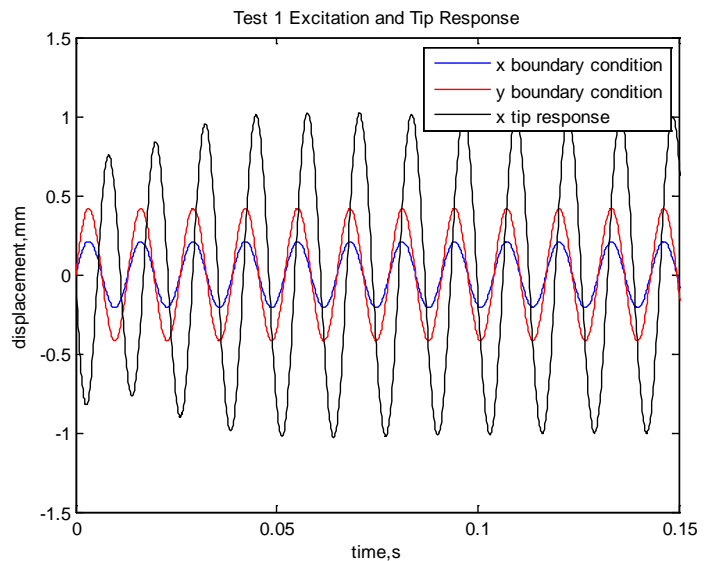


Figure 23: Excitation and response of component for simulation test 1

simulation. The simulation was allowed to run until the transients decayed, and until steady state response was observed. Steady state response was determined by the motion of the tip mass. Simulations were run until the motion of the tip stabilized for a measurable time interval.

An example of the tip  $\hat{x}$ -displacement response history for simulation condition 1 is shown in Figure 23. The black curve represents the  $\hat{x}$  response of the tip when the excitation signals shown in blue and red (for  $\hat{x}$  and  $\hat{y}$  directions, respectively) were simultaneously applied to the model. The corresponding bending stress history seen at the base of the component is shown in Figure 24. The peak value of stress observed in the steady state response for each excitation condition is considered as the output variable from that simulation condition. The peak values were taken because stress response – just as displacement response – is periodic, and

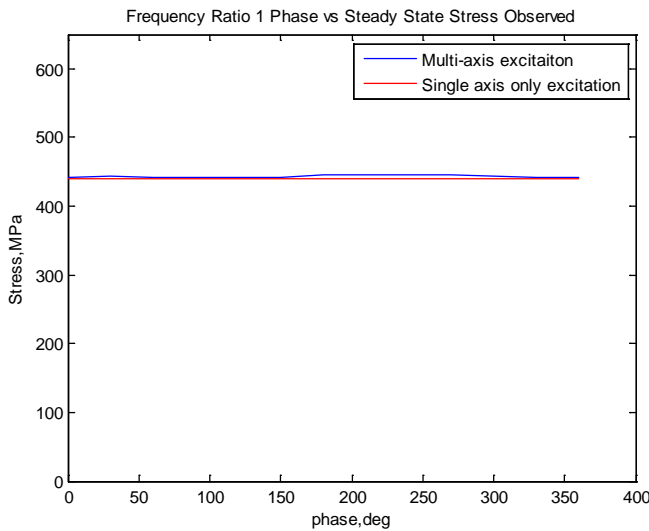


Figure 24: Peak steady state stress response observed in component base, for phase 0-360° and frequency ratio 1. Plot Y axis range set to match other result plots, for comparison purposes

because this peak stress value per cycle is important when assessing cyclic fatigue damage.

The peak stress observed in the steady state responses of simulations 1-13 (frequency ratio 1, all phase angles) were computed and compiled into a single plot of peak stress vs. phase (for frequency ratio 1). This plot is shown in

Figure 24. A baseline stress is also

plotted in red, representing the peak bending stress seen in the component when undergoing single axis  $\hat{x}$  excitation. This was chosen as a baseline for comparison as the purpose of this experiment is to investigate the stress amplification in DoF excitation vs SDoF excitation test

conditions, and because this type of SDoF excitation is most damaging to the component. It is evident that the addition of  $\hat{y}$  acceleration has very little effect on the peak cyclic stress observed in the component lead when the frequency ratio is 1, regardless of excitation phase.

Plots similar to Figure 24 were made for each frequency ratio in the simulation matrix. These plots, for each frequency ratio, are shown in Appendix 5.4. The plots were overlaid onto a single 3D surface plot with frequency ratio on one axis, excitation initial phase on the second axis, and resulting stress amplification on the third axis. Initial phase was applied as described in Section 3.4, and is defined as the phase of the  $\hat{y}$  excitation at a point when the phase of the  $\hat{x}$  excitation is 0 (with excitations defined as displacements). This plot is shown in Figure 25. In this plot, an amplification of 1 implies that the peak steady state stress for that simulation condition was identical to that seen in the SDoF excitation simulation condition. An amplification greater than 1 implies stresses were greater in the MDoF case, and an amplification less than 1 implies stresses were greater in the SDoF case.

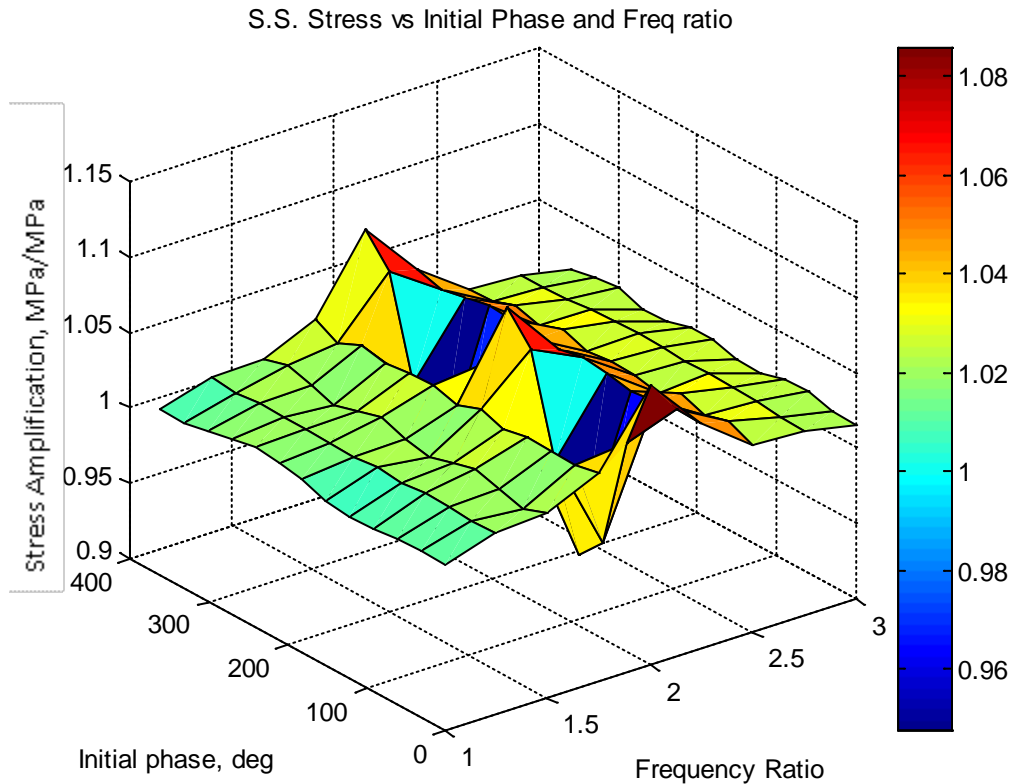


Figure 25: Steady state stress amplification (MDoF/SDoF) observed in all simulations (frequency ratios 1-3, excitation phases 0-360)

The most apparent trend evident from the results is that the addition of  $\hat{y}$  excitation causes large changes in stresses only when the excitation frequency ratio is 2. At frequency ratio 2, there is both stress amplification and stress de-amplification caused by the addition of MDoF excitation (depending on the phase relationship between the two orthogonal excitation axes). The reasons for this behavior are well understood in the literature<sup>vii</sup> and are explained later in this section. Another trend that is apparent from these results is that the peak steady state stresses appear to be periodic as a function of phase. This arises because of the periodicity of the excitation conditions in the simulation matrix. This phenomenon was described in Section 3.4 and in detail in Appendix 5.7.

It is apparent from Figure 25 that the frequency ratio of 2 is of interest, as its nonlinear amplification effects are greatest. Frequency ratio 2 causes the largest stress amplification, as well as stress de-amplification at certain phases, compared to the amplification at any other frequency ratio. A time domain and frequency domain discussion of these results is presented in Section 3.5.2.

### 3.5.2 Interpretation of Simulation Results

This section discusses the underlying physics of the results presented in Section 3.5.

#### 3.5.2.1 Time domain interpretation

This subsection focuses on frequency ratio two. It is intended to explain – in the time domain – the reason a frequency ratio of two provides large cross-axis interactions, as was observed in Section 3.5.1.

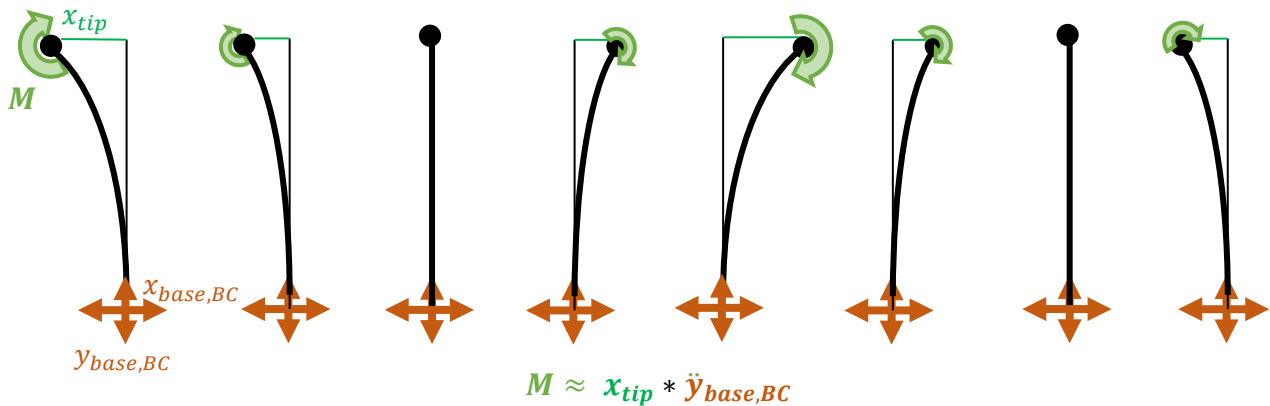


Figure 26: One cycle of component model's first bending mode (excited by x excitation) with nonlinear moment shown

Figure 26 visualizes one cycle of the component first bending mode being excited by  $\hat{x}$  excitation. While this is happening, in the case of frequency ratio 2,  $\hat{y}$  excitation is applied at frequency  $\omega_y = 2\omega_x$ . Consider the first instance in Figure 26, where the tip displacements in



$\hat{x}$  is at a maximum (in the negative x direction). If the phase of excitation in  $\hat{y}$  is such that its positive peak acceleration occurs at this instant in time (i.e. phase angle between x-excitation and y-excitation is either  $0^\circ$  or  $180^\circ$ ), this will generate an additional moment  $M$  in the beam (in the same direction as the moment due to the x-excitation) that will increase the magnitude of the tip displacement, and thus the stress at the base of the beam.

A few moments later the tip mass will reach its opposite peak  $\hat{x}$  displacement as shown in the fifth instance in Figure 26. This moment in time occurs a half x-cycle after the first instance. Meanwhile, the  $\hat{y}$  excitation will have completed an entire cycle, as  $\omega_y = 2\omega_x$ , and again reached its peak positive value. Once again, the additional bending moment due to y-excitation will increase the tip displacement and bending stresses that would have occurred from x-excitation alone. This cycle of stress amplification will repeat every steady state cycle because  $\omega_y = 2\omega_x$ .

As discussed above, the phase condition described in the previous two paragraphs is represented by phase angles  $0$  and  $180^\circ$  at frequency ratio  $2$  in Figure 25 (Simulation sets 53 and 59)

Similarly, phase angles  $90^\circ$  and  $270^\circ$  at frequency ratio  $2$  in Figure 25 represent phase conditions where the peak value of the steady stresses observed in the beam is decreased by the largest amount. This occurs when the phase angle is such that in Figure 26 – peak  $\hat{x}$  tip displacement corresponds with peak negative  $\hat{y}$  acceleration. In this case, the additional moment due to the y-excitation counteracts the bending moment from the x-excitation and thus decreases tip x-displacement and the corresponding bending stress at the base of the beam. Just as with the stress-amplification, the stress de-amplification repeats as the phase relationship cycles through  $360^\circ$ .

### 3.5.2.2 Frequency domain interpretation

Figure 27 shows the component model along with its excitation conditions. The nonlinear moment  $M$  induced by the tip mass, its displacement, and axial acceleration can be described generally as:

$$M \approx m * x_{tip} * \ddot{y}_{tip}$$

Equation 1: Nonlinear bending moment

From linear beam theory, we can create an estimate of this nonlinear moment. Derivation of the required equations of motion for a cantilever beam with a tip mass are shown in Appendix 5.7. The tip displacement  $x$  will be dominated by the  $\hat{x}$  excitation, as the  $\hat{x}$  excitation frequency was near the first bending frequency of the beam.  $\hat{x}$  excitation at the base of the component (the boundary condition in this section's simulations) takes the form:

$$x_{base} = \alpha_1 * \cos(\omega_x t + \phi_{base})$$

Equation 2: X\_base

$\alpha_1$  represents the amplitude of excitation, and  $\phi_{base}$  represents the phase of excitation.

The tip response in  $\hat{x}$  can be linearly approximated by:

$$x_{tip,linear} \approx \alpha_2 * \cos(\omega_x t + \phi_{tip,x})$$

Equation 3: X\_tip\_linear

Where  $\alpha_2$  is the magnitude of tip motion, and  $\phi_{tip,x}$  is the phase of the tip response in  $\hat{x}$ .  $\alpha_2$  and  $\phi_{tip,x}$  can be approximated from linear beam theory. This is a linear approximation of the tip displacement  $x$ , which does not include the effect of MDoF excitation.

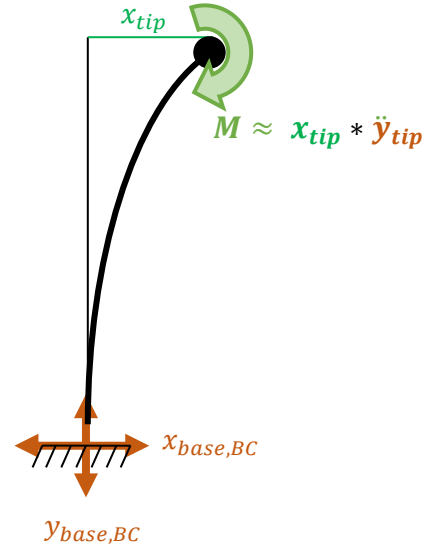


Figure 27: Component model with nonlinear moment shown

The  $\ddot{y}_{base}$  acceleration is described by:

$$\ddot{y}_{base} = \beta_0 * \cos(\omega_y t)$$

Equation 4:  $\ddot{Y}_{dd\_base}$

Where  $\beta_0$  represents the amplitude of acceleration applied to the base of the component model. Note that  $\ddot{y}_{base}$  has zero phase, as this paper measures relative phase as the phase of  $\hat{x}$  excitation when  $\hat{y}$  excitation has zero phase. The acceleration of the tip in  $\hat{y}$  will be dominated by the  $\hat{y}$  excitation frequency, and an estimate of  $\ddot{y}_{tip}$  can be estimated by a magnitude and phase shift applied to  $\ddot{y}_{base}$ .

$$\ddot{y}_{tip} \cong \beta_1 * \cos(\omega_y t + \phi_{tip,y})$$

Equation 5:  $\ddot{Y}_{dd\_tip}$  estimate

The estimate of moment  $M$  then becomes:

$$M \approx m * \alpha_2 * \cos(\omega_x t + \phi_{tip,x}) * \beta_1 * \cos(\omega_y t + \phi_{tip,y})$$

$$M \approx \gamma * \cos(\omega_x t + \phi_{tip,x}) * \cos(\omega_y t + \phi_{tip,y})$$

Equation 6: Nonlinear moment estimate

Where  $\gamma$  arises from the simple multiplication of coefficients. Through trigonometric properties, this moment can be decomposed into two frequency components:

$$M \approx \gamma * \{ \cos[(\omega_y + \omega_x)t + \phi_{tip,x} + \phi_{tip,y}] + \cos[(\omega_y - \omega_x)t - \phi_{tip,x} + \phi_{tip,y}] \}$$

Equation 7: Nonlinear moment estimate expanded

Equation 7 demonstrates that the nonlinear moment can be decomposed into two separate frequencies. The two frequency components of this moment can be approximated as excitation sources acting on a linear beam (although they originate from a nonlinear phenomenon).

The case of frequency ratio 2 causes one of the nonlinear moment frequencies in Equation 7 to equal  $(\omega_y - \omega_x) = (2\omega_x - \omega_x) = \omega_x$ . The moment at this frequency will spectrally interfere with the linear response of the component tip,  $x_{tip,linear}$  which is also at

frequency  $\omega_x$ . Depending on the phase of the  $\hat{x}$  linear tip response  $\phi_{tip,x}$  and the phase of the  $\hat{y}$  tip response  $\phi_{tip,y}$ , this interference will either increase or decrease the displacement of the tip. This explains provides ground for the stress amplification and stress de-amplification conditions observed in the simulation results for frequency ratio 2.

Equation 7 describes nonlinear moments which occur at frequencies which are not frequencies used to excite the structure. The two new frequencies described,  $(\omega_y + \omega_x)$  and  $(\omega_y - \omega_x)$ , are a result of a simple “first order” approximation. They are typically the most prominent non-excitation frequencies observed in the responses, however there are other new frequencies introduced as a result of the nonlinear moment.

The nonlinear moment in Equation 7 will result in acceleration at the new frequencies  $(\omega_y + \omega_x)$  and  $(\omega_y - \omega_x)$ , which implies  $\hat{x}$  tip displacements at the new frequencies. Since these frequencies are present in the  $\hat{x}$  tip displacement, they can then interact again with  $\ddot{y}$  to generate more nonlinear moments at another set of frequencies,  $(2\omega_y + \omega_x)$ ,  $(2\omega_y - \omega_x)$ , and  $(\omega_x)$ . Moments at these “second order” frequency estimates will thus also act on the structure. The moments at these frequencies will be less intense than the first order approximation frequencies’ moments, as they are proportional to the displacement induced by the first order moments.

The effect of these nonlinear forces is observed in the simulation data used to produce Figure 25. In particular, taking the FFT of the acceleration at the tip of the beam allows us to see the presence of these predicted nonlinear forcing frequencies in the tip response. For example, take simulation 31 (Appendix 5.3), which corresponds to the test condition with frequency ratio of 1.5 ( $\omega_y = 1.5\omega_x$ ), and a phase of  $0^\circ$ . Figure 28 shows the acceleration realized in the steady state portion of the tip acceleration in the  $\hat{x}$  direction. The spectrum (untreated for leakage) is

shown underneath it. The excitation frequency in the  $\hat{x}$  direction was 76Hz, while the first order frequency approximations are 38.4Hz and 192Hz. Peaks at both these first order approximations are visible in the acceleration spectrum (circled and labeled on plot).

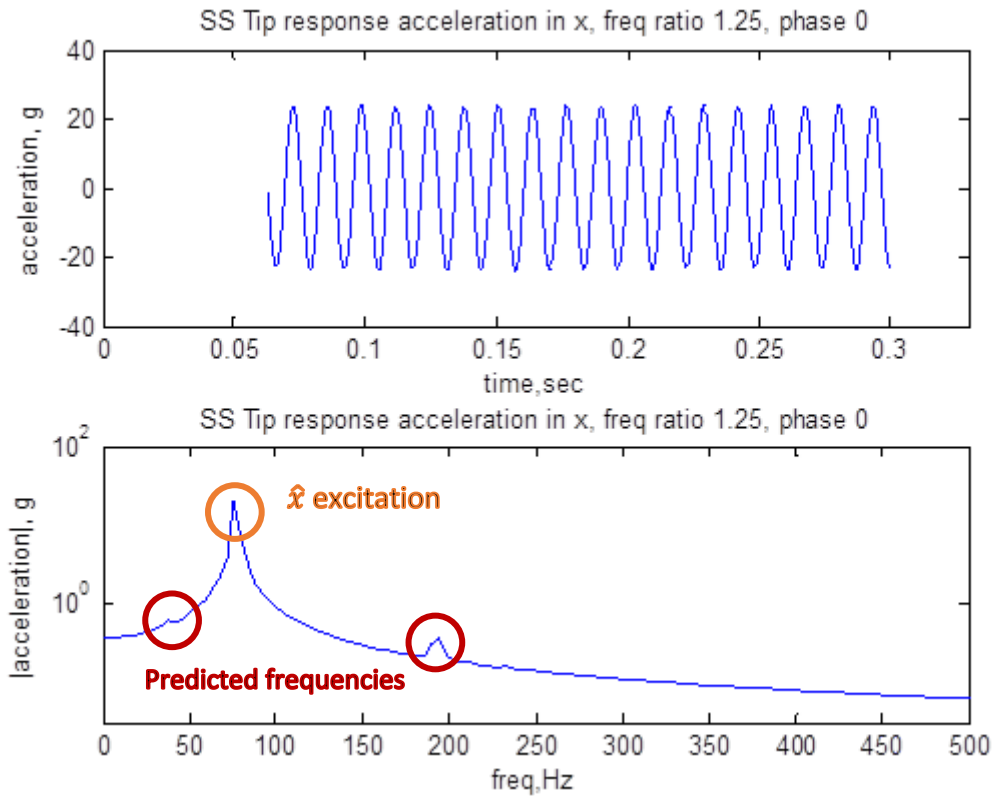


Figure 28: Steady State Tip Response ( $x$ ) for simulation 31, frequency ratio 1.25, phase  $0^\circ$

Similar results for test cases 98 (frequency ratio 2.75 and phase  $90^\circ$ ) and test case 53 (frequency ratio 2 and phase  $0^\circ$ , a simulation which resulted in one of the largest amplifications) are also shown in Figure 29 and Figure 30. The first order predicted frequencies for test case 98 are 134Hz and 288Hz; both of which are peak frequencies in Figure 29 (circled in figure). The first order predicted frequencies in case 53 are 76Hz and 230Hz. In Figure 30 we can see frequency peaks at both these predicted frequencies (76Hz has such a large peak since the linear  $\hat{x}$  excitation response is also 76Hz). Figure 30 also shows a tiny peak at 385Hz, one of the second order frequency estimates.

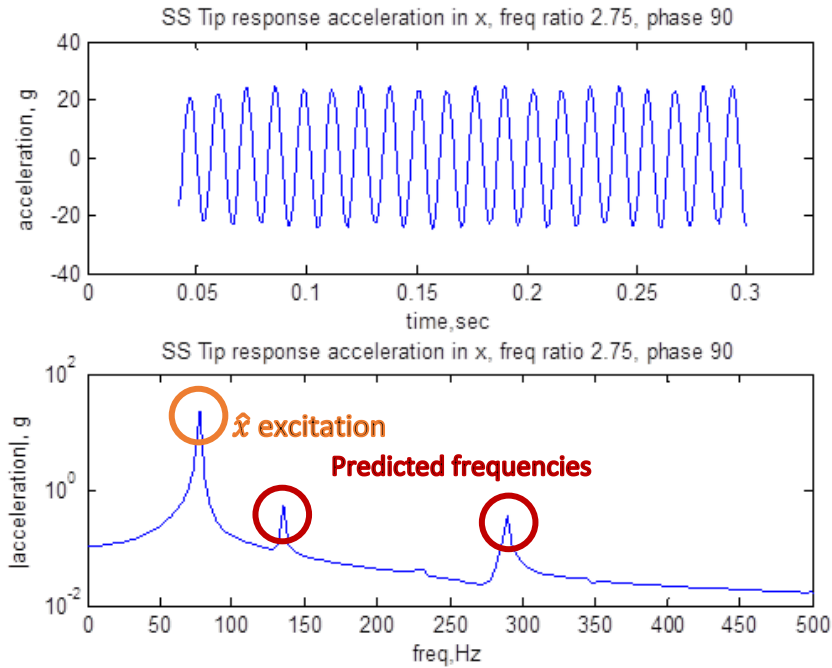


Figure 29: Steady State Tip Response (x) for simulation 98, frequency ratio 2.75, phase 90°

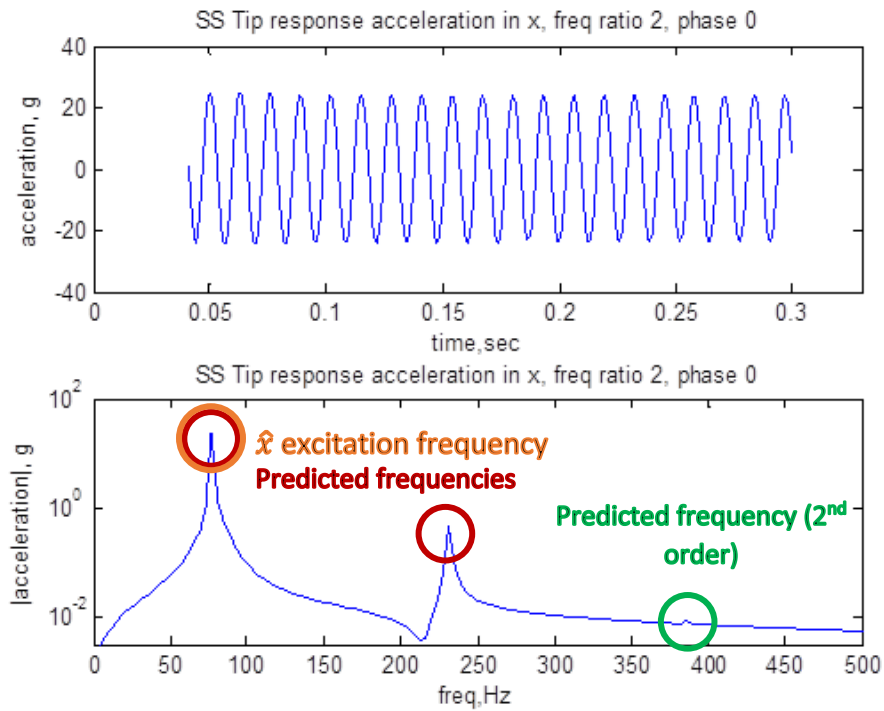


Figure 30: Steady State Tip Response (x) for simulation 53, frequency ratio 2, phase 0°

Note that the presence of these frequencies is not dependent on the frequency ratio, and they are present in simulation results even when stress amplification is small (stress amplification is large when a nonlinear moment frequency coincides with the resonant frequency of the beam). The stress amplifications of the simulation results shown in Figure 28 and Figure 30 (tests 31 and 98) were close to 1, while the stress amplification for the data shown in Figure 30 (test 53) was around 1.05. In general, the amplitude of the acceleration response at the predicted frequencies varies with both frequency ratio and phase. It should also be noted that not all frequencies present in the response are accounted for. In particular, a small peak at 230Hz is observed in most simulations regardless of frequency ratio, and is likely the result of other nonlinear forces not investigated in this study. But, the magnitude of this peak was observed to be much smaller than that of the first order frequencies peaks in every simulation.

Experimental results from Section 2 also show the presence of these predicted new frequencies in the measured tip acceleration response. Figure 31 shows the steady state response measured during the multi-axis excitation portion of experimental test condition 1. The frequency content of the signal is shown in the bottom plot of Figure 31. There is a distinct peak at the expected predicted frequency of 75Hz (the excitations are at 25 and 50Hz).

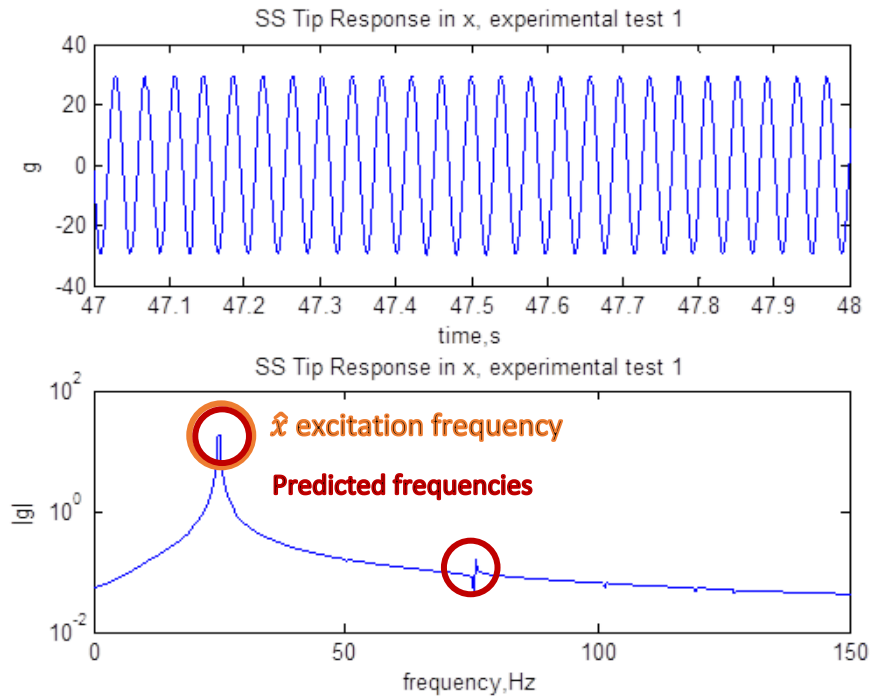


Figure 31: Steady State Tip Response ( $x$ ) for experimental test 1, frequency ratio 2

It should also be noted that the equations presented in this subsection are approximations. These approximations are useful in understanding the effect of the nonlinear moment observed in this experiment, and will be of value only if the linear response of the component is much larger in magnitude than the nonlinear portion of the response. This is because nonlinear moment  $M$  and thus the nonlinear response of the tip  $x$  is dependent on itself. If this condition is not met – which will only occur when the  $\hat{y}$  excitation is extremely large – then the approximations provided in this section will underestimate the nonlinear moment. These will result in underestimates of the stress amplification and de-amplification.

An iterative method such as Newton Raphson Iteration is required to accurately solve/simulate this geometrically nonlinear beam. N-R iteration was used by the finite element solver for all results presented in this experiment.



### 3.6 Comparison of finite element results with experimental results

Amplification factors from the finite element results presented in Section 3.5.1 can not be directly compared to the experimental results presented in Section 2.4.1, as the finite element model was not identical to the experimental model. The experimental model was chosen to amplify the nonlinearity being investigated, and to work with the available test equipment. The finite element model was chosen to resemble the size and shape of a large electronic component.

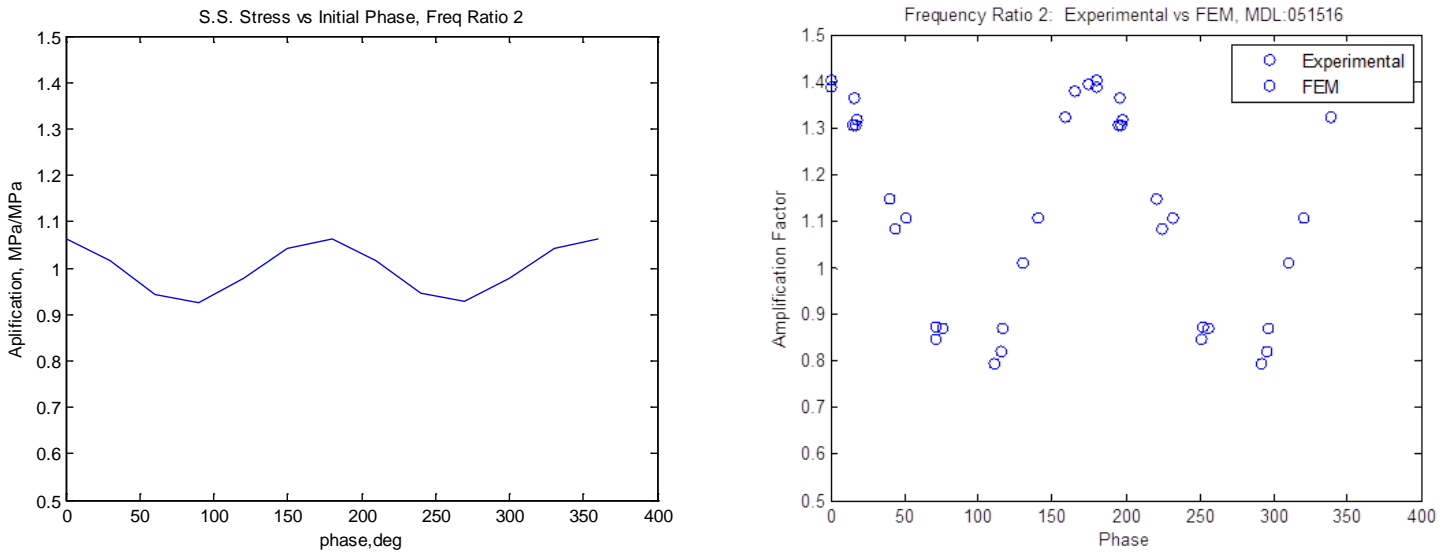


Figure 32: FEA simulation results (left) and experimental results (right)

However, based on the physics identified in Section 3.5.2, the relationships any beam-model has with phase should be similar. These two plots are shown side by side in Figure 31. In both the finite element study and the experimental tests, an identical relationship between excitation phase and amplification is observed. This is logical, because the nonlinear moment introduced at resonant frequency will either interfere constructively with (amplify) or destructively (attenuate) the response, in other words it will either work with the translational excitation or work against the translational excitation (the translational excitation is also at resonant frequency) depending on the nonlinear moment's phase.

Based on Equation 7, the nonlinear moment's phase depends on  $\phi_{tip,x}$  and  $\phi_{tip,y}$ . From beam theory, we can approximate  $\phi_{tip,x}$  to be approximately constant ( $-90^\circ$ , since  $\omega_x$  is at resonant frequency). This constant value was measured to be approximately  $-60^\circ$  in the finite element study, as the structure was being excited slightly below its resonant frequency.  $\phi_{tip,y}$  can generally be approximated as 0 for small deformation beams (since the first axial mode is sufficiently higher than excitation frequency  $\omega_y = 2\omega_x$ ,  $\omega_x$  is first bending mode frequency). While this is not generally true for large deformation beams,  $\phi_{tip,y}$  was still found to be close to zero for the deformation ranges investigated in this study. Thus, the amplification factor's relationship with phase should be similar for any beam tested, which is why we observe similar relationships between amplification factor and phase in Figure Figure 31.

In order to better validate the experimental results presented in Section 2.4, the exact specimens used in the experiments were modeled and simulated in finite element. This procedure is described in detail in the following section.

### 3.6.1 Experimental validation with finite element

The experimentally obtained results from the previous section are validated in finite element in this section.

#### 3.6.1.1 Finite Element model description

The FE model was constructed to mimic the experimental test specimen. Measurements were taken of the test specimen (and tip mass accelerometers), and were used to generate a 2-D Finite element beam model with identical properties. During the process, it was realized that the FE model needed to be extremely accurately tuned; and that the FEA model would need to be tuned (as the test

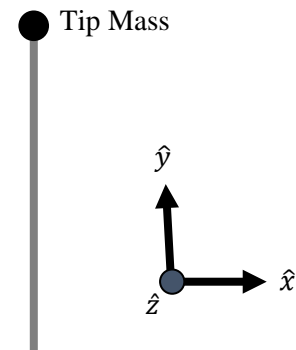


Figure 33: Finite Element model, a beam with a tip mass. Excitations applied at base of beam.

numbers progressed) to address material softening. For the same reason, every time the physical test specimen was changed due to fatigue softening, a new FE model needed to be generated and tuned.

The model required such a high level of precision because the nonlinear phenomenon being investigated is dependent on the phase response of the beam while oscillating at a lightly damped resonance. At resonance, a miniscule mismatch between the model and specimen can cause a large change in phase response; and thus would cause a discrepancy in the verification data.

The Finite Element model consisted of a beam with dimensions 10x1x120.5mm made of Aluminum, with a measured density of 3.89E-9 tonne/mm<sup>3</sup> and a measured stiffness of 41.9MPa. Stiffness of the sample was measured using a three point bend test.

10 elements were used to make up the beam model. A point mass equal to the mass of the two accelerometers at the tip of the specimen were applied to the tip of the beam model. The density of the aluminum was modified to include the mass of the cables. Additional stiffness introduced by the cables was ignored.

Excitation was applied as cyclic displacements in the  $\hat{x}$  and  $\hat{y}$  directions. Each will have the phase between the  $\hat{x}$  and  $\hat{y}$  displacements equal to the phase measured in the experimental run being validated.

### 3.6.1.2 Finite Element model calibration

As mentioned in previous sections, each FE model's phase response was required to exactly match the specimen's phase response. To ensure this, each test specimen was calibrated in a three step calibration process:

1. Excite physical beam at five frequencies around 25Hz

2. Calibration of the natural frequency
3. Calibration of damping

This was done for each test specimen.

The first step of the two step calibration procedure was to excite the specimen in  $\hat{x}$  at four calibration frequencies – 24.6, 24.8, 25, 25.2, and 25.4Hz. During the excitation, the  $\hat{x}$  excitation and tip response is measured.

The second step uses the phase lag measured in step 1 at 25Hz. This phase lag (relative to the excitation acceleration) should be around  $90^\circ$  as the beam is being excited at its resonant frequency. However, fine tuning was always required. Small adjustments were made to the length of the FEA beam model until the phase response at the tip of the FE model exactly matched the phase observed in the 25Hz excitation.

The final step in FE model calibration was tuning material damping. The amplitude of the response at 25Hz was tuned by adding material Rayleigh damping to the Aluminum. Damping was added until the steady state response of the tip (when simulated) exactly matched the steady state response measure during the specimen's 25Hz calibration excitation. Because only a single mode is being excited in this experiment, only one Rayleigh parameter  $\alpha$  was used ( $\beta = 0$ ). The formulation of Rayleigh damping applied can be found in Appendix 5.2.

The verification process was then validated by simulating the tuned model at 24.6, 24.8, 25.2, and 25.4Hz and comparing the amplitude/phase of the steady state simulation responses to the amplitude/phase measured in the corresponding experimental calibration measurements.

While the above three step process was done for each new specimen, further tuning of the FEA model was required to account for material fatigue. For each run, the FEA model was softened and phase calibrated to the experimental SDoF 25Hz data for that run. This ensured

that the FE model's phase response was exactly the same as the phase response of the experimental test specimen during the experimental run being simulated.

### 3.6.1.3 Simulation process

The calibrated FE model is first tuned to the experimental SDoF 25Hz data for the experimental run being simulated. The appropriate phase offset for the run being simulated was applied to the sinusoidal boundary displacements. Geometrically nonlinear time domain simulations were run on a the tuned until steady state tip response was observed. Amplification factors were computed using tip displacements during an MDoF simulation normalized by tip displacements measured during the SDoF-only tuning process.

### 3.6.1.4 Test matrix

The simulation matrix used for validation is taken directly from the experimental results presented in Section 2.4.2. Each phase angle observed in the experimental section is to be simulated using a calibrated and tuned FE model. The test matrix is shown in Table 6.

Test Number	$\hat{x}$ Frequency and magnitude	$\hat{y}$ Frequency and magnitude	Phase (°)
1	.3g @ 25Hz	2 g @ 50Hz	15.7
2	.3g @ 25Hz	2 g @ 50Hz	51.5
3	.3g @ 25Hz	2 g @ 50Hz	76.2012
4	.3g @ 25Hz	2 g @ 50Hz	71.7188
5	.3g @ 25Hz	2 g @ 50Hz	0
6	.3g @ 25Hz	2 g @ 50Hz	111.3574
7	.3g @ 25Hz	2 g @ 50Hz	115.8398
8	.3g @ 25Hz	2 g @ 50Hz	174.8145
9	.3g @ 25Hz	2 g @ 50Hz	165.8496
10	.3g @ 25Hz	2 g @ 50Hz	116.543
11	.3g @ 25Hz	2 g @ 50Hz	140.4932
12	.3g @ 25Hz	2 g @ 50Hz	17.9297
13	.3g @ 25Hz	2 g @ 50Hz	40.3418
14	.3g @ 25Hz	2 g @ 50Hz	44.1211

15	.3g @ 25Hz	2 g @ 50Hz	159.126
16	.3g @ 25Hz	2 g @ 50Hz	71.0156
17	.3g @ 25Hz	2 g @ 50Hz	129.9902
18	.3g @ 25Hz	2 g @ 50Hz	0
19	.3g @ 25Hz	2 g @ 50Hz	14.9854
20	.3g @ 25Hz	2 g @ 50Hz	17.2266

Table 6: Test Matrix for FEM verification

### 3.6.1.5 Finite element validation results

The same computations applied to the experimental data were applied to the Finite Element data. In general the finite element data is easier to work with as we can save resulting displacements (eliminating the need to integrate acceleration), and because there is little noise in the simulation data. Finite element simulations were also not privy to the uncontrollable moment observed in the experimental data.

The finite element amplification factors are overlaid with the experimental results and presented in in Figure 33.

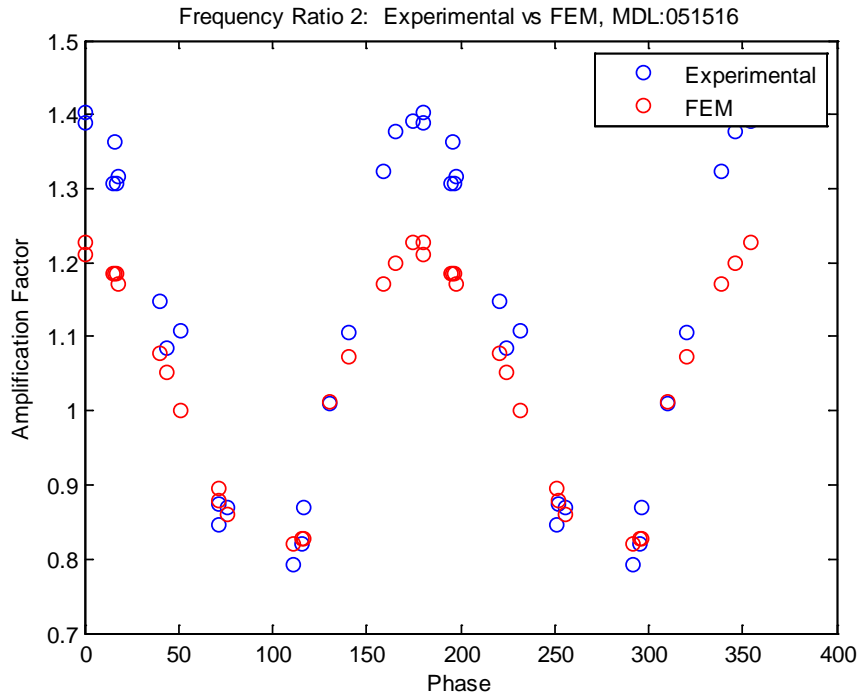


Figure 34: FEM Verification amplification factors vs. Experimental Amplification Factors

The same phase relationship can be clearly seen in both the experimental and FE simulation data. The phase relationships which are constructive are between 0 and 75, 130 and 180°; and they are destructive between 75 and 130°.

There are still differences between the finite element model and experimental results. In general the amplification seen in the experiment was greater than the amplifications predicted in finite element. There are many possible contributing factors to this, the largest of which are unmodeled nonlinearities. It is likely that the dynamic stiffness of the aluminum was lower than the measured stiffness, as the stiffness was measured statically. It is also possible that the material displayed nonlinear properties, none of which were accounted for in the FE model. This is supported by the fact that, although precise measurements were used to model each specimen, each finite element model still had to be painstakingly tuned. Because of the model calibration

process used (described in Section 2.2.4), any error in modeling the dimensions and properties of the structure will also lead to an incorrect selection of material damping. An overestimate in material damping, even an extremely small one, will lead to large underestimates in the amplitude of the MDoF tip response.



## **4 Summary, conclusions, and future work**

### **4.1 Summary and conclusions**

The results from the experiments in this study show a consistent and predictable relationship between excitation phase and stress amplification in a mass loaded beam undergoing harmonic bi-axial excitation. This amplification is a result of large tip displacement combined with axial acceleration, which induces a nonlinear moment. Because this nonlinear moment depends on the displacement response of the beam, it is inherently nonlinear in nature and can only be captured with geometrically nonlinear time domain simulations. When decoupled, this moment can be treated as a response-dependent force. When coupled with knowledge of beam dynamics, nonlinear solutions can be calculated using methods such as Newton Raphson iteration.

As predicted by initial finite element simulations, stress amplification is significant only at frequency ratio 2. This is explained by decoupling the nonlinear moment which is believed to cause the stress amplification. As illustrated by Equations 1 through 6, this nonlinear moment – caused by the addition of axial acceleration - has a component that is at the same frequency as the transverse acceleration and will constructively or destructively interfere with the response at this frequency.

### **4.2 Limitations and future work**

There are several limitations in this study, both in the experimental and finite element studies.

#### **4.2.1 Experimental limitations**

There were physical limitations in the experimental test setup which came into play. In order to avoid the use of expensive laser vibrometer measurement devices, accelerometers were

used at the tip of the test specimen. This introduced a tip mass which was modeled as a point mass in finite element. Because point masses were used to model the accelerometer masses, rotational energy of the tip mass was neglected in finite element simulations. Furthermore, the use of accelerometers meant a cable would be required to run down the axis of the beam. While the mass of the cable was accounted for by modifying the density of the beam material, any stiffness added by the cable was not accounted for. The cable was taped to the beam, and moved with the beam.

The use of accelerometers was also not optimal as the parameter of interest was displacement. Thus, all data needed to be integrated twice before analyzing. This integration was done digitally, and low and band pass filters were implemented to avoid drifting. Care was taken to ensure that the filters applied shifted the frequencies of interest (25 and 50Hz) by the same time (the phase response of the filters at 50 Hz was exactly twice the phase response at 25Hz). Since only steady state responses were analyzed, this filtering did not affect the results.

Dynamic testing limitations also were a factor in this study. Multi axial vibration control is still in its early stages. The multi axial controller used in this experiment was not capable of controlling multiple-axis multiple-frequency vibration. The vibration control was split into two independent controllers, one used in each axis. Each axis itself was a multiple-exciter, multiple-degree of freedom control problem. The  $\hat{y}$  excitation was excited by four shakers, and controlled the  $\hat{y}$  translation as well as  $\hat{x}$  rotation (controlled to zero). The  $\hat{x}$  excitation was controlled by four actuators, which controlled the  $\hat{x}$  translation as well as  $\hat{y}$  and  $\hat{z}$  rotations (both rotations controlled to zero).

While the test setup was configured to minimize motion from one axis affecting the other, each controller was only able to control at the frequency at which it was exciting. Because

of this, moment created from the mass of the fixture and structure being excited by the  $\hat{y}$  translation created a moment at the  $\hat{y}$  excitation frequency that could not be nulled by the  $\hat{x}$  actuators. This moment affected the rotation of the fixture and structure and was an uncontrollable error in the experimental setup.

Because the  $\hat{x}$  and  $\hat{y}$  excitations were controlled separately, the initial phase offset between the two was uncontrollable. Because of this, experiments were run with unknown phases, measurements taken, and the initial phase angles computed post-experiment.

#### **4.2.2 Finite Element Limitations**

Extremely precise calibration of the finite element model was absolutely critical for finite element and experimental correlation. The model calibration procedure described in Section 3.6.1.2 was conducted on each specimen to ensure that the phase response of the model matched that of the specimen. Furthermore, the calibration procedure was redone every time a difference in the SDoF response of the specimen was conducted to account for material fatigue. This calibration process was extremely time consuming and is a limitation on the number of experimental results which could be numerically validated.

#### **4.2.3 Future Work**

The purpose of this thesis is to investigate the effect of excitation parameters (frequency ratio and initial phase offset) of a mass loaded cantilever beam subjected to bi-axial sinusoidal excitation. This piece of the puzzle fits into the larger puzzle of assessing the durability of electronic components assemblies subject to multi-axial vibration. There are many more aspects to this problem which should be addressed in future research.

#### 4.2.3.1 Experiments with beams or components of different sizes

Although there have been some studies done, it is important to properly assess these nonlinear effects on component models with different sizes or masses. Intuitively, it is apparent that the more massive a component or the longer its lead, the more the component will displace when excited at its resonance. The larger the displacement of the tip of the component, the larger the nonlinear moment generated will be. These results (multi-axis simulation results exciting components of various standoff's or masses) should be validated experimentally.

#### 4.2.3.2 Examine the effects of mounting the component model on a circuit card

Although the research in this paper assesses the stresses seen in a single large electronic component, in the real world a component would be a part of a larger assembly. In particular, it would likely be attached to a circuit card. A circuit card will have its own natural frequencies and mode shapes which will affect the accelerations each component residing on it sees. A natural progression of this research project will be to examine the effect of the circuit card dynamics on the stresses seen by each component. In particular, each component will see axial accelerations and rotations about the plane of the circuit card (caused by the circuit card vibrating at its modeshapes). In the experiments presented in this paper, those accelerations were assumed to be constant frequency and rotations were assumed to be zero. While this is representative of some real world scenarios, it does not represent a generalized large electronic component residing anywhere on a circuit card with generalized boundary conditions.

As a part of this study, finite element simulations were run which simulated two identical components (modeled as beams with tip masses) mounted symmetrically on a circuit card (modeled as a beam). The circuit card was modeled as a beam with a fix-fix boundary condition, with sinusoidal excitation applied at the two ends of the beam. A beam was chosen to simulate

the first bending mode of the circuit card. A diagram of the circuit card model is shown in Figure 34 and the properties of the circuit card are shown in Section 5.8.



Figure 35: The PWB model, the green PWB board with two large electronic components mounted on it.

The dimensions of the circuit card were tuned so that the circuit card's first bending mode – with the components mounted on it – were was at twice the natural frequency of the components mounted on it. This was done to create a worst case scenario of frequency ratio of 2, identified by Ernst<sup>vii</sup>.

The first bending mode of each component is 79Hz, and the first bending mode of the circuit card was 158Hz.

Similar to the simulations run on a single component, sinusoidal excitation was applied to the model; however instead of being applied to the base of a component the excitation was applied to the ends of the circuit card beam. The in-plane  $\hat{x}$  excitation was applied at 95% the natural frequency of the component; using 95% to avoid extremely high resonant gain of a lightly damped structure. The out-of-plane  $\hat{y}$  excitation was applied at twice the  $\hat{x}$  excitation frequency.

As with study conducted on a single component, the phase between the excitation signals was of interest. A simulation matrix used in this study is shown in Table 7. Each simulation was run until steady state was reached.

Simulation Number	Phase of $\hat{x}$ excitation	Phase of $\hat{y}$ excitation
1	0	0
2	15	0
3	30	0
4	45	0
5	60	0
6	75	0
7	90	0
8	105	0
9	120	0
10	135	0
11	150	0
12	165	0
13	180	0
14	195	0
15	210	0
16	225	0
17	240	0
18	255	0
19	270	0
20	285	0
21	300	0
22	315	0
23	330	0
24	345	0
25	360	0

Table 7: Excitation Phases Simulated

Excitation levels of 5g in  $\hat{x}$  and 10g in  $\hat{y}$  were used. This acceleration was chosen because it is an acceleration value that could reasonably be experienced by electronic cards. The level of 5g value is within the peak value of the electronics screening profile recommended in the U.S. Navy's manufacturing screening program, NAVMAT P9492.

A sample of the excitation signals used is shown in Figure 35. This corresponds to Simulation 1 in Table 7. Note that both the 79Hz and the 178Hz signal start with 0 relative phase.

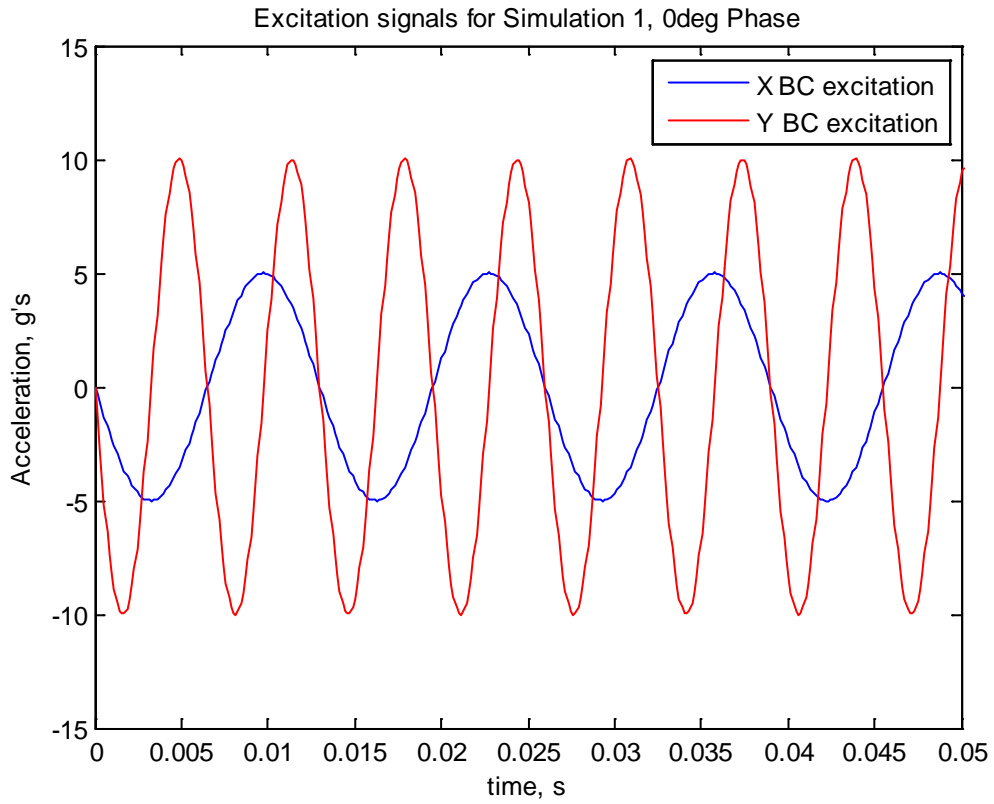


Figure 36: Excitation signals for Simulation 1

Another sample of  $\hat{x}$  and  $\hat{y}$  excitation is shown in Figure 36. This corresponds to Simulation 7 in Table 7. Note that the 79Hz signal starts at 90deg phase while the 178Hz signal start with 0deg phase.

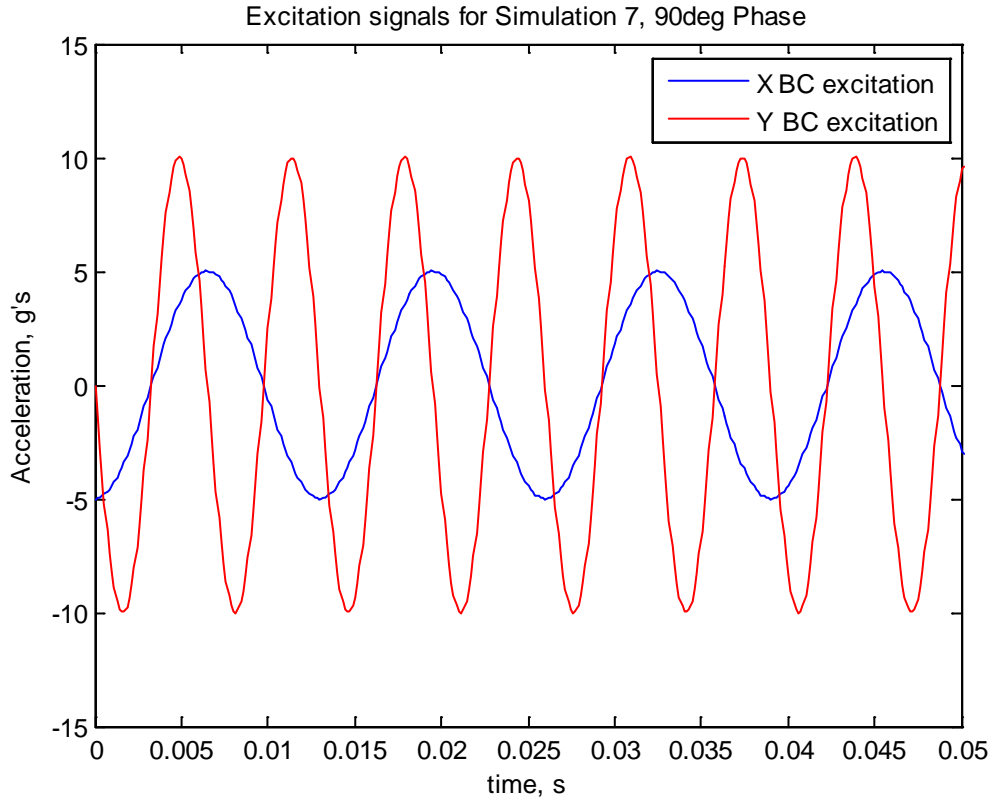


Figure 37: Excitation Boundary Condition for Simulation 7, 90deg phase

Just as with the single component simulations, these excitation conditions were applied until steady state response was observed in the component tips. The stress seen at the base of the component – the location in the structure which Ernst<sup>vii</sup> determined fails first – are of interest. A sample of the stress history at the base of the component for Simulation 1 in Table 7 is shown in Figure 37.



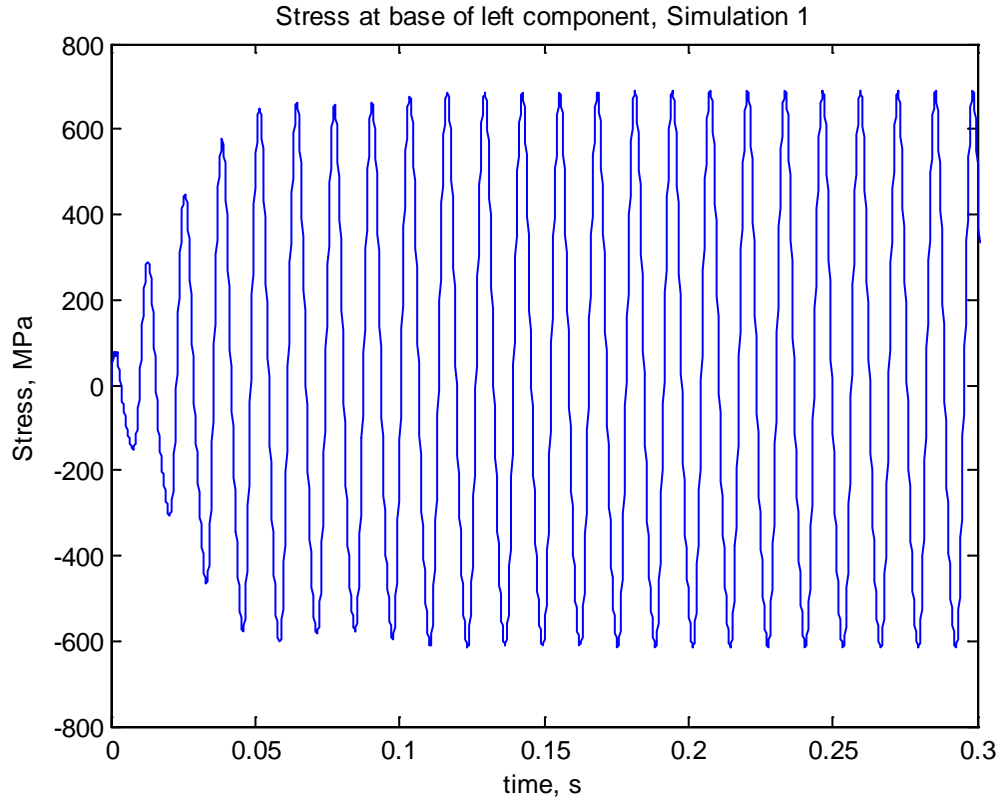


Figure 38: Stress Response of left component, Simulation 1

For this 0deg phase condition, the peak of the steady state portion of this stress response is around 688MPa. This stress is noted as the “peak” value of steady state response for the 0deg excitation condition. Similar peak-stresses were observed for all 25 phase excitations; and the peak stress vs excitation phase is plotted in Figure 38.

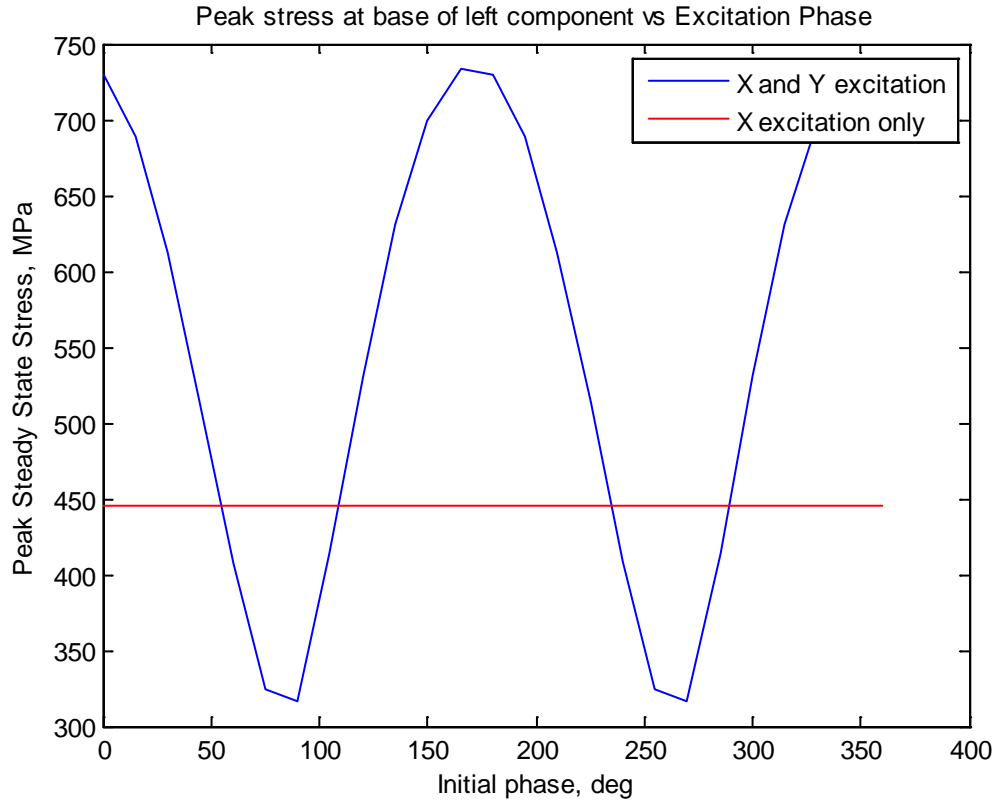


Figure 39: Peak Stress in single component and PWA Simulations

The stresses observed in single-axis ( $\hat{x}$  only) excitation is plotted in red, and can be used as a baseline for comparison. There is a clear dependence on the phase of excitation for the circuit card and component combination, similar to similar simulations involving a single component. The amplifications, however, are greater when compared to the single component simulations with the same excitations. A plot of the peak steady state stress observed in each phase excitation condition for both the single component and the component-on-PWA model is plotted in Figure 39.

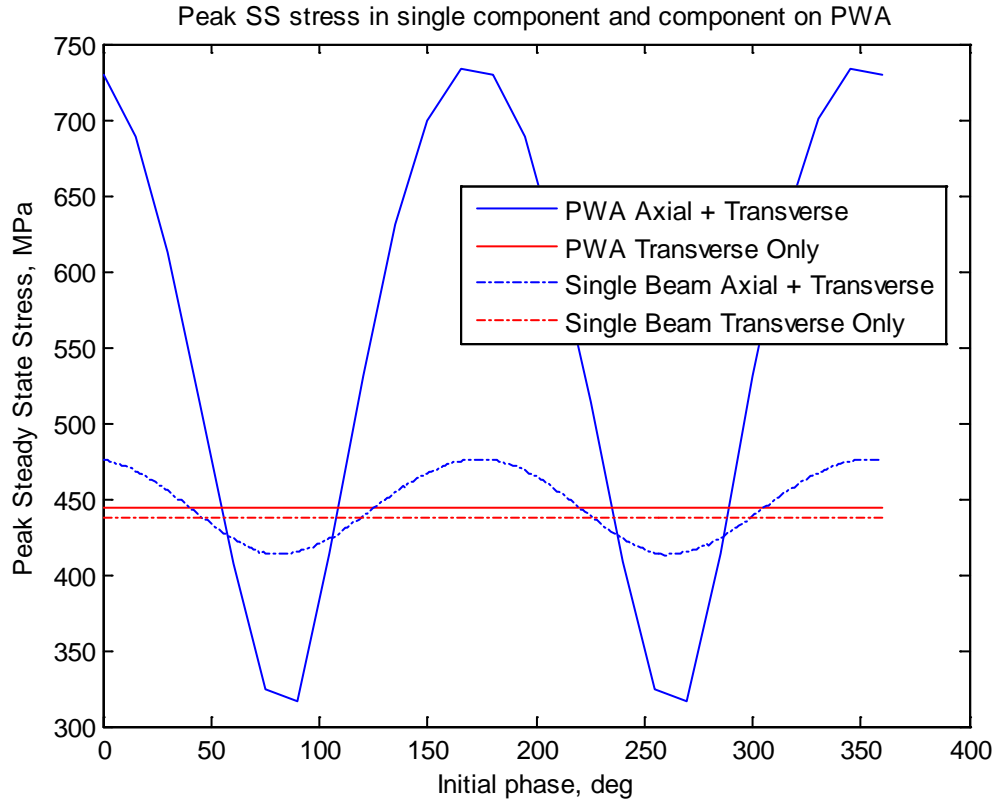


Figure 40: Peak Stress in single component and PWA Simulations

Two large discrepancies between the single component case (where excitations are applied at the base of the component) and the component-on-PWB (where excitations applied at the PWB edge) were noted. The  $\hat{y}$  excitation levels seen at the base of the component in the PWB model are higher than those applied to the single component, as the excitation applied at the edges of the PWB are amplified by the PWB dynamics. This alone will increase the effect of the nonlinear moment, which is proportional to the  $\hat{y}$  acceleration. However, there is another dynamic difference between the single component and component-on-PWB models.

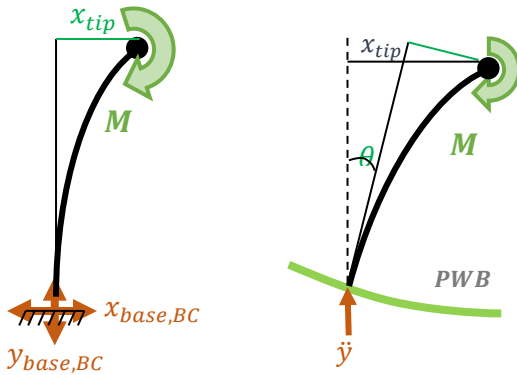


Figure 41: Single Component and Component on PWB

In the single component simulations, the slope at the base of the beam is held to be zero by the boundary excitation moment. This is not the case when the excitations are moved to the edges of the PWB. The deformation of the PWB leads to rotations induced at the base of the component. This rotation is at the  $\hat{y}$  excitation frequency. An image of this rotation during dynamic bi-axial motion is shown in Figure 40. The extra variable  $\theta$  arises from the dynamics of the PWB assembly, and will affect the moment arm  $x_{tip}$ . This rotation is believed to be the cause of the dramatic difference between the single component and PWB models, and is the next stage of research necessary to further understanding of this complex system.

Although there is still much research needed to fully understand the effects of MDoF excitation on the durability of an electronic component, many design criteria can be extrapolated from the research presented in this paper in order to design more reliable electronic component assemblies.

#### 4.2.3.3 Understand effects on fatigue life

This paper focuses on the response of a component under multi-axial vibration. Section 4.2.3.2 describes the basis for extending these component-level analyses to PWB-level analysis, however all experiments and simulations conducted and suggested relate to understanding the dynamics of the component or model.

These analyses ultimately lay the basis for understanding the fatigue life of components or PWBs under multi-axial excitation conditions, and how they differ from a PWB under single-axis excitation condition. Applying material fatigue models (S-N curves) to predict a component lifespan – as well as to predict accelerated lifecycle tests – is a natural progression of this research area.

#### 4.2.3.4 Application to Random Vibration

This paper focuses solely on sinusoidal excitation. This allows for numerous simplifications, the biggest being the assumption of a uni-modal response from the component. This is a simplification used in order to better understand the fundamentals of the problem, however this test condition does not typically exist in the real world.

Another natural progression of this research is to extend the results to simultaneous bi-axial random vibration. A random excitation greatly complicates the scenario, as a unimodal response can no longer be assumed. Furthermore, there will be nonlinear forces generated at many frequencies (rather than at specific frequencies). The combination of these two factors greatly complicate the analysis used in this paper, which was simplified because responses were measured at discrete frequencies.

In spite of these complications, the “worst case” frequency ratio/phase relationships investigated in this paper will still be the worst case under random excitation; and should be used to simplify the analysis required to understand a component/PWB under multi-axis random excitation.

## 5 Appendix

### 5.1 Aluminum 6061-T6 Properties

Mass Density	$2.7 * 10^{-9} \text{ tonne/mm}^3$
Elasticity	68900MPa
Poisson's Ratio	.33
Damping	Rayleigh, $\alpha = 100, \beta = 0$

### 5.2 Rayleigh Damping Relationship

Rayleigh material damping was used in the simulations performed in this experiment. Rayleigh damping has the following properties and constants:

$\alpha$ : Mass Proportional Damping

$\beta$ : Stiffness Proportional Damping

The damping matrix is defined by:

$$[C] = \alpha[M] + \beta[K]$$

Where  $[M]$  and  $[K]$  are the mass and stiffness matrix of the structure.

The modal damping ratio is given by:

$$\xi_i = \frac{\alpha}{2\omega_i} + \frac{\beta\omega_i}{2}$$

Where  $i$  refers to the  $i$ th mode of vibration

### 5.3 Complete Simulation Matrix for Finite Element Study

Test Number	Transverse $\hat{x}$ excitation frequency	Axial $\hat{y}$ excitation frequency	Transverse excitation phase	Axial excitation phase
1	76.9Hz	76.9Hz	0°	0°
2	76.9Hz	76.9Hz	30°	0°
3	76.9Hz	76.9Hz	60°	0°
4	76.9Hz	76.9Hz	90°	0°
5	76.9Hz	76.9Hz	120°	0°
6	76.9Hz	76.9Hz	150°	0°
7	76.9Hz	76.9Hz	180°	0°
8	76.9Hz	76.9Hz	210°	0°
9	76.9Hz	76.9Hz	240°	0°
10	76.9Hz	76.9Hz	270°	0°
11	76.9Hz	76.9Hz	300°	0°
12	76.9Hz	76.9Hz	330°	0°
13	76.9Hz	76.9Hz	360°	0°
14	76.9Hz	96.125Hz	0°	0°
15	76.9Hz	96.125Hz	30°	0°

16	76.9Hz	96.125Hz	60°	0°
17	76.9Hz	96.125Hz	90°	0°
18	76.9Hz	96.125Hz	120°	0°
19	76.9Hz	96.125Hz	150°	0°
20	76.9Hz	96.125Hz	180°	0°
21	76.9Hz	96.125Hz	210°	0°
22	76.9Hz	96.125Hz	240°	0°
23	76.9Hz	96.125Hz	270°	0°
24	76.9Hz	96.125Hz	300°	0°
25	76.9Hz	96.125Hz	330°	0°
26	76.9Hz	96.125Hz	360°	0°
27	76.9Hz	115.35Hz	0°	0°
28	76.9Hz	115.35Hz	30°	0°
29	76.9Hz	115.35Hz	60°	0°
30	76.9Hz	115.35Hz	90°	0°
31	76.9Hz	115.35Hz	120°	0°
32	76.9Hz	115.35Hz	150°	0°
33	76.9Hz	115.35Hz	180°	0°
34	76.9Hz	115.35Hz	210°	0°
35	76.9Hz	115.35Hz	240°	0°
36	76.9Hz	115.35Hz	270°	0°
37	76.9Hz	115.35Hz	300°	0°
38	76.9Hz	115.35Hz	330°	0°
39	76.9Hz	115.35Hz	360°	0°
40	76.9Hz	135.58Hz	0°	0°
41	76.9Hz	135.58Hz	30°	0°
42	76.9Hz	135.58Hz	60°	0°
43	76.9Hz	135.58Hz	90°	0°
44	76.9Hz	135.58Hz	120°	0°
45	76.9Hz	135.58Hz	150°	0°
46	76.9Hz	135.58Hz	180°	0°
47	76.9Hz	135.58Hz	210°	0°
48	76.9Hz	135.58Hz	240°	0°
49	76.9Hz	135.58Hz	270°	0°
50	76.9Hz	135.58Hz	300°	0°
51	76.9Hz	135.58Hz	330°	0°
52	76.9Hz	135.58Hz	360°	0°
53	76.9Hz	153.8Hz	0°	0°
54	76.9Hz	153.8Hz	30°	0°
55	76.9Hz	153.8Hz	60°	0°
56	76.9Hz	153.8Hz	90°	0°
57	76.9Hz	153.8Hz	120°	0°
58	76.9Hz	153.8Hz	150°	0°
59	76.9Hz	153.8Hz	180°	0°
60	76.9Hz	153.8Hz	210°	0°
61	76.9Hz	153.8Hz	240°	0°

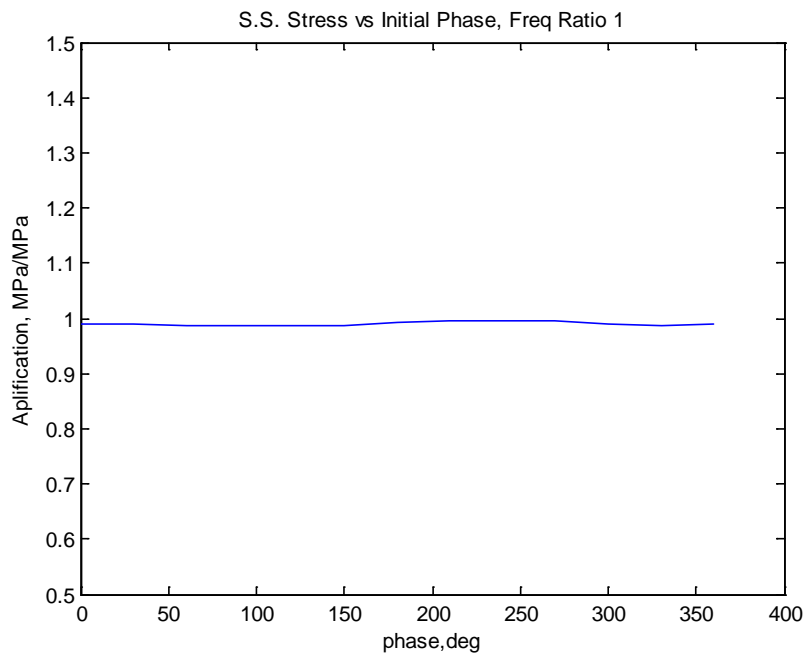
62	76.9Hz	153.8Hz	270°	0°
63	76.9Hz	153.8Hz	300°	0°
64	76.9Hz	153.8Hz	330°	0°
65	76.9Hz	153.8Hz	360°	0°
66	76.9Hz	173.0Hz	0°	0°
67	76.9Hz	173.0Hz	30°	0°
68	76.9Hz	173.0Hz	60°	0°
69	76.9Hz	173.0Hz	90°	0°
70	76.9Hz	173.0Hz	120°	0°
71	76.9Hz	173.0Hz	150°	0°
72	76.9Hz	173.0Hz	180°	0°
73	76.9Hz	173.0Hz	210°	0°
74	76.9Hz	173.0Hz	240°	0°
75	76.9Hz	173.0Hz	270°	0°
76	76.9Hz	173.0Hz	300°	0°
77	76.9Hz	173.0Hz	330°	0°
78	76.9Hz	173.0Hz	360°	0°
79	76.9Hz	192.25Hz	0°	0°
80	76.9Hz	192.25Hz	30°	0°
81	76.9Hz	192.25Hz	60°	0°
82	76.9Hz	192.25Hz	90°	0°
83	76.9Hz	192.25Hz	120°	0°
84	76.9Hz	192.25Hz	150°	0°
85	76.9Hz	192.25Hz	180°	0°
90	76.9Hz	192.25Hz	210°	0°
91	76.9Hz	192.25Hz	240°	0°
92	76.9Hz	192.25Hz	270°	0°
93	76.9Hz	192.25Hz	300°	0°
94	76.9Hz	192.25Hz	330°	0°
95	76.9Hz	211.47Hz	0°	0°
96	76.9Hz	211.47Hz	30°	0°
97	76.9Hz	211.47Hz	60°	0°
98	76.9Hz	211.47Hz	90°	0°
99	76.9Hz	211.47Hz	120°	0°
100	76.9Hz	211.47Hz	150°	0°
101	76.9Hz	211.47Hz	180°	0°
102	76.9Hz	211.47Hz	210°	0°
103	76.9Hz	211.47Hz	240°	0°
104	76.9Hz	211.47Hz	270°	0°
105	76.9Hz	211.47Hz	300°	0°
106	76.9Hz	211.47Hz	330°	0°
107	76.9Hz	211.47Hz	360°	0°
109	76.9Hz	230.7Hz	0°	0°
110	76.9Hz	230.7Hz	30°	0°
111	76.9Hz	230.7Hz	60°	0°
112	76.9Hz	230.7Hz	90°	0°

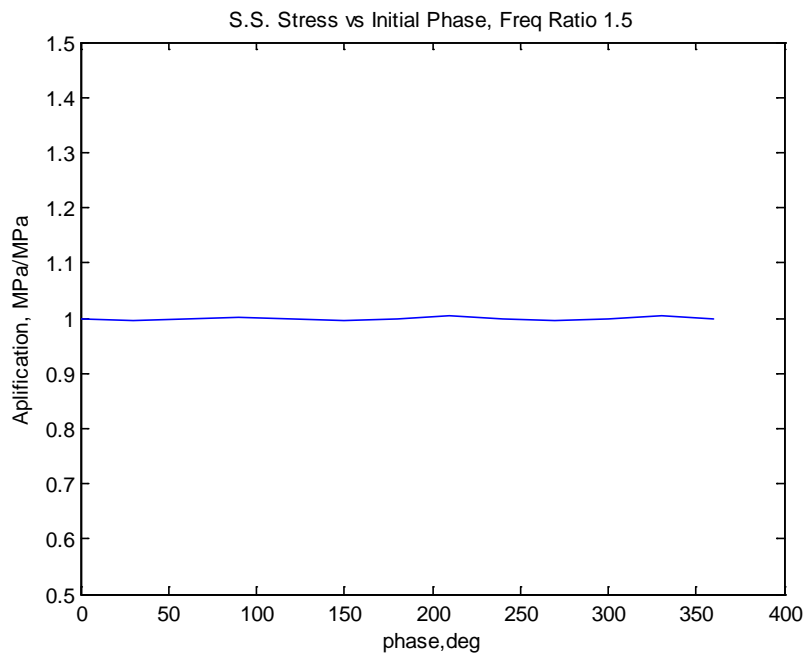
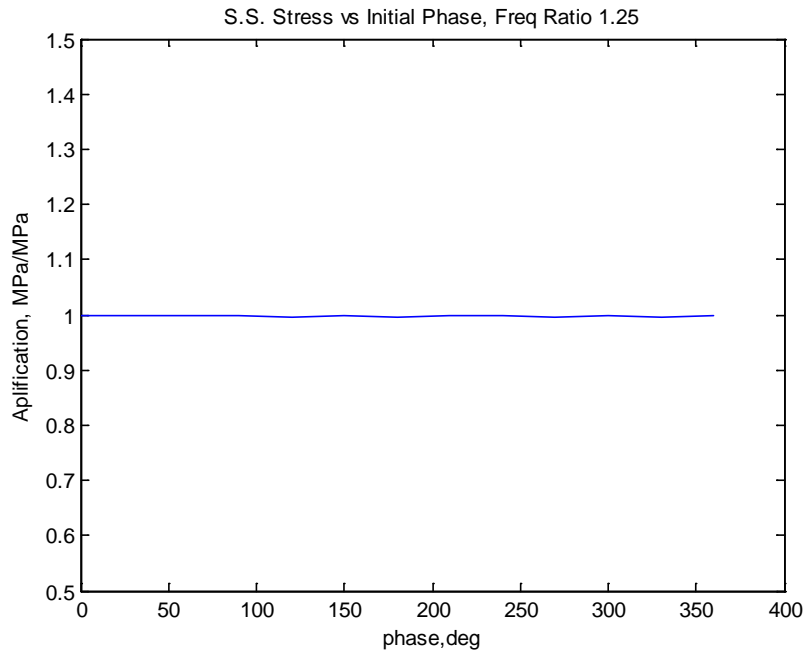


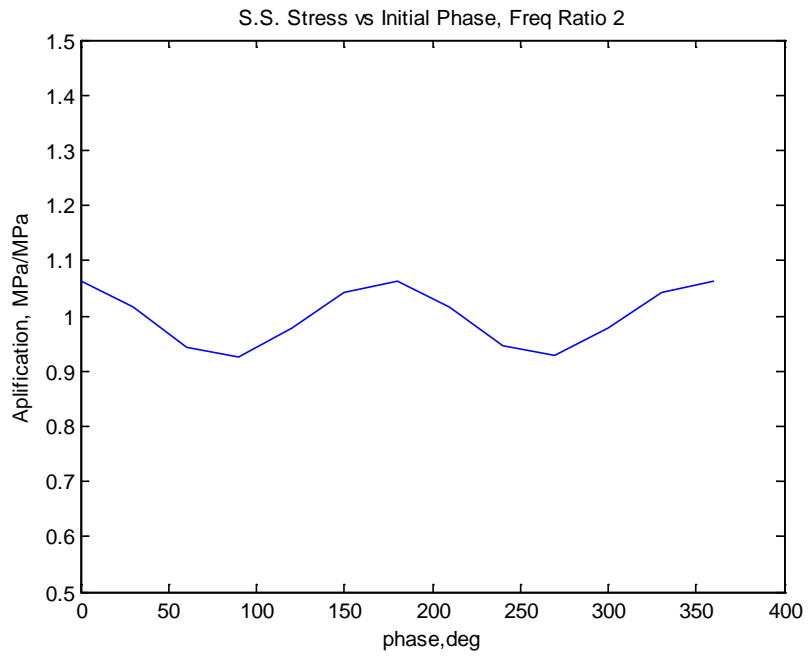
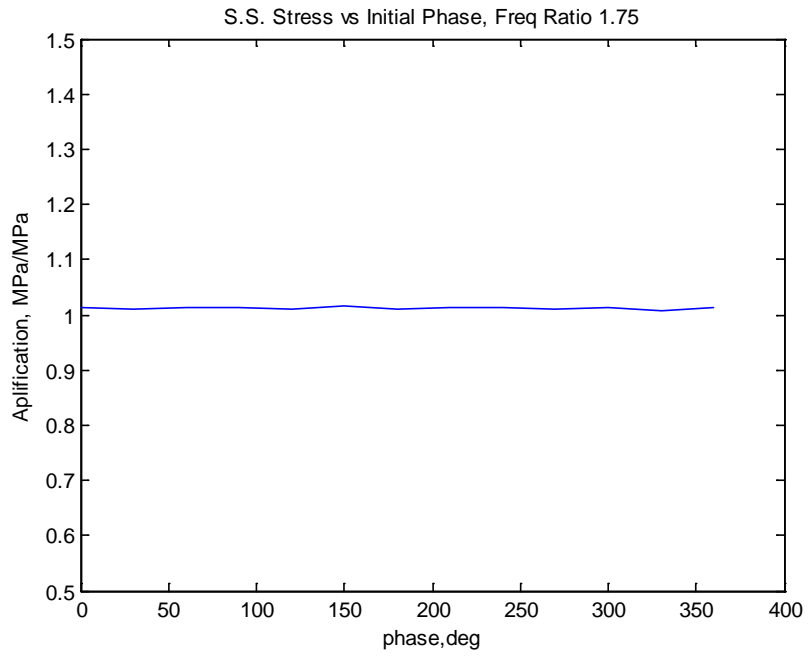
113	76.9Hz	230.7Hz	120°	0°
114	76.9Hz	230.7Hz	150°	0°
115	76.9Hz	230.7Hz	180°	0°
116	76.9Hz	230.7Hz	210°	0°
117	76.9Hz	230.7Hz	240°	0°
118	76.9Hz	230.7Hz	270°	0°
119	76.9Hz	230.7Hz	300°	0°
120	76.9Hz	230.7Hz	330°	0°
121	76.9Hz	230.7Hz	360°	0°

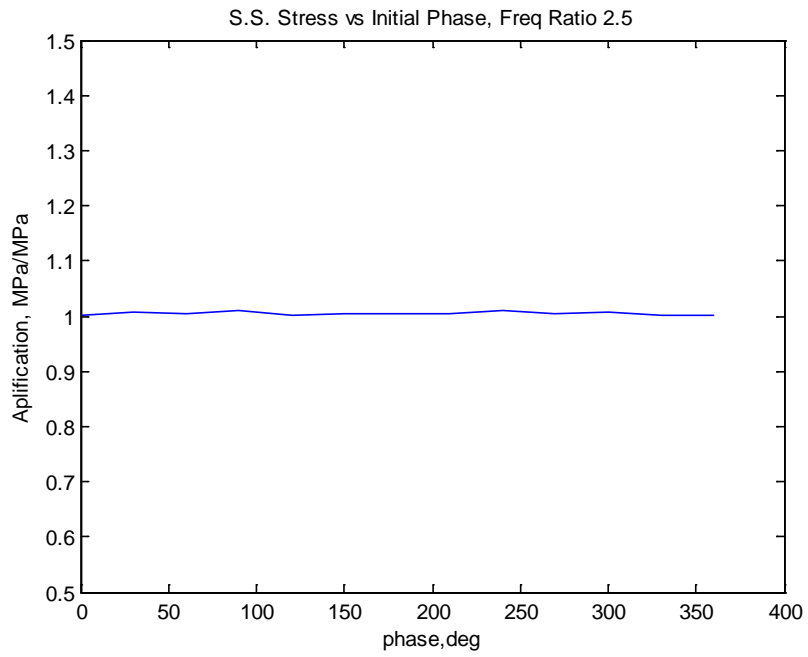
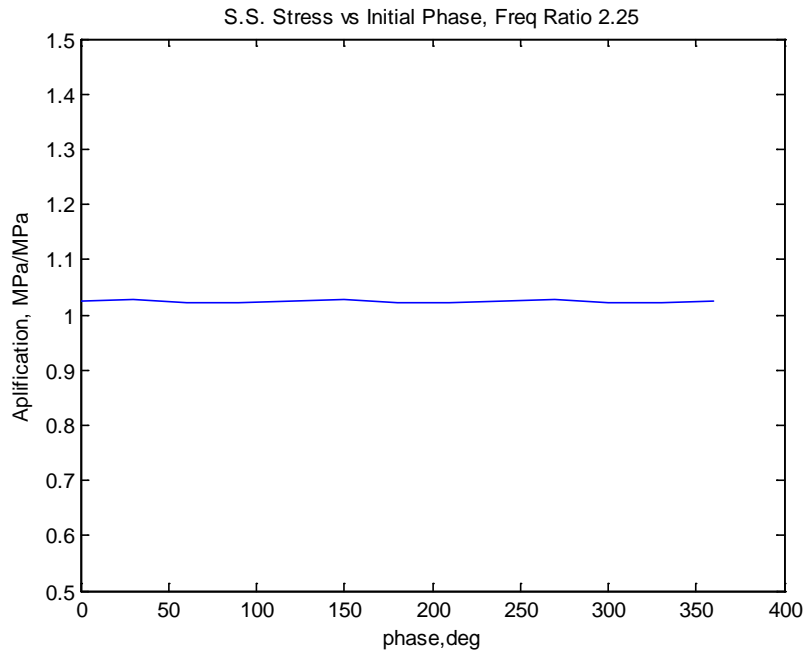
#### 5.4 Results for each Phase Sweep (Frequency Ratio Constant) in Finite Element Study

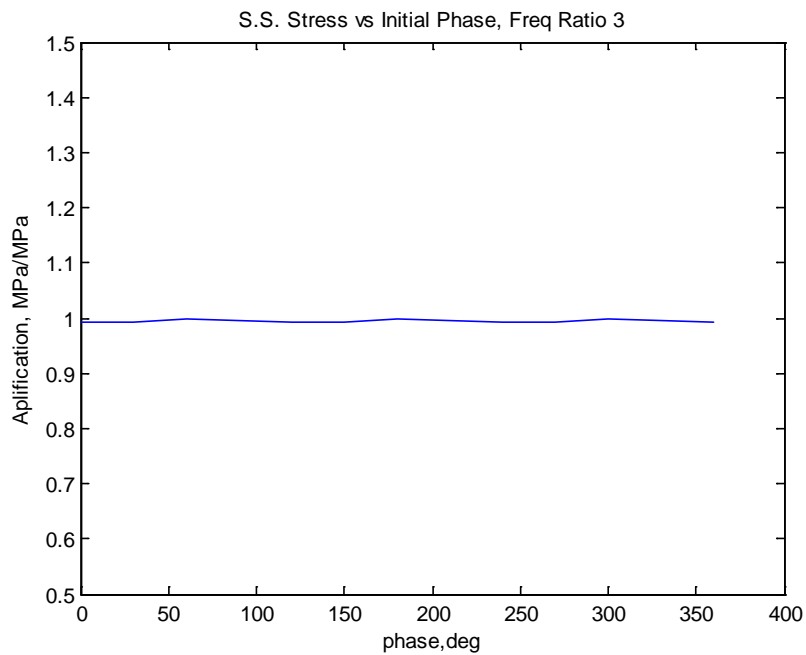
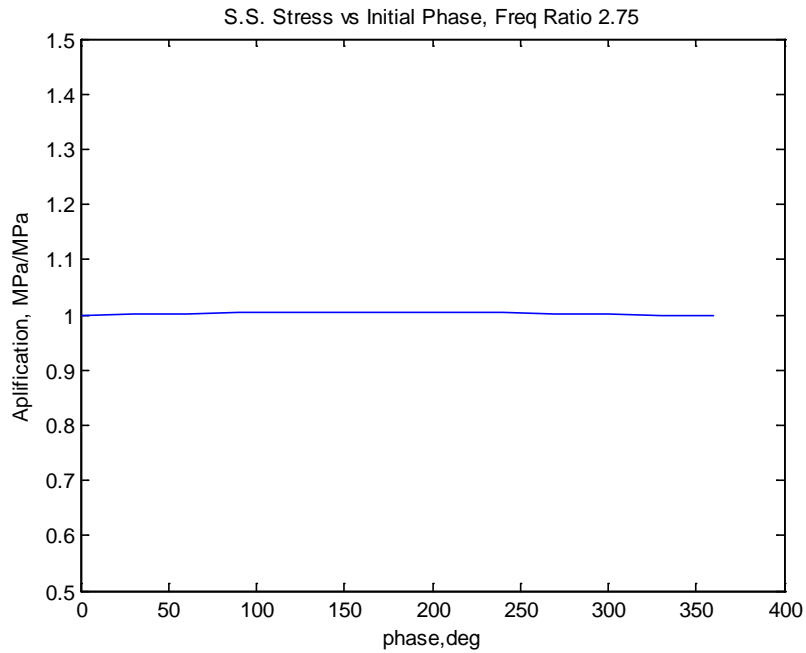
Note: The following plots are shown in a waterfall format in Figure 25: Steady state stress amplification (MDoF/SDoF) observed in all simulations (frequency ratios 1-3, excitation phases 0-360)











## 5.5 Phase Extraction from Time Data (MATLAB Code)

Time data was taken from the shaker table during 2 axis excitation. This time data was used to calculate the initial phase offset between the two excitation signals (the relative

excitation phase was uncontrollable as vibration controllers were operated separately. In each axis.

The phase was extracted in the frequency domain. The overall process involved iterating (sample by sample) through the two time signals. Starting at the current time sample of the  $\hat{y}$  axis data, 2048 samples of data are taken. The FFT of these 2048 samples was taken. The phase of the 50Hz bin was measured. If the measured phase was equal to  $-90^\circ$  (with a  $2^\circ$  error,  $90^\circ$  since phase is defined as phase of a sine wave in this paper which is  $-90^\circ$  from MATLAB's `angle()` command), it was determined that the y acceleration was at 0 phase. The phase of the 25Hz bin of the  $\hat{x}$  axis excitation was then determined to be the phase offset of this test.

Because 2048Hz was used as the sample frequency, using 2048 points for the FFT generated a spectrum which had no leakage for measurements of both 25 and 50Hz. No window function is necessary, and results produced are extremely accurate.

#### Pseudo code:

```
% iterating through the steady state portion of the response
n1_samples=2048;
for ii=1:length(t)-n1_samples-1

    % x axis excitation, FFT of 2048 samples of X axis excitation
    Y1 = single_side_fft(fs,x1(ii:ii+n1_samples));
    % y axis excitation, FFT of 2048 samples of Y axis excitation
    Y2 = single_side_fft(fs,x2(ii:ii+n1_samples));

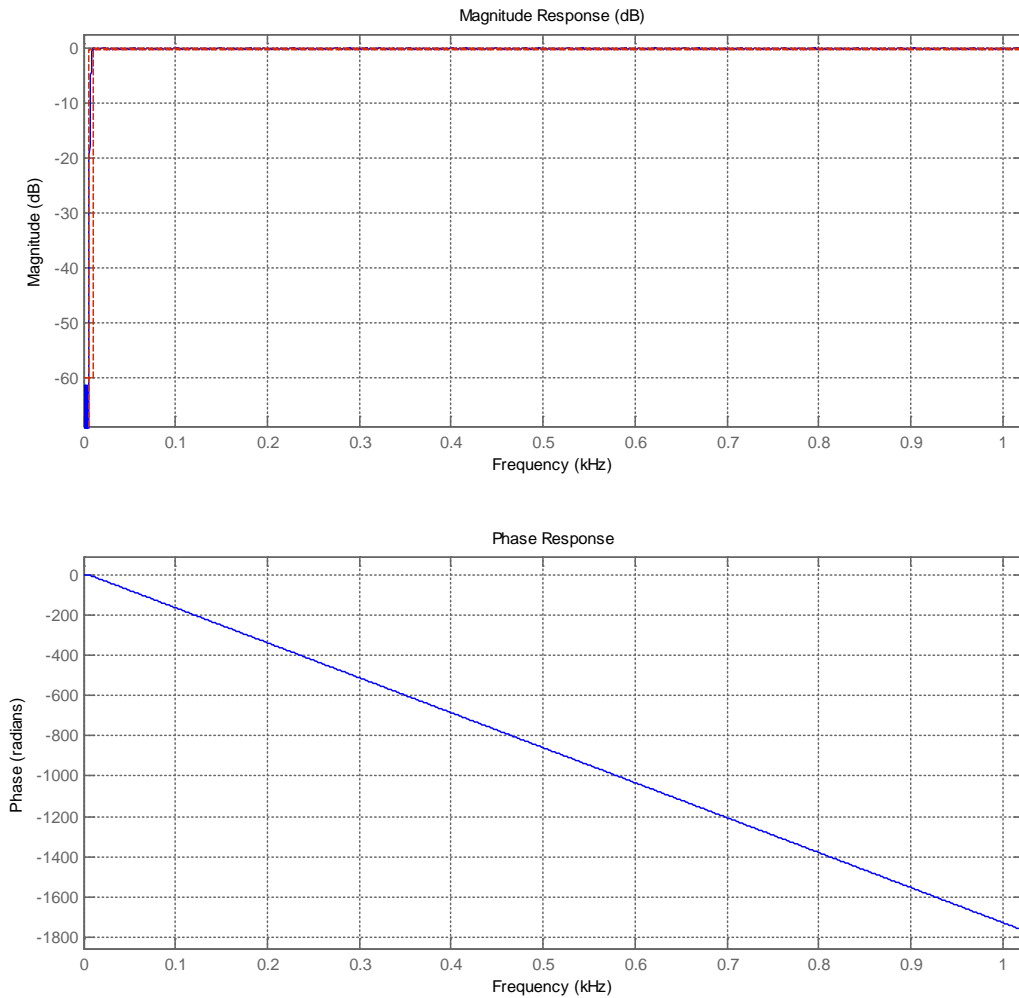
    % since using 800Hz/Lines we can use frequency as the index
    % if phase goes from positive and large (+pi) to negative and large
    % (-pi) then we know we are at a "zero phase" point for that frequency.
    % we need to apply that to the higher frequency
    ph_2 = angle(Y2(f2+1,2)); %ph_2 phase of the Y excitation at the current
timeframe
    ph_1 = angle(Y1(f1+1,2)); %ph_1 phase of the X excitation at the current
timeframe

    % if the sine-based phase of the Y frequency (phi in sin(w2+phi))
    % is zero then we are at a critical point that we want to note down
    % the phase of the X signal
    if abs(ph_2+pi/2)<2*pi/180 %2 °ree error
        % we have a critical location, note the phase of the two signals.
```

```
    phase_constants = [phase_constants;ph_2,ph_1];  
end  
end
```

Note: `single_side_fft()` generates a single side scaled FFT of the input.

## 5.6 Highpass Filter applied to data before integration



## 5.7 Periodicity of two sine waves at different frequencies, and how phase relationship between two waves can be described as a single phase angle

In this paper a single phase angle is used to represent the phase relationship (or “initial phase” offset) between two sinusoids at different excitation frequencies  $f_1$  and  $f_2$ . This is an acceptable way to characterize the relationship between two sinusoids at different frequencies IF the two frequencies have a least common multiple.

If the LCM of  $f_1$  and  $f_2$  exists, then a signal composed of a component at  $f_1$  and a component at  $f_2$  will be periodic with period  $P = LCM(\frac{1}{f_1}, \frac{1}{f_2})$ . This can be extended to say that two individual signals at frequencies  $f_1$  and  $f_2$  are periodic as a group, with  $LCM(\frac{1}{f_1}, \frac{1}{f_2})$

It is strange to work with the LCM function using fractions. Care must be taken to *not* estimate the decimal approximation, and to leave numbers in fractional form. The solution P can be found by identifying two integers M and N that satisfy:

$$P = M * \frac{1}{f_1} = N * \frac{1}{f_2}$$

Equation 8: Period of two sine waves at frequency f1 and f2

P need not be an integer.

### Examples, and relation to Phase

Start with frequency ratio 2, initial phase 0. See plot below:



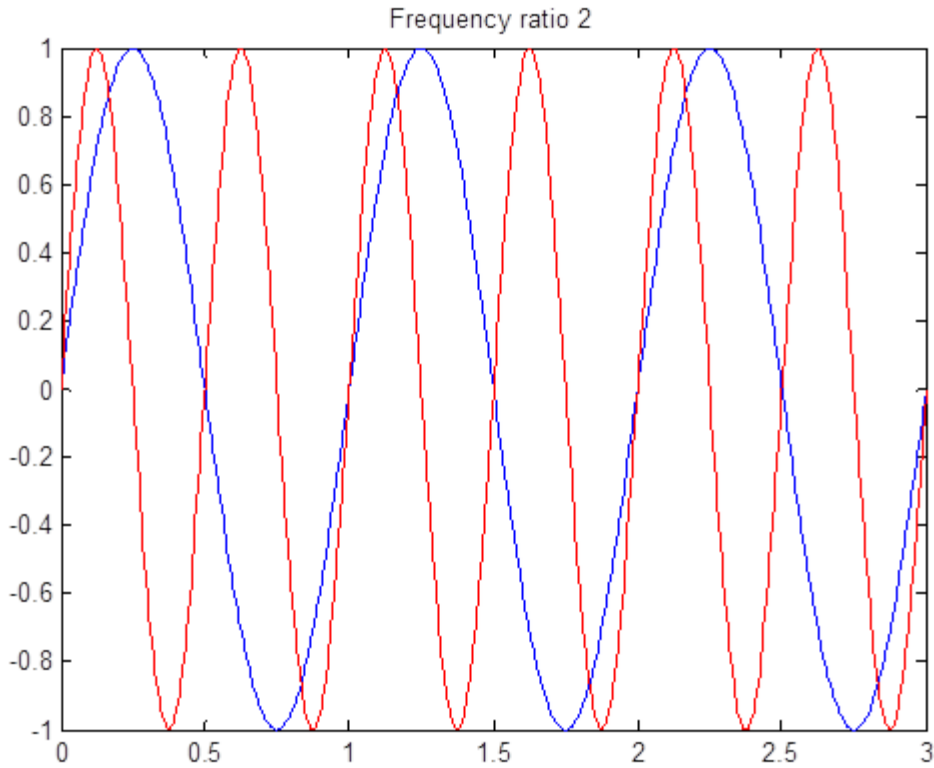


Figure 42: Sine waves with a frequency ratio of 2 ( $f_1=1, f_2=2$ )

The set of sinusoids will be periodic over:

$$P = 1 = 1 * \frac{1}{1} = 2 * \frac{1}{2}$$

Equation 9: Period of sine waves shown in Figure 41: Sine waves with a frequency ratio of 2 ( $f_1=1, f_2=2$ )

If we look at any 1 second snip of the two sinusoids (which is as good as looking at the entirety of both signals, since they are both periodic over 1sec), we notice 2 intersections (this is also N in the equation for period). The phase angles at the intersections are the same every 1sec, but we need a convenient way to express those phase angles.

In this thesis, I adopted the following way to identify the phase offsets between two signals at  $f_1$  and  $f_2$  ( $f_2 > f_1$ ):

**Take the phase of the  $f_1$  signal at the instant  $f_2$  has zero phase.**

Over one period P in the frequency ratio 2 example (Figure 41: Sine waves with a frequency ratio of 2 ( $f_1=1, f_2=2$ ))**Error! Reference source not found.**, we get two instances of 0 phase in  $f_2$ . The phase of  $f_1$  (the blue signal) when  $f_2$  has 0 phase is 0 for the first intersection, and  $180^\circ$  at the second intersection.

Note that it doesn't matter whether the phase relationship is characterized as  $0^\circ$  or  $180^\circ$ . One implies the other.

Also note that phase angles can be measured exactly using FFTs (if measurement is leakage free). This avoids the error of estimating phase by looking at time histories. This technique was used extensively in this paper.

More complex example frequency ratio 1.25

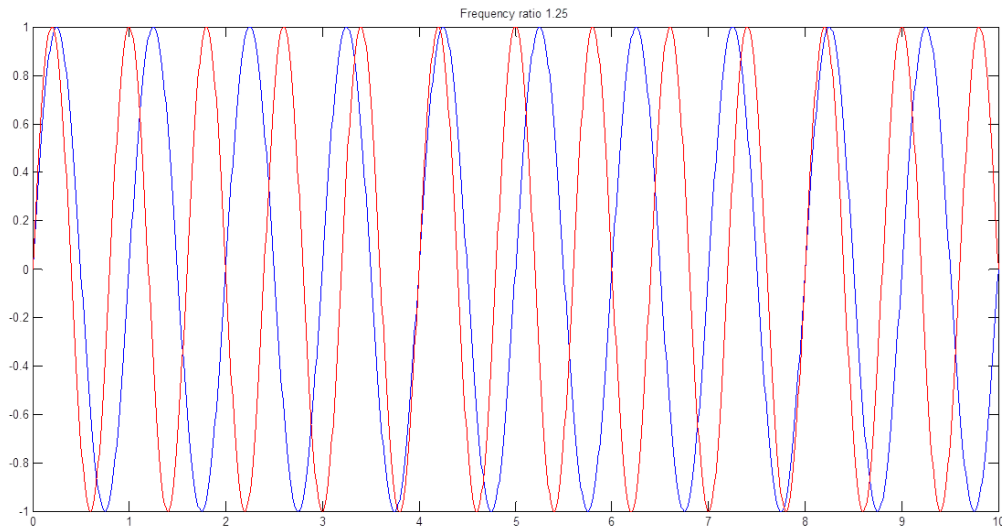


Figure 43: Frequency Ratio 1.25,  $f_1=1$ ,  $f_2=1.25$

Period of these two signals (Figure 42):

$$P = 4 = 4 * \frac{1}{1} = 5 * \frac{1}{1.25}$$

Equation 10: Period of sine waves shown in Figure 42: Frequency Ratio 1.25,  $f_1=1$ ,  $f_2=1.25$ .

The two signals both do appear to be periodic on 4.  $N$  from the above equation is 5, so we know there will be 5 0-phase points in the red  $f_2$  plot along 1 period. The red plot has 5 full cycles and this will have 5 points of 0 phase. The phase of the blue signal at these 5 0-phase points describes the “phase relationship” between the two signals. As previously noted, knowing the phase of  $f_1$  at only one of these five points still fully describes the relationship.

Take Frequency Ratio 2.75:

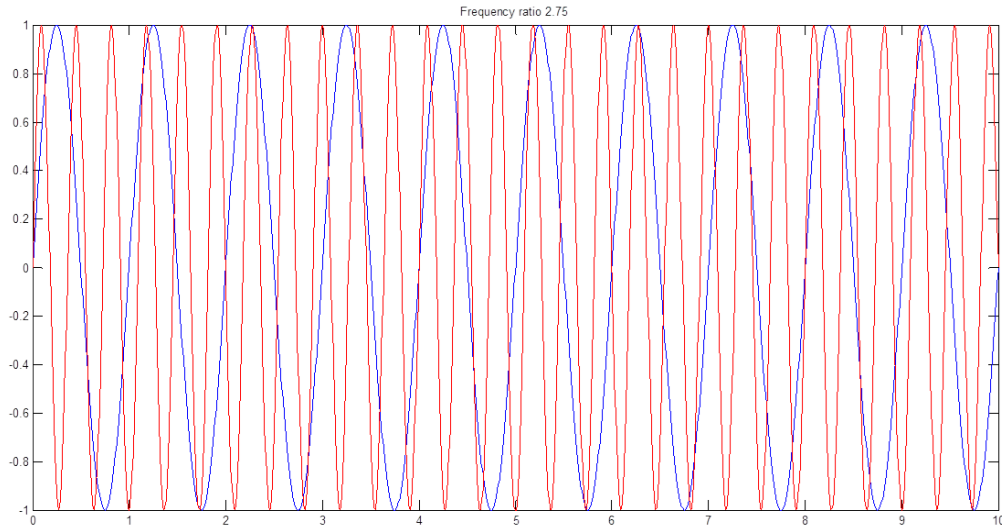


Figure 44: Frequency Ratio 2.75,  $f_1=1$ ,  $f_2=2.75$

Period of these two signals (Figure 43):

$$P = 4 = 4 * \frac{1}{1} = 11 * \frac{1}{2.75}$$

Equation 11: Period of sine waves shown in Figure 43: Frequency Ratio 2.75,  $f_1=1$ ,  $f_2=2.75$ .

The two signals both do appear to be periodic on 4.  $N$  from the above equation is 11. The red wave has 11 full cycles and this will have 11 points of 0 phase. Knowing the phase of  $f_1$  at only one of these 11 points still fully describes the relationship.

In summary, the method used in this paper to characterize the phase relationship between two sinusoids at different frequencies took advantage of the fact that the excitation frequencies used had an LCM. This allowed characterization of the phase between both sinusoids by one phase angle.

If the frequencies of excitation do NOT have an LCM:

Take the example where the frequency ratio is  $e \cong 2.71 \dots$

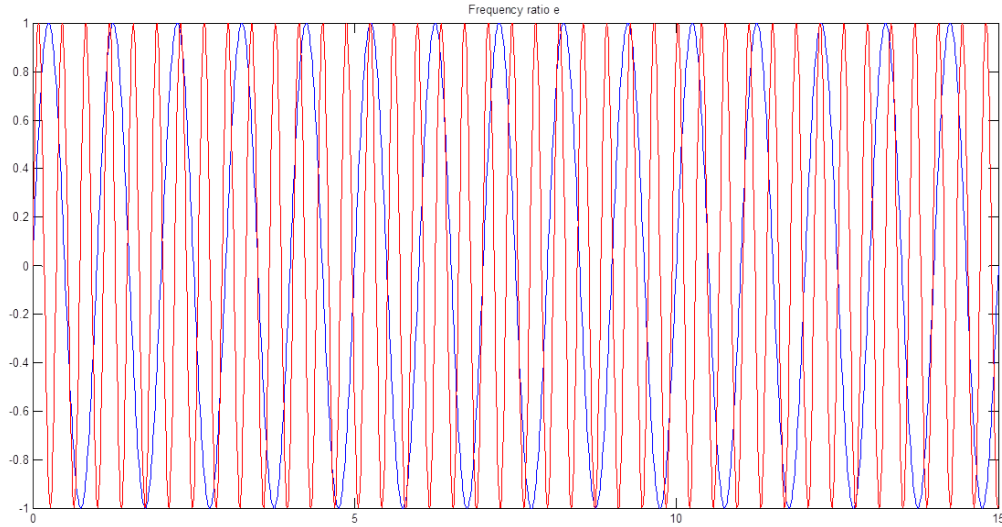


Figure 45: Frequency Ratio  $e$ ,  $f_1=1$ ,  $f_2 = e \cong 2.71$

Here there is no LCM of  $e$  and 1. There is no solution for  $M$  such that  $M$  and  $N$  are integers:

$$P = M * \frac{1}{1} = N * \frac{1}{e}$$

Equation 12: LCM equation for periodicity of signals shown in Figure 44

In the plot shown in Figure 44, there is no observable period on which both signals are periodic.

Were it necessary to investigate these excitation cases, a different way to characterize the set of excitation signals would have been required. Taking the phase of  $f_2$  when  $f_1$  has 0 phase is not a reproducible marker; Every “0-phase” point on  $f_2$  is now unique since there is no “Master period”.

Irrational frequency ratios would also have affected the end result of the FEA simulations (stresses or displacements). Using rational frequency ratios meant any driving signals all were periodic over some period  $P$ .

A rational frequency ratio implies that the nonlinear moment and the excitation frequencies would all have a master period (that is,  $\text{LCM}(f_1, f_2, f_{NL})$  does exist; remember  $f_{NL} = f_2 - f_1 \mid f_2 + f_1$  for first order approximation). Since all driving frequencies are periodic over some “master period”  $P$ , the response is also periodic over some period  $P$ . Maximum displacement/stress value observed during 1 “master period” of the response was used as an output variable in this experiment, however this would not exist for irrational frequency ratios.

If the frequency ratio were not rational, the displacement/stress response would not be periodic, and they would not be characterize-able as the peak value over a given “master period”. Instead, results would need to be characterized in the frequency domain, as the magnitude of the response

at the individual frequencies  $f_1, f_2, f_{NL}$ . Time Domain peak values could be estimated from this by summing corresponding sine waves over time and looking for peaks; however the sum would not be periodic.

This “frequency domain characterization” would still work fine for rational frequency ratios. But in the case for rational frequency ratios, the last step of summing sine waves corresponding to the frequencies  $f_1, f_2, f_{NL}$  and looking for a peak would produce the same result as looking for the peak on a “Master Period” of the time domain response plot (the sum is periodic).

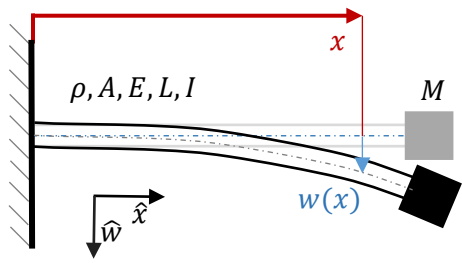
## 5.8 PWB Properties

PWB (modeled as beam) Length	350mm
PWB cross section	Rectangle, 2x2mm
PWB Material Properties	Orthotropic (mmNs units): 25175.7, 5351.53, 25175.7, 4937.66, 1937.66, 11476.7, 3700, 2900, 2900
PWB Density	$1.85 \times 10^{-9}$ tonne/mm <sup>3</sup>
Component (beam) Length	65mm
Component (beam) Cross Section	Circle, r=1.05mm
Component (beam) Tip Mass	1.5gram

Table 8: Properties of PWB FEA model

## 5.9 Beam With Tip Mass Natural Frequency Derivation

Equations of motion derivation using Hamilton's variation principal



$\rho \equiv$  Area Density (Mass/Area)

$A \equiv$  Cross sectional area (Area)

$E \equiv$  Elastic Modulus (Force/Area)

$L \equiv$  Length of Beam (Mass/Area)

$I \equiv$  Second Moment of Inertia (Mass\*Area)

$M \equiv$  Point Mass at  $x = L$  (Mass)

Equation 13: Elastic Potential Energy

$$PE = \frac{1}{2} EI \int_0^L \left( \frac{\partial^2 w}{\partial x^2} \right)^2 dx$$

Equation 14: Kinetic Energy

$$KE = \frac{1}{2} \rho A \int_0^L \dot{w}^2 dx + \frac{1}{2} M \dot{w}_L^2$$

$\dot{w}_L$  represents the velocity of the tip of the beam in the  $\hat{w}$  direction.

Beam, properties are constant along  $x$ , and can be moved outside the integrals spanning  $x$ .

Equation 15: Lagrange

$$L \equiv KE - PE = \frac{1}{2} \rho A \int_0^L \dot{w}^2 dx + \frac{1}{2} M \dot{w}_L^2 - \frac{1}{2} EI \int_0^L \left( \frac{\partial^2 w}{\partial x^2} \right)^2 dx$$

Equation 16: Variation

$$\delta L \equiv \delta KE - \delta PE = \rho A \int_0^L \dot{w} \delta \dot{w} dx + M \dot{w}_L \delta \dot{w}_L - EI \int_0^L \left( \frac{\partial^2 w}{\partial x^2} \right) \delta \left( \frac{\partial^2 w}{\partial x^2} \right) dx$$

Equation 17: Euler Lagrange Principal

$$\int_{t_0}^{t_1} \delta L dt = 0 = \int_{t_0}^{t_1} \underbrace{\rho A \int_0^L \dot{w} \delta \dot{w} dx}_{[\delta L_1]} dt + \int_{t_0}^{t_1} \underbrace{M \dot{w}_L \delta \dot{w}_L}_{[\delta L_2]} dt - \int_{t_0}^{t_1} \underbrace{EI \int_0^L \left( \frac{\partial^2 w}{\partial x^2} \right) \delta \left( \frac{\partial^2 w}{\partial x^2} \right) dx}_{[\delta L_3]} dt$$

$$\int_{t_0}^{t_1} \delta L dt = 0 = \int_{t_0}^{t_1} \delta L_1 dt + \int_{t_0}^{t_1} \delta L_2 dt - \int_{t_0}^{t_1} \delta L_3 dt$$

Equation 18: First term of Equation 5

$$\int_{t_0}^{t_1} \delta L_1 dt = \int_{t_0}^{t_1} \rho A \int_0^L \dot{w} \delta \dot{w} dx dt$$

Integrate by parts with respect to time

$$\int_{v_0}^{v_1} u dv = uv|_{v_0}^{v_1} - \int_{v_0}^{v_1} v du$$

$$u = \rho A \dot{w} \quad v = \delta w$$

$$du = \rho A \ddot{w} dt \quad dv = \delta \dot{w} dt$$

$$\int_{t_0}^{t_1} \delta L_1 dt = \rho A \int_0^L \dot{w} \delta w dx \Big|_{t_0}^{t_1} - \int_{t_0}^{t_1} \rho A \int_0^L \ddot{w} \delta w dx dt$$

Principal of virtual work

Equation 19: Simplified First term of Equation 5

$$\int_{t_0}^{t_1} \delta L_1 dt = - \int_{t_0}^{t_1} \rho A \int_0^L \ddot{w} \delta w dx dt$$

Equation 20: Second term of Equation 5

$$\int_{t_0}^{t_1} \delta L_2 dt = \int_{t_0}^{t_1} M \dot{w}_L \delta \dot{w}_L dt$$

Integrate by parts with respect to time

$$\int_{v_0}^{v_1} u dv = uv|_{v_0}^{v_1} - \int_{v_0}^{v_1} v du$$

$$u = M \dot{w}(L) \quad v = \delta w(L)$$

$$du = M \ddot{w}(L) dt \quad dv = \delta \dot{w}(L) dt$$



$$\int_{t_0}^{t_1} \delta L_2 dt = \cancel{M\dot{w}(L)\delta w(L)} \Big|_{t_0}^{t_1} - \int_{t_0}^{t_1} M\ddot{w}(L)\delta w(L) dt$$

Principal of virtual work

Equation 21: Simplified Second term of Equation 5

$$\int_{t_0}^{t_1} \delta L_2 dt = - \int_{t_0}^{t_1} M\ddot{w}(L)\delta w(L) dt$$

$$\int_{t_0}^{t_1} \delta L_3 dt = \int_{t_0}^{t_1} EI \int_0^L \left( \frac{\partial^2 w}{\partial x^2} \right) \delta \left( \frac{\partial^2 w}{\partial x^2} \right) dx dt$$

Integrate by parts with respect to x

$$\int_{v_0}^{v_1} u dv = uv \Big|_{v_0}^{v_1} - \int_{v_0}^{v_1} v du$$

$$u = -EI \frac{\partial^2 w}{\partial x^2} \quad v = \delta \left( \frac{\partial w}{\partial x} \right)$$

$$du = -EI \frac{\partial^3 w}{\partial x^3} dx \quad dv = \delta \left( \frac{\partial^2 w}{\partial x^2} \right) dx$$

Equation 22: Partly Simplified Third Term of Equation 5

$$\int_{t_0}^{t_1} \delta L_3 dt = \int_{t_0}^{t_1} -EI \frac{\partial^2 w}{\partial x^2} \delta \left( \frac{\partial w}{\partial x} \right) \Big|_0^L + EI \underbrace{\int_0^L \frac{\partial^3 w}{\partial x^3} dx \delta \left( \frac{\partial w}{\partial x} \right)}_{\int_{t_0}^{t_1} [\delta L_4] dt} dt$$

Integrate  $\delta L_4$  by parts with respect to x

$$\delta L_4 = \int_{t_0}^{t_1} EI \int_0^L \frac{\partial^3 w}{\partial x^3} dx \delta \left( \frac{\partial w}{\partial x} \right) dt$$

$$\int_{v_0}^{v_1} u dv = uv \Big|_{v_0}^{v_1} - \int_{v_0}^{v_1} v du$$

$$u = -EI \frac{\partial^3 w}{\partial x^3} \quad v = \delta w$$

$$du = -EI \frac{\partial^4 w}{\partial x^4} dx \quad dv = \delta \left( \frac{\partial w}{\partial x} \right) dx$$

$$\delta L_4 = \int_{t_0}^{t_1} EI \frac{\partial^3 w}{\partial x^3} \delta w \Big|_0^L - \int_0^L EI \frac{\partial^4 w}{\partial x^4} \delta w dx dt$$

Equation 23: Simplified Part 3 of Equation 5

$$\int_{t_0}^{t_1} \delta L_3 dt = \int_{t_0}^{t_1} -EI \frac{\partial^2 w}{\partial x^2} \delta \left( \frac{\partial w}{\partial x} \right) \Big|_0^L + EI \frac{\partial^3 w}{\partial x^3} \delta w \Big|_0^L - \int_0^L EI \frac{\partial^4 w}{\partial x^4} \delta w dx dt$$

$$\begin{aligned} \int_{t_0}^{t_1} \delta L dt &= \int_{t_0}^{t_1} \rho A \int_0^L \ddot{w} \delta w dx - M \ddot{w}(L) \delta w(L) - EI \frac{\partial^2 w}{\partial x^2} \delta \left( \frac{\partial w}{\partial x} \right) \Big|_0^L + EI \frac{\partial^3 w}{\partial x^3} \delta w \Big|_0^L \\ &\quad - \int_0^L EI \frac{\partial^4 w}{\partial x^4} \delta w dx dt \end{aligned}$$

Equation 24: Hamiltons variation Principal simplified

$$0 = - \left[ EI \frac{\partial^4 w}{\partial x^4} + \rho A \ddot{w} \right] \delta w dx - M \ddot{w}(L) \delta w(L) - EI \frac{\partial^2 w}{\partial x^2} \delta \left( \frac{\partial w}{\partial x} \right) \Big|_0^L + EI \frac{\partial^3 w}{\partial x^3} \delta w \Big|_0^L$$

Setting each part of Equation 24 to 0:

Equation 25: Equation of motion

$$EI \frac{\partial^4 w}{\partial x^4} + \rho A \ddot{w} = 0$$

Equation 26: Boundary Condition 1

$$w(0) = 0$$

Equation 27: Boundary Condition 2

$$\frac{\partial w}{\partial x}(0) = 0$$

Equation 28: Boundary Condition 3

$$\frac{\partial^2 w}{\partial x^2}(L) = 0$$

Equation 29: Boundary Condition 4

$$EI \frac{\partial^3 w}{\partial x^3}(L) = M \ddot{w}(L)$$

Assume  $w$  takes the form:

$$w \sim w(t, x) = W(x)T(t)$$

Where  $W$  is independent of time, and  $T$  is independent of  $x$ .

Separating variables in Equation 25: Equation of motion becomes:

Equation 30: Separated Equation of motion

$$-\frac{EI}{\rho A W} \frac{d^4 w}{dx^4} = \frac{1}{T} \frac{d^2 T}{dt^2}$$

Two independent variables that are equal, must equal a constant

Equation 31: Separated Equation of motion

$$-\frac{EI}{\rho A W} \frac{d^4 W}{dx^4} = \frac{1}{T} \frac{d^2 T}{dt^2} = \omega^2$$

Separating the spatial part of the equation:

$$\frac{d^4 W}{dx^4} - \frac{\rho A}{EI} \omega^2 W = 0$$

Substituting Laplace variable  $s$  for differentiation with respect to distance

Equation 32: Poles of spatial equation

$$(s^4 - \beta^4)W = 0$$

Equation 33: Beta

$$\beta = \frac{\rho A}{EI} \omega^2$$

The solution of  $W$  takes the form:

Equation 34: Form of solution of spatial component

$$W \sim C_1 \cos(\beta x) + C_2 \sin(\beta x) + C_3 \cosh(\beta x) + C_4 \sinh(\beta x)$$

From Equation 26: Boundary Condition 1 and Equation 27: Boundary Condition 2

Equation 35: Boundary Condition result

$$C_1 + C_3 = 0$$

Equation 36: Boundary Condition result

$$C_2 + C_4 = 0$$

From Equation 28: Boundary Condition 3

Equation 37: Boundary onditions plugged into solution

$$0 = C_1(-\cos(\beta L) - \cosh(\beta L)) + C_2(-\sin(\beta L) - \sinh(\beta L))$$

From Equation 29: Boundary Condition 4

Equation 38: Final boundary condition plugged in

$$0 = C_1 (EI \beta^3 \sin(\beta L) - EI \beta^3 \sin h(\beta L) + M\omega^2 \cos(\beta L) - M\omega^2 \cosh(\beta L)) \\ + C_2 (-EI \beta^3 \cos(\beta L) - EI \beta^3 \cosh(\beta L) + M\omega^2 \sin(\beta L) - M\omega^2 \sinh(\beta L))$$

Equation 37 and Equation 38 can be cast in a matrix, as a function of  $C_1$  and  $C_2$

Equation 39: Matrix form of constants

$$\begin{bmatrix} A & B \\ C & D \end{bmatrix} \begin{matrix} C_1 \\ C_2 \end{matrix} = \begin{matrix} 0 \\ 0 \end{matrix}$$

$$A = \cos(\beta L) + \cosh(\beta L)$$

$$B = \sin(\beta L) + \sinh(\beta L)$$

$$C = EI\beta^3[\sin(\beta L) - \sinh(\beta L)] + M\omega^2[\cos(\beta L) - \cosh(\beta L)]$$

$$D = -EI\beta^3[\cos(\beta L) + \cosh(\beta L)] + M\omega^2[\sin(\beta L) - \sinh(\beta L)]$$

Setting the determinant of the matrix in Equation 39 equal to zero generates a function where the only unknown is  $\omega$ .

Equation 40: Natural frequency function

$$F(\omega) \equiv \det \begin{bmatrix} A & B \\ C & D \end{bmatrix} = 0$$

Solving for the zeros of  $F(\omega)$  is done numerically.  $F(\omega)$  is a function of  $\omega$  and model constants  $\rho, A, E, L, M$  and  $I$ . Its zeros are the natural frequencies of the cantilever beam with the tip mass.

The Time responses can also be computed, if desired, by solving the temporal portion of Equation 30 and pairing it with the spatial solution of  $w(x, t)$ .

## 6 References

---

- <sup>i</sup> MIL-STD-810G, Department of Defense Test Method Standard for Environmental Engineering Considerations and Laboratory Tests. PDF. United States Department of Defense. 31 Oct 2008.
- <sup>ii</sup> IEEE 344. Institute of Electrical and Electronics Engineers (IEEE). PDF. 2013.
- <sup>iii</sup> E. Habtour, Drake, G.S, Dasgupta, A., Al-Bassyiouni, M. and Choi, C., "Improved Reliability Testing with Multiaxial Electrodynamics Vibration," in Proceedings of the Annual Reliability and Maintainability Symposium, Jan. 2010.
- <sup>iv</sup> C. Choi, M. Al Bassyiouni, Dasgupta, A. and Osterman, M., "PoF Issues in Multi-DoF Vibration Testing: ED Shakers and RS Shakers," in IEEE ASTRO9 Workshop, New Jersey, Oct 2009
- <sup>v</sup> D. Smallwood and D. Gregory, "Evaluation of a Six-DOF Electrodynamic Shaker System," in Proceedings of the 79th Shock and Vibration Symposium, Orlando, FL, 2008.
- <sup>vi</sup> E. Habtour, "Time-to-Failure Results for CALCE C11-02 Project," Unpublished raw data, 2011.
- <sup>vii</sup> M. Ernst, E. Habtour, and A. Dasgupta. "Examining Steinberg's Octave Rule Applicability for Electronic Systems Exposed to Multiaxial Vibration." IEEE Transactions on Components Packaging and Manufacturing Technology, 2016.
- <sup>viii</sup> W. Whiteman and Berman, M.B., "Fatigue Failure Results for Multiaxial Versus Uniaxial Stress Screen Vibration Testing," Journal of Shock and Vibration, vol. 9, pp. 319-328, 2002.
- <sup>ix</sup> R. French, Handy, R. and Cooper, H.L., "A Comparison of Simultaneous and Sequential Single-Axis Durability Testing," Experimental Techniques, pp. 1-6, September-October 2006.
- <sup>x</sup> D. Gregory, F. Bitsie and D. Smallwood, "Comparison of the Response of a Simple Structure to Single Axis and Multiple Axis Random Vibration Inputs," 2009.
- <sup>xi</sup> E. Habtour, Choi, C., Osterman, M. and Dasgupta, A., "Novel Approach to Improve Electronics Reliability in the Next Generation of US Army Small Unmanned Ground Vehicles Under Complex Vibration Conditions," Journal of Failure Analysis and Prevention, pp. 86-95, 2012.
- <sup>xii</sup> M. Aykan and Çelik, M., "Vibration fatigue analysis and multi-axial effect in testing of aerospace structures," Mechanical Systems and Signal Processing, vol. 23, pp. 897-907, 2009.
- <sup>xiii</sup> V. Kumar, J. Miller, and J. Rhoads. "Nonlinear parametric amplification and attenuation in a base-excited cantilever beam." Journal of Sound and Vibration. 28, June 2011. Online.
- <sup>xiv</sup> J. Rhoads, N. Miller, S. Shaw, and B. Feeny. "Mechanical Domain Parametric Amplification." Journal of Vibration and Acoustics December, 2008.
- <sup>xv</sup> A. Nayfeh and D. Mook. "Nonlinear Oscillations". Wiley Classic Library Edition, New York, 1995.
- <sup>xvi</sup> R. Sridharan, Dr. A. Dasgupta, E. Habtour, C. Choi. "Resilience of Large Electronic Components Undergoing Multi-Axial Vibratory Excitation." Proceedings of the ASME 2015 International Technical Conference and Exhibition on Packaging and Integration of Electronic and Photonic Microsystems and ASME 2015 12th International Conference on Nanochannels, Microchannels, and Minichannels, InterPACKICNMM2015. July 2016